

Making it personal

Citation for published version (APA):

van Osta, N. C. J. (2022). *Making it personal: model-based cardiac tissue characterization in arrhythmogenic cardiomyopathy*. [Doctoral Thesis, Maastricht University]. Gildeprint Drukkerijen. <https://doi.org/10.26481/dis.20220331no>

Document status and date:

Published: 01/01/2022

DOI:

[10.26481/dis.20220331no](https://doi.org/10.26481/dis.20220331no)

Document Version:

Publisher's PDF, also known as Version of record

Please check the document version of this publication:

- A submitted manuscript is the version of the article upon submission and before peer-review. There can be important differences between the submitted version and the official published version of record. People interested in the research are advised to contact the author for the final version of the publication, or visit the DOI to the publisher's website.
- The final author version and the galley proof are versions of the publication after peer review.
- The final published version features the final layout of the paper including the volume, issue and page numbers.

[Link to publication](#)

General rights

Copyright and moral rights for the publications made accessible in the public portal are retained by the authors and/or other copyright owners and it is a condition of accessing publications that users recognise and abide by the legal requirements associated with these rights.

- Users may download and print one copy of any publication from the public portal for the purpose of private study or research.
- You may not further distribute the material or use it for any profit-making activity or commercial gain
- You may freely distribute the URL identifying the publication in the public portal.

If the publication is distributed under the terms of Article 25fa of the Dutch Copyright Act, indicated by the "Taverne" license above, please follow below link for the End User Agreement:

www.umlib.nl/taverne-license

Take down policy

If you believe that this document breaches copyright please contact us at:

repository@maastrichtuniversity.nl

providing details and we will investigate your claim.

Making it Personal

**Model-based Cardiac Tissue Characterization in
Arrhythmogenic Cardiomyopathy**

Nick van Osta

Making it Personal

Model-based Cardiac Tissue Characterization in Arrhythmogenic Cardiomyopathy

Nick van Osta

ISBN: 978-94-6423-699-6

Printing: Gildeprint Enschede, gildeprint.nl

Layout and (cover) design: Harma Makken, persoonlijkproefschrift.nl

Copyright 2022 © Nick van Osta

The Netherlands. All rights reserved. No parts of this thesis may be reproduced, stored in a retrieval system or transmitted in any form or by any means without permission of the author.

Making it Personal

Model-based Cardiac Tissue Characterization in
Arrhythmogenic Cardiomyopathy

Proefschrift

ter verkrijging van de graad van doctor aan de Universiteit Maastricht,
op gezag van de Rector Magnificus, Prof. dr. Pamela Habibović
volgens het besluit van het College van Decanen,
in het openbaar te verdedigen
op donderdag 31 maart 2022 om 13.00 uur

door

Nick Cornelis Johannes van Osta

geboren op 6 juli 1994
te Roosendaal, Nederland

Promotoren

Prof. dr. ir. J. Lumens

Prof. dr. T. Delhaas

Beoordelingscommissie

Prof. dr. F.W. Prinzen (voorzitter)

Dr. ir. P.H.M. Bovendeerd (Technische Universiteit Eindhoven)

Prof. dr. ir. R.L.M. Peeters

Dr. A.S.J.M. te Riele (Universitair Medisch Centrum Utrecht)

Prof. dr. P.G.A. Volders

Financial support by the **Dutch Heart Foundation** for the publication of this thesis is gratefully acknowledged.

Financial support for the publication of this thesis as provided by **Maastricht University** is gratefully acknowledged

The prettier the flower, the further from the path

– Stephen Sondheim



Contents

Chapter 1	General Introduction	8
Chapter 2	Personalization of Biomechanical Models for Early Detection of Disease in Arrhythmogenic Cardiomyopathy	16
Chapter 3	Parameter Subset Reduction for patient-specific Modelling of Arrhythmogenic Cardiomyopathy-related Mutation Carriers in the CircAdapt Model	28
Chapter 4	Electromechanical Substrate Characterization in Arrhythmogenic Cardiomyopathy using imaging-based patient-specific Computer Simulations	52
Chapter 5	Uncertainty Quantification of Regional Cardiac Tissue Properties in Arrhythmogenic Cardiomyopathy using Adaptive Multiple Importance Sampling	74
Chapter 6	Monitoring age-related Penetrance of Structural Right Ventricular Disease in Arrhythmogenic Cardiomyopathy	100
Chapter 7	General Discussion	120
Appendices	Summary	142
	Acknowledgment (Dankwoord)	144
	Curriculum Vitae	147
	List of Publications	148

1



General Introduction



Introduction

Arrhythmogenic Cardiomyopathy (AC) is an inherited pathology of the heart for which in 60% of probands a (likely-)pathogenic mutation can be found [1,2]. It is characterized by fibrofatty replacement, primarily affects the right ventricle, and predisposes to ventricular arrhythmias and sudden cardiac death in young individuals [3,4]. Probands and family members are screened and monitored, as they are likely to develop the disease themselves [5,6]. To prevent sudden cardiac death in apparently healthy individuals, early detection of pro-arrhythmic tissue substrates is important.

Definitive diagnosis of AC is based on the presence of transmural fibro-fatty replacement of RV myocardium at biopsy, autopsy, or surgery [7,8]. As assessment of transmural myocardium is not possible in most patients, 2010 Task Force Criteria (TFC) guide the diagnosis of AC [9]. Unfortunately, the overlap of TFC with other disease expressions makes it difficult to differentiate between AC and, for example, pulmonary artery hypertension, Brugada syndrome, and Athlete's heart [10]. The use of personalized computational modelling can provide more insight in the patient's underlying myocardial disease substrates.

A patient-specific cardiac model can function as a Digital Twin, a virtual representation of reality based on comprehensive physical and functional description of the heart [11]. Digital Twins often are personalized to represent non-invasive data that is easily accessible [12,13]. The personalized computational model provides more insight in the Digital Twin's myocardial tissue properties, which reflects the patient's underlying myocardial disease substrates. As tissue properties are directly related to tissue function and composition, the properties provided by the Digital Twin might have predictive value for disease progression and might improve arrhythmogenic risk stratification.

The choice of cardiovascular computational model determines the possible representations of the Digital Twin and which properties can be estimated. Over the years, these models became more detailed. Starting with simulation of only global haemodynamics [14], nowadays cardiac models give insight in tissue mechanics [15,16] and are used for preclinical research and clinical application [17–19]. The level of detail on the tissue ranges from generalized constitutional laws with phenomenological active behaviour to multi-scale models coupling mechanics on the organ level to cellular electrophysiology [20]. As models have been improved in their ability of reproducing clinical data, the challenge now is to personalize these models to clinical data to create the Digital Twin [13,18].

The development of creating the Digital Twin is a multi-disciplinary problem engineers together with clinicians try to solve. Many challenges have been acknowledged to develop

Digital Twins and to successfully integrate them in clinical practice [13,17,18,21]. This can be summarized into six main challenges:

- *Problem Challenge*. Define the pathology, its characteristics, and its typical expressions that should be mimicked by the Digital Twin.
- *Measurement Challenge*. Clinical data containing valuable information on the pathology should be selected.
- *Model Challenge*. The computational model must have the ability to reproduce the selected clinical data must be chosen.
- *Parameter Challenge*. Computational models are often complex and extended, therefore, an identifiable parameter subset sensitive to the measurements must be defined.
- *Optimization Challenge*. This method must be suited for the complex parameter space to the selected measurements.
- *Translational Challenge*. Clinically relevant information should be extracted from the Digital Twin and translated to the clinics.

Each of these challenges should be addressed to develop a modelling framework to create a Digital Twin.

In this Thesis, we will focus on creating the Digital Twin of patients with AC. Two challenges have already been addressed in previous studies. It has been shown that right ventricular deformation abnormalities have prognostic value for disease progression [22] and arrhythmic risk stratification [23] (Measurement Challenge). Furthermore, it has been shown that the CircAdapt model [15,24] is a fast computational model which is able to reproduce these deformation abnormalities [25,26] (Model Challenge). In this thesis, we will verify whether deformation patterns produced by the CircAdapt model can be used for patient-specific modelling and we will use this information to develop a modelling framework to generate the Digital Twin of the AC heart.

Aim

The aim of this Thesis is to get more insight in the underlying myocardial disease substrate in early-stage AC patients. To do so, we will address the six challenges of creating the Digital Twin. The modelling framework will have information of regional myocardial deformation (i.e. tissue strain) as input which then is simulated with the CircAdapt model where we are *making it personal*. The subset of model parameters used for optimization will be selected based on an extensive sensitivity and identifiability analysis. Two

optimization protocols will be investigated to create a Digital Twin. These protocols will then be applied to a large patient cohort to investigate the underlying tissue substrate.

We explored the possibility to estimate patient-specific model parameters of regional RV segments in the CircAdapt model in **Chapter 2**. This chapter mostly focusses on the RV, resulting in a relatively simple optimization problem solved with a gradient-based parameter estimation algorithm. In this feasibility study, it is demonstrated that deformation patterns can be used as input of the modelling framework and that the CircAdapt model is able to reproduce these deformation patterns (Problem, Measurement, and Model Challenge).

Because of the high number of model parameters in the CircAdapt model, we did an extensive sensitivity and identifiability analysis in **Chapter 3** to objectively select the parameter subset for parameter optimization. The sensitivity analysis was performed with the Morris screening method [27]. Parameter identifiability was quantified based on the diaphony using Monte Carlo simulations [28]. Parameter subset reduction was performed based on identifiability and validated by optimizing parameters with particle swarm optimization [29] (Parameter and Optimization Challenge).

After defining the optimal parameter subset, we used this subset in **Chapter 4** to patient-specific personalize the CircAdapt model to a large cohort of 68 individuals with a desmosomal mutation related to AC [26]. We compared the estimated tissue properties with severity of deformation abnormalities and with clinical stage based on 2010 TFC (Translational Challenge).

Measurement uncertainty inevitably affects model parameter estimations. When investigating tissue properties in a longitudinal study design, this uncertainty might influence the estimation and thereby should be taken into account. Therefore, in **Chapter 5**, we applied a Bayesian inference approach to estimate posterior distributions of model parameters rather than only providing point estimates. To do so, we applied adaptive multiple importance sampling [30,31] to randomly draw samples to form the posterior distribution (Optimization and Translational Challenge).

In **Chapter 6**, we applied the Bayesian inference algorithm explored in Chapter 5 on a large cohort of 82 probands and family members without structural abnormalities present at baseline. In total, 313 datasets at baseline and follow-up were included to investigate the age penetrance of AC. Both clinical measures as well as computationally estimated tissue properties were investigated (Translational Challenge).

The concluding **Chapter 7** discusses the different approaches described in this Thesis in a more global context. Strengths and weaknesses of our framework are discussed and opportunities offered by our modelling framework are hypothesized.

References

1. Sen-Chowdhry S, Syrris P, McKenna WJ. 2007 Role of Genetic Analysis in the Management of Patients With Arrhythmogenic Right Ventricular Dysplasia/Cardiomyopathy. *J. Am. Coll. Cardiol.* **50**, 1813–1821. (doi:10.1016/j.jacc.2007.08.008)
2. Cox MGPJ *et al.* 2011 Arrhythmogenic right ventricular dysplasia/cardiomyopathy: Pathogenic desmosome mutations in index-patients predict outcome of family screening: Dutch arrhythmogenic right ventricular dysplasia/cardiomyopathy genotype-phenotype follow-up study. *Circulation* **123**, 2690–2700. (doi:10.1161/CIRCULATIONAHA.110.988287)
3. Thiene G, Nava A, Corrado D, Rossi L, Pennelli N. 1988 Right Ventricular Cardiomyopathy and Sudden Death in Young People. *N. Engl. J. Med.* **318**, 129–133. (doi:10.1056/NEJM198801213180301)
4. Basso C, Corrado D, Marcus FI, Nava A, Thiene G. 2009 Arrhythmogenic right ventricular cardiomyopathy. *Lancet* **373**, 1289–1300. (doi:10.1016/S0140-6736(09)60256-7)
5. Priori SG *et al.* 2013 Executive Summary: HRS/EHRA/APHRs Expert Consensus Statement on the Diagnosis and Management of Patients with Inherited Primary Arrhythmia Syndromes. *Heart Rhythm* **10**, e85–e108. (doi:10.1016/j.hrthm.2013.07.021)
6. Charron P *et al.* 2010 Genetic counselling and testing in cardiomyopathies: A position statement of the European Society of Cardiology Working Group on Myocardial and Pericardial Diseases. *Eur. Heart J.* **31**, 2715–2728. (doi:10.1093/eurheartj/ehq271)
7. Basso C, Thiene G. 2007 Arrhythmogenic right ventricular cardiomyopathy/dysplasia. In *Orphanet Journal of Rare Diseases* (eds F Marcus, A Nava, G Thiene), pp. 29–44. (doi:10.1186/1750-1172-2-45)
8. Basso C, Burke M, Fornes P, Gallagher PJ, De Gouveia RH, Sheppard M, Thiene G, Van Der Wal A. 2008 Guidelines for autopsy investigation of sudden cardiac death. *Virchows Arch.* **452**, 11–18. (doi:10.1007/s00428-007-0505-5)
9. Marcus FI *et al.* 2010 Diagnosis of Arrhythmogenic Right Ventricular Cardiomyopathy/Dysplasia: Proposed Modification of the Task Force Criteria. *Eur. Heart J.* **31**, 806–814. (doi:10.1093/eurheartj/ehq025)
10. Corrado D *et al.* 2020 Arrhythmogenic right ventricular cardiomyopathy: evaluation of the current diagnostic criteria and differential diagnosis. *Eur. Heart J.* **41**, 1414–1429. (doi:10.1093/eurheartj/ehz669)
11. Boschert S, Rosen R. 2016 Digital Twin—The Simulation Aspect. In *Mechatronic Futures: Challenges and Solutions for Mechatronic Systems and Their Designers* (eds P Hehenberger, D Bradley), pp. 1–259.
12. Niederer SA, Lumens J, Trayanova NA. 2019 Computational models in cardiology. *Nat. Rev. Cardiol.* **16**, 100–111. (doi:10.1038/s41569-018-0104-y)
13. Corrat-Acero J *et al.* 2020 The ‘Digital Twin’ to enable the vision of precision cardiology. *Eur. Heart J.* **41**, 4556–4564B. (doi:10.1093/eurheartj/ehaa159)
14. Suga H, Sagawa K, Shoukas AA. 1973 Load independence of the instantaneous pressure-volume ratio of the canine left ventricle and effects of epinephrine and heart rate on the ratio. *Circ. Res.* **32**, 314–322. (doi:10.1161/01.RES.32.3.314)
15. Arts T, Delhaas T, Bovendeerd P, Verbeek X, Prinzen F. 2005 Adaptation to Mechanical Load Determines Shape and Properties of Heart and Circulation: the CircAdapt Model. *Am. J. Physiol. Heart Circ. Physiol.* **288**, 1943–1954. (doi:10.1152/ajpheart.00444.2004.)
16. Fritz T, Wieners C, Seemann G, Steen H, Dössel O. 2014 Simulation of the contraction of the ventricles in a human heart model including atria and pericardium: Finite element analysis of a frictionless contact problem. *Biomech. Model. Mechanobiol.* **13**, 627–641. (doi:10.1007/s10237-013-0523-y)
17. Gray RA, Pathmanathan P. 2018 Patient-specific cardiovascular computational modeling: Diversity of personalization and challenges. *J. Cardiovasc. Transl. Res.* **11**, 80–88. (doi:10.1007/s12265-018-9792-2)
18. Niederer SA, Lumens J, Trayanova NA. 2019 Computational models in cardiology. *Nat. Rev. Cardiol.* **16**, 100–111. (doi:10.1038/s41569-018-0104-y)
19. Kerckhoffs RCP, Neal ML, Gu Q, Bassingthwaight JB, Omens JH, McCulloch AD. 2007 Coupling of a 3D finite element model of cardiac ventricular mechanics to lumped systems models of the systemic and pulmonary circulation. *Ann. Biomed. Eng.* **35**, 1–18. (doi:10.1007/s10439-006-9212-7)
20. Trayanova NA. 2011 Whole-heart modeling: Applications to cardiac electrophysiology and electromechanics. *Circ. Res.* **108**, 113–128. (doi:10.1161/CIRCRESAHA.110.223610)
21. Neal ML, Kerckhoffs R. 2009 Current progress in patient-specific modeling. *Brief. Bioinform.* **11**, 111–126. (doi:10.1093/bib/bbp049)

22. Mast TP *et al.* 2019 The Prognostic Value of Right Ventricular Deformation Imaging in Early Arrhythmogenic Right Ventricular Cardiomyopathy. *JACC Cardiovasc. Imaging*, 14 March. **12**, 446–455. (doi:10.1016/j.jcmg.2018.01.012)
23. Sarvari SI, Haugaa KH, Anfinsen OG, Leren TP, Smiseth OA, Kongsgaard E, Amlie JP, Edvardsen T. 2011 Right ventricular mechanical dispersion is related to malignant arrhythmias: A study of patients with arrhythmogenic right ventricular cardiomyopathy and subclinical right ventricular dysfunction. *Eur. Heart J.* **32**, 1089–1096. (doi:10.1093/eurheartj/ehr069)
24. Lumens J, Delhaas T, Kirn B, Arts T. 2009 Three-wall segment (TriSeg) model describing mechanics and hemodynamics of ventricular interaction. *Ann. Biomed. Eng.* **37**, 2234–2255. (doi:10.1007/s10439-009-9774-2)
25. Walmsley J, Arts T, Derval N, Bordachar P, Cochet H, Ploux S, Prinzen FW, Delhaas T, Lumens J. 2015 Fast Simulation of Mechanical Heterogeneity in the Electrically Asynchronous Heart Using the MultiPatch Module. *PLoS Comput. Biol.* **11**, 1–23. (doi:10.1371/journal.pcbi.1004284)
26. Mast TP *et al.* 2016 Right Ventricular Imaging and Computer Simulation for Electromechanical Substrate Characterization in Arrhythmogenic Right Ventricular Cardiomyopathy. *J. Am. Coll. Cardiol.* **68**, 2185–2197. (doi:10.1016/j.jacc.2016.08.061)
27. Morris MD. 1991 Factorial Sampling Plans for Preliminary Computational Experiments. *Technometrics*. **33**.
28. Hornfeck W, Kuhn P. 2015 Diaphony, a measure of uniform distribution, and the Patterson function. *Acta Crystallogr. Sect. A Found. Adv.* **71**, 382–391. (doi:10.1107/S2053273315007123)
29. Kennedy J, Eberhart R. In press. Particle swarm optimization. In *Proceedings of ICNN'95 - International Conference on Neural Networks*, pp. 1942–1948. IEEE. (doi:10.1109/ICNN.1995.488968)
30. Cornuet JM, Marin JM, Mira A, Robert CP. 2012 Adaptive Multiple Importance Sampling. *Scand. J. Stat.* **39**, 798–812. (doi:10.1111/j.1467-9469.2011.00756.x)
31. Bugallo MF, Elvira V, Martino L, Luengo D, Miguez J, Djuric PM. 2017 Adaptive Importance Sampling: The past, the present, and the future. *IEEE Signal Process. Mag.* **34**, 60–79. (doi:10.1109/MSP.2017.2699226)

2



9509450565
7857894385
3489989345
05679930947437
43857789234789
34577849300484
289438577892347
8934577849300

Personalization of Biomechanical Models for Early Detection of Disease in Arrhythmogenic Cardiomyopathy

Based on: **Nick van Osta**, Feddo P. Kirkels, Aurore Lyon, Tammo Delhaas, Maarten J. Cramer, Arco J. Teske, Joost Lumens “Personalization of Biomechanical Models for Early Detection of Disease in Arrhythmogenic Cardiomyopathy” *2018 Computing in Cardiology Conference* (2018)

Abstract

Arrhythmogenic cardiomyopathy (AC) is an inherited cardiac disease clinically characterized by life-threatening ventricular arrhythmias and progressive cardiac dysfunction. Current electrocardiographic and structural imaging methods fail to detect early-stage AC-related myocardial disease in mutation carriers. We propose a cardiac imaging-based personalized modelling approach that enables the identification and characterization of regional electro-mechanical tissue abnormalities in the vulnerable right ventricular (RV) free wall of AC mutation carriers.

RV tissue deformation data from 2 controls and 8 mutation carriers, covering various stages of AC disease, were used to personalize the CircAdapt model of the human heart and circulation. This resulted in estimates of contractility and stiffness in the apical, midventricular, and basal segments of the RV.

Apex-to-base heterogeneity in tissue properties, with increased stiffness and decreased contractility in the RV basal region, was found in most patients and was largest in late-stage AC disease. Future studies should evaluate whether early-stage tissue heterogeneity is predictive for arrhythmic events or AC disease progression.

Introduction

Arrhythmogenic Cardiomyopathy (AC) is considered as an inherited cardiomyopathy predisposing to ventricular arrhythmias, sudden cardiac death (SCD), and more rarely (bi)ventricular dysfunction and heart failure [1,2]. A genetic mutation is found in up to 60% of probands, mostly affecting desmosomal genes [3]. To prevent sudden cardiac death in these apparently healthy AC mutation carriers, early detection of pro-arrhythmic tissue substrates is important. Current conventional electrocardiographic and structural imaging methods lack sensitivity to detect early-stage AC-related myocardial disease in genotype-positive AC family members.

In a recent study [4], Mast et al. showed that regional right ventricular (RV) deformation abnormalities exist in most individuals with a pathogenic plakophilin-2 (PKP2) or desmoglein-2 mutation, even in those classified as subclinical (concealed) or electrical stage AC patients according to the 2010 International Task Force Criteria [5]. In the same study, generic patient simulations obtained with a biophysical model of the human heart and circulation suggested that those regional RV deformation abnormalities originate from regional contractile dysfunction either or not in combination with myocardial stiffening.

In a follow-up study [6], Mast et al. showed that early-stage AC mutation carriers with an abnormal pattern of basal RV deformation are more likely to progress into a more advanced AC disease stage than those with normal basal RV deformation. RV mechanical dispersion has also been reported in early stage AC patients [7] and has been found to be associated with arrhythmic outcome [8].

These observed regional differences in RV myocardial deformation suggest the existence of a detectable heterogeneity in local tissue properties in early-stage AC. A biophysical model of the human heart and circulation, such as the CircAdapt Model [9,10], describes the mechanistic link between myocardial tissue properties and regional myocardial deformation, based on well-established physics and physiology principles. We therefore hypothesize that cardiac imaging-based personalization of the CircAdapt model can reveal the severity of AC-related RV tissue disease. In this study, we aimed to explore the potential of personalizing the CircAdapt model to patient-specific characterize regional differences in RV myocardial tissue properties.

Methods

Patient Cohort

A total of 2 control subjects and 8 mutation carriers (4 male, age 33.8 ± 14.9 years) were selected from the previously introduced AC cohort [4]. Selection was based on covering the spectrum of AC disease severity. Longitudinal RV strain was measured in three segments

(apex, mid, and base) using a standard echocardiographic deformation imaging protocol that has been described in more detail elsewhere [11]. LV and RV end diastolic volumes ($154 \pm 26 \text{ mL}$ and $184 \pm 38 \text{ mL}$, respectively) and stroke volume ($85 \pm 21 \text{ mL}$) were obtained by cardiac magnetic resonance imaging (CMR) performed on a 1.5-T scanner (Achieva, Philips Healthcare, Best, the Netherlands), according to standard AC protocol [12].

Based on their RV basal strain pattern, the subjects were classified in three subgroups, representing increasing severity of AC disease [5]. One mutation carrier and two controls had normal RV deformation (Type-I), four mutation carriers showed mildly abnormal deformation (Type-II), and three showed severely abnormal deformation (Type-III).

Personalized Model Simulation

The CircAdapt model was used to simulate cardiac pump function and cardiovascular system dynamics [9]. CircAdapt is a lumped-parameter model which couples regional myocardial tissue mechanics in the cardiac walls to pump mechanics and haemodynamics of a geometrically simplified four-chamber heart model and closed-loop circulation. Its MultiPatch module [13] was used to divide the RV free wall in three tissue segments, representing the basal, midventricular, and apical regions.

Passive and Active Tissue Behaviour

The CircAdapt model has been extensively explained elsewhere [13]. In this study, we aim to patient-specific estimate RV tissue parameters describing cardiac myofibre mechanics. In brief, cardiac myofibre mechanics were modelled using a Hill-type contraction model including active (myofibre contraction) and passive (soft tissue deformation of the myocardium) stress components [13]. In this model, passive fibre stress is described by a nonlinear relation depending on sarcomere length (l_s),

$$\sigma_{f,pas} = SfPas \left(\left(\frac{l_s}{l_{s0}} \right)^{k_1} - 1 \right) \quad 2.1$$

where l_{s0} represents stress-free fibre length, $SfPas$ a scaling factor, referred to as stiffness in the remainder of this study, and k_1 the exponent determining the degree of non-linearity. We assumed k_1 and l_{s0} to be constant, i.e. 10 and $1.8 \mu\text{m}$, respectively.

The active fibre stress is a function f of time (t), sarcomere length (l_s), and contractile element length (l_{si}) multiplied by a scaling factor $SfAct$.

$$\sigma_{f,act} = SfAct \cdot f(t, l_s, l_{si}) \quad 2.2$$

In the rest of this study, contractility refers to this scaling factor.

Parameter Estimation Protocol

The CircAdapt model was personalized by fitting simulated RV strain patterns to the patient's RV strain patterns, since this region is typically first-affected. To that end, parameters related to regional RV stiffness and contractility, relative systole duration, and LV and RV cavity and wall volume were adjusted for each patient. RV stiffness and contractility were estimated by minimizing the error between a set of simulated and measured RV strain indices, together capturing the pattern of regional RV deformation (Table 2.1 and Figure 2.1): time-to-peak-pre-stretch (TTPP), peak pre-stretch, time-to-50%-shortening (TT50), time-to-peak-strain (TTPS), peak strain (PS), and end systolic strain (ESS). LV end diastolic volume was fitted by changing the LV cavity volume while maintaining wall thickness constant. RV wall and cavity volume were changed to fit RV global longitudinal strain. Relative systolic duration was estimated from time to pulmonary valve closure.

Table 2.1. Indices used for estimation of contractility and stiffness.

Index	Definition	Constant
TTPP	$(t_{PP,model} - t_{PP,meas})$	/ 10 ms
PP	$(\max(\epsilon_{model}) - \max(\epsilon_{meas}))$	/ 1 %
TT50	$(t_{50\%,model} - t_{50\%,meas})$	/ 10 ms
TTPS	$(t_{peak,model} - t_{peak,meas})$	/ 10 ms
ESS	$(\epsilon_{PVC,model} - \epsilon_{PVC,meas})$	/ 1 %
PS	$(\min(\epsilon_{model}) - \min(\epsilon_{meas}))$	/ 1 %

TTPP: Time to peak pre-stretch; PP: Peak Pre-stretch; TT50: Time to 50% shortening; TTPS: Time to peak strain; ESS: End Systolic Strain; PVC: Pulmonary Valve Closure; PS: Peak Strain

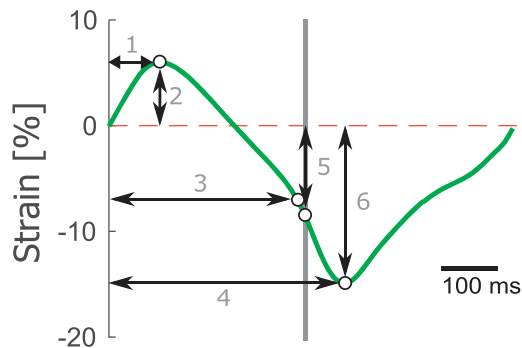


Figure 2.1. Indices used for fitting. Arrows represent the indices TTPP (1), Peak Pre-Stretch (2) TT50 (3), TTPS (4) End Systolic Strain (5), and Peak Strain (6), as described in Table 2.1.

To minimize the squared sum of error in the indices, the trust-region algorithm was used. The algorithm stopped when the estimated step size of the parameters became smaller than 0.1% of the original value. The regional tissue parameters described earlier were estimated in iterative steps until convergence to improve convergence of the parameter estimation algorithm. To quantify the goodness of the fit, the unitless mean squared strain error (X^2) of the three segmental RV strain patterns was calculated as the squared sum of difference in strain between simulation and measurement, normalized to the cycle time for better comparison between subjects.

$$X^2 = \frac{\left(\oint \epsilon_{model}(t) - \epsilon_{meas}(t) \right)^2}{tCycle} \quad 2.3$$

with ϵ_{model} and ϵ_{meas} being simulated and measured strain at time t , respectively. A perfect fit would result in an X^2 of zero. The error is squared to increase the weight of larger differences in strain error. To quantify the degree of tissue heterogeneity for each type of AC disease, the standard deviation of the three segmental parameter values was calculated per subject and averaged for each subgroup.

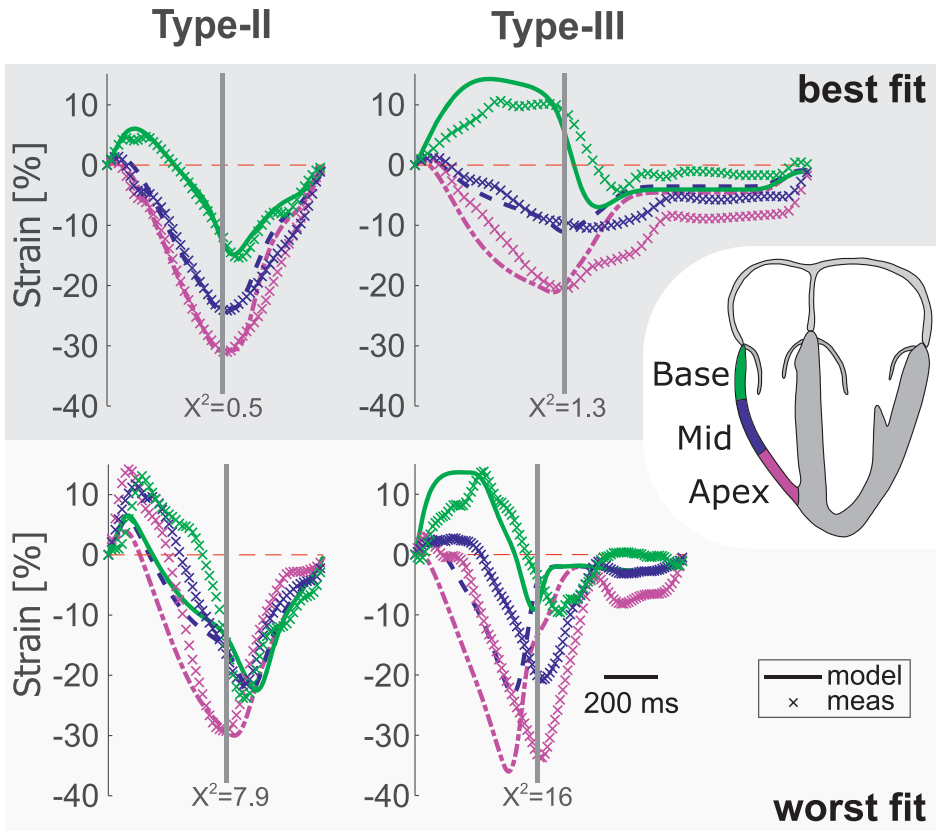
Numerical Implementation

Simulations were performed in MATLAB 2017a (MathWorks, Natick, MA, USA). Simulations were run on a PC with 8 GB RAM and an Intel i7-7600U (2.8 GHz, 2 cores).

Results

The simulated strains obtained from the personalized models are in good agreement with the measurements. The median X^2 of all estimations is 2.6, with a minimum and maximum of 0.5 and 16, respectively. The strain of two good and two bad estimations with X^2 are shown in Figure 2.2.

Figure 2.3 shows the mean estimated contractility and stiffness relative to the apical estimations for apical, mid, and basal segments. Both contractility and stiffness are more homogeneously distributed in Type-I, with a heterogeneity of 18% in contractility and a heterogeneity of 23% in stiffness. In Type-II and Type-III, the parameters are more heterogeneously distributed with a heterogeneity of 23% in contractility and 83% in stiffness in Type-II, and a heterogeneity of 39% in contractility and 161% in stiffness in Type-III. On average, basal contractility decreases and stiffness increases for Type-II and Type-III, leading to an increase of RV tissue heterogeneity with progression of AC disease.



2

Figure 2.2. Two best (first and third from left) and two worst fits (second and fourth from left) in terms of X^2 of Type-II and Type-III patients. The vertical line represents the closure of pulmonary valve in both measurements and model. Onset QRS is taken to be the zero-strain reference point.

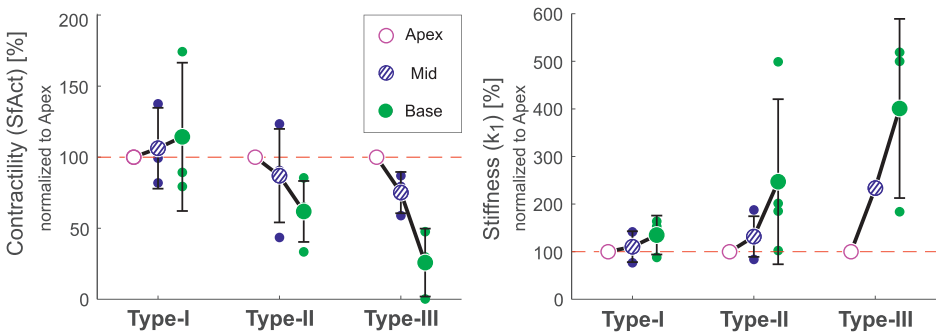


Figure 2.3. Fitted contractility and stiffness normalized to the apical values. The mean estimated values of contractility $SfAct$ and stiffness $SfPas$ per type (large dots) are shown with bars representing the standard deviation of the individual subjects (small dots).

Discussion

The main outcome of this study is the characterization of the tissue mechanisms underlying deformation abnormalities in AC subjects using a patient-specific modelling-based approach. The results suggest that AC disease progression, defined as the level of RV basal deformation abnormality, is associated with growing RV apex-to-base heterogeneity in contractile dysfunction and myocardial stiffening. The patient-specific simulations of the subjects with a Type-II deformation pattern, which was previously found in about half of the subclinical mutation carriers, revealed decreased basal contractility and increased basal stiffness compared to the apex. This finding is in line with the hypothesis by Mast et al. [4].

These predicted changes in contractility and stiffness may be explained by fibro-fatty replacement, which is conventionally detected by late gadolinium enhancement (LGE). However, LGE was detected in only one Type-II and one Type-III patient. This suggests that our method may reveal tissue abnormalities other than detected by LGE. This could also be in line with a limited sensitivity of LGE in the RV due to, for example, the typical thin RV lateral wall, and the presence of more diffuse fibrosis in AC patients [14].

Tissue behaviour of the RV lateral wall depends not only on its intrinsic tissue properties, but also on mechanical interaction with the LV lateral and septal wall. This study focusses on the RV, because this is typically the first affected area in PKP2 mutation carriers [15]. In later disease stages, LV involvement can be observed at the macroscopic level [5], but also in early stages, as AC-related genes may be expressed differently in the LV [16]. Additionally to these pathological findings, cardiac differences between subjects due to patient's length, weight, lifestyle, and other factors will lead to subject-to-subject differences in both LV and RV tissue characteristics. Therefore, including LV tissue in the parameter estimation protocol might improve goodness of fit in the RV and reduce model discrepancy in the LV. Additionally to EDV, LV strain should be included in the objective function to more reliably estimate LV tissue properties. By including LV tissue properties in the estimation, ventricular interaction via the septum in the TriSeg module should improve the estimation of RV tissue properties.

Currently, one fitting protocol with a fixed starting point is used. In the future, uniqueness of the solutions should be investigated. Future work can also develop the current estimation protocol by including other strain indexes to remove local minima, or by including other parameters to better capture the disease's mechanics. Gradient based optimization algorithms have a chance to find local minima in complex models, so other derivative-free optimization techniques should be considered to improve accuracy of the fitting protocol [17]. Finally, this study focuses on a relatively small cohort of PKP2

mutation carriers only. Future work should include a larger clinical sample size of a genetically more heterogeneous cohort of AC mutation carriers to evaluate the ability of the simulation based electromechanical substrates to stratify arrhythmic risk.

Conclusion

We presented a patient-specific modelling approach and showed its ability to reproduce regional RV deformation abnormalities in AC mutation carriers by introducing apex to base heterogeneity in regional tissue properties. Estimation of model parameters is limited to regional RV parameters. To improve the reliability of the estimations, future studies should include both RV and LV deformation in the objective function and both RV and LV parameters in the set of parameters included in the optimization. A sensitivity and identifiability analysis should support the choice of model parameters included in the estimation. Other optimization techniques should be investigated in order to improve convergence.

References

1. Basso C, Corrado D, Marcus FI, Nava A, Thiene G. 2009 Arrhythmogenic right ventricular cardiomyopathy. *Lancet* 373, 1289–1300. (doi:10.1016/S0140-6736(09)60256-7)
2. Thiene G, Nava A, Corrado D, Rossi L, Pennelli N. 1988 Right Ventricular Cardiomyopathy and Sudden Death in Young People. *N. Engl. J. Med.* 318, 129–133. (doi:10.1056/NEJM198801213180301)
3. Groeneweg JA et al. 2015 Clinical Presentation, Long-Term Follow-Up, and Outcomes of 1001 Arrhythmogenic Right Ventricular Dysplasia/Cardiomyopathy Patients and Family Members. *Circ. Cardiovasc. Genet.* 8, 437–446. (doi:10.1161/CIRCGENETICS.114.001003)
4. Mast TP et al. 2016 Right Ventricular Imaging and Computer Simulation for Electromechanical Substrate Characterization in Arrhythmogenic Right Ventricular Cardiomyopathy. *J. Am. Coll. Cardiol.* 68, 2185–2197. (doi:10.1016/j.jacc.2016.08.061)
5. Marcus FI et al. 2010 Diagnosis of Arrhythmogenic Right Ventricular Cardiomyopathy/Dysplasia: Proposed Modification of the Task Force Criteria. *Eur. Heart J.* 31, 806–814. (doi:10.1093/eurheartj/ehq025)
6. Mast TP et al. 2019 The Prognostic Value of Right Ventricular Deformation Imaging in Early Arrhythmogenic Right Ventricular Cardiomyopathy. *JACC Cardiovasc. Imaging*, 14 March. 12, 446–455. (doi:10.1016/j.jcmg.2018.01.012)
7. Saberniak J, Leren IS, Haland TF, Beitnes JO, Hopp E, Borgquist R, Edvardsen T, Haugaa KH. 2017 Comparison of patients with early-phase arrhythmogenic right ventricular cardiomyopathy and right ventricular outflow tract ventricular tachycardia. *Eur. Heart J. – Cardiovasc. Imaging* 18, 62–69. (doi:10.1093/ehjci/jew014)
8. Lie ØH, Rootwelt-Norberg C, Dejgaard LA, Leren IS, Stokke MK, Edvardsen T, Haugaa KH. 2018 Prediction of Life-Threatening Ventricular Arrhythmia in Patients with Arrhythmogenic Cardiomyopathy. *JACC Cardiovasc. Imaging* 11, 2660. (doi:10.1016/j.jcmg.2018.05.017)
9. Arts T, Delhaas T, Bovendeerd P, Verbeek X, Prinzen F. 2005 Adaptation to Mechanical Load Determines Shape and Properties of Heart and Circulation: the CircAdapt Model. *Am. J. Physiol. Heart Circ. Physiol.* 288, 1943–1954. (doi:10.1152/ajpheart.00444.2004.)
10. Lumens J, Delhaas T, Kirn B, Arts T. 2009 Three-wall segment (TriSeg) model describing mechanics and hemodynamics of ventricular interaction. *Ann. Biomed. Eng.* 37, 2234–2255. (doi:10.1007/s10439-009-9774-2)
11. Teske AJ, De Boeck BW, Melman PG, Sieswerda GT, Doevendans PA, Cramer MJ. 2007 Echocardiographic Quantification of Myocardial Function using Tissue Deformation Imaging, a Guide to Image Acquisition and Analysis using Tissue Doppler and Speckle Tracking. *Cardiovasc. Ultrasound.* 5, 27. (doi:10.1186/1476-7120-5-27)
12. Dalal D et al. 2009 Morphologic Variants of Familial Arrhythmogenic Right Ventricular Dysplasia/Cardiomyopathy: A Genetics–Magnetic Resonance Imaging Correlation Study. *J. Am. Coll. Cardiol.* 53, 1289–1299. (doi:10.1016/J.JACC.2008.12.045)
13. Walmsley J, Arts T, Derval N, Bordachar P, Cochet H, Ploux S, Prinzen FW, Delhaas T, Lumens J. 2015 Fast Simulation of Mechanical Heterogeneity in the Electrically Asynchronous Heart Using the MultiPatch Module. *PLoS Comput. Biol.* 11, 1–23. (doi:10.1371/journal.pcbi.1004284)
14. van Oorschoot JWM, Güçlü F, de Jong S, Chamuleau SAJ, Luijten PR, Leiner T, Zwanenburg JJM. 2017 Endogenous Assessment of Diffuse Myocardial Fibrosis in Patients with T1ρ-mapping. *J. Magn. Reson. Imaging* 45, 132–138. (doi:10.1002/jmri.25340)
15. Teske AJ, Cox MGPJ, Te Riele ASJM, De Boeck BW, Doevendans PA, Hauer RNW, Cramer MJM. 2012 Early Detection of Regional Functional Abnormalities in Asymptomatic ARVD/C Gene Carriers. *J. Am. Soc. Echocardiogr.* 25, 997–1006. (doi:10.1016/j.echo.2012.05.008)
16. Asimaki A et al. 2009 A New Diagnostic Test for Arrhythmogenic Right Ventricular Cardiomyopathy. *N. Engl. J. Med.* 360, 1075–1084. (doi:10.1056/NEJMoa0808138)
17. Audet C, Kokkolaras M. 2016 Blackbox and derivative-free optimization: theory, algorithms and applications. *Optim. Eng.* 17, 1–2. (doi:10.1007/s11081-016-9307-4)

3



Parameter Subset Reduction for patient-specific Modelling of Arrhythmogenic Cardiomyopathy-related Mutation Carriers in the CircAdapt Model

Based on: **Nick van Osta**, Aurore Lyon, Feddo P. Kirkels, Tijmen Koopsen, Tim van Loon, Maarten J. Cramer, Arco J. Teske, Tammo Delhaas, Wouter Huberts, Joost Lumens “Parameter subset reduction for patient-specific modelling of arrhythmogenic cardiomyopathy-related mutation carriers in the CircAdapt model” *Philosophical Transactions of the Royal Society A* (2020)

Abstract

Arrhythmogenic Cardiomyopathy (AC) is an inherited cardiac disease, clinically characterized by life-threatening ventricular arrhythmias and progressive cardiac dysfunction. Patient-specific computational models could help understand the disease progression and may help in clinical decision making.

We propose an inverse modelling approach using the CircAdapt model to estimate patient-specific regional abnormalities in tissue properties in AC subjects. However, the number of parameters ($n=110$) and their complex interactions make personalized parameter estimation challenging. The goal of this study is to develop a framework for parameter reduction and estimation combining Morris Screening, quasi-Monte Carlo simulations, and Particle Swarm Optimization (PSO). This framework identifies the best subset of tissue properties based on clinical measurements allowing patient-specific identification of right ventricular tissue abnormalities.

We applied this framework on 15 AC genotype positive subjects with varying degrees of myocardial disease. Cohort studies have shown that atypical regional right ventricular (RV) deformation patterns reveal early-stage AC disease. The CircAdapt model of cardiovascular mechanics and haemodynamics already demonstrated its ability to capture typical deformation patterns of AC subjects. We, therefore, use clinically measured cardiac deformation patterns to estimate model parameters describing myocardial disease substrates underlying these AC-related RV deformation abnormalities.

Morris screening reduced the subset to 48 parameters. Quasi-Monte Carlo and PSO further reduced the subset to a final selection of 23 parameters, including regional tissue contractility, passive stiffness, activation delay, and wall reference area.

Introduction

Arrhythmogenic Cardiomyopathy (AC) is an inherited cardiomyopathy, clinically characterized by the occurrence of ventricular arrhythmias, sudden cardiac death (SCD), and predominantly right ventricular (RV) dysfunction [1,2]. A pathogenic genetic mutation, mostly affecting desmosomal genes, is found in up to 60% of probands. This mutation may result in fibro-fatty replacement of the myocardium, which can be a substrate for life-threatening arrhythmias and may already occur in an early stage without overt signs of disease using conventional screening tools [3]. To prevent SCD in these apparently healthy AC mutation carriers, early detection of pro-arrhythmic tissue substrates is important.

The diagnosis of AC is based on a set of criteria described in the revised 2010 Task Force Criteria (TFC), with the electrocardiogram (ECG) and cardiac imaging as central elements [4]. By using these conventional screening tools, mutation carriers can be classified into three categories: 1) a concealed stage with no abnormalities, 2) an electrical stage with electrical abnormalities, but no structural abnormalities, and 3) a structural stage with both electrical and structural abnormalities. Conventional electrocardiographic and structural imaging methods as described in the 2010 TFC are specific but may lack sensitivity to detect early-stage AC-related myocardial disease in genotype-positive AC patients and family members [5].

Mast et al. [5] found local RV deformation abnormalities in the absence of electrocardiographic and structural 2010 TFC. These abnormal deformation patterns were derived from speckle tracking echocardiography in individuals with a pathogenic Plakophilin-2 (PKP2) or Desmoglein-2 (DSG2) mutation [5]. In a follow-up study by the same group, these deformation abnormalities were related to disease progression from a concealed stage to a stage where subjects had developed electrical or structural abnormalities [6], which suggests that identifying the underlying substrate responsible for these strain abnormalities would help us understand disease progression and ultimately help in arrhythmic risk stratification.

In the initial study by Mast et al. [5], generic *in silico* patient simulations were performed using the CircAdapt model. This model is a biophysical model of the human heart and circulation describing the mechanistic link between myocardial tissue properties and regional myocardial strain based on well-established physical and physiological principles [7]. These simulations suggest that regional RV strain abnormalities in AC patients originate from regional contractile dysfunction either or not in combination with myocardial stiffening.

Generic simulations as described above give insight into the disease origin for the generic population, but do not contain patient-specific data. Therefore, we hypothesize that cardiac deformation imaging-based personalisation of the CircAdapt model not only

may reveal the severity of AC-related RV tissue disease, but also may help to monitor or even to predict disease progression, and therefore may support clinical decision making.

To use the CircAdapt model for clinical decision support in AC subjects, it is essential to assess which model parameters can be uniquely identified given this model and available data. The CircAdapt model as configured for this study contains 110 parameters. Due to mechanical interactions within and between the walls of the heart on one hand and between heart and circulation, on the other hand, the model acts highly non-linear, non-monotone, and non-additive. This behaviour, combined with the limited amount of available clinical data, challenges the identifiability of the parameters. Therefore, patient-specific modelling of cardiac deformation characteristics is challenging.

Reducing the dimensionality of the model is necessary for patient-specific modelling. This can be done with a screening method such as Morris screening [8]. It is based on a one-at-a-time method, where the effect of individual parameter changes on the model output is evaluated. The method is designed to account not only for their individual effect but also interactions. It has been demonstrated to be a proxy for the variance-based total sensitivity index of a parameter [9]. Therefore, it is a suitable method to reduce dimensionality of the model.

Due to the complexity of the model, Morris screening does not result in a sufficiently reduced parameter subset. By performing actual runs of patient-specific parameter estimation using quasi-random Monte Carlo simulations, the quality of estimation using different parameter subsets can be assessed and compared. Using the diaphony [10] obtained from quasi-random Monte Carlo simulations, the relative importance of parameters can be determined, which guides the subset reduction. Particle Swarm Optimization (PSO) [11,12] can be used for parameter estimation. Because the subset reduction is based on the size of parameter input space, results are biased. By comparing the estimations following from PSO, the subset reductions are validated independent of input space size.”

The goal of this study is to introduce a parameter reduction and estimation framework allowing personalization of models with many parameters. Though this approach is more widely applicable, we focus on the identification of the best subset of model parameters essential to accurately simulate patient-specific RV deformation using the CircAdapt model. This framework reduces the parameter subset in two steps based on importance and identifiability. First, the Morris Screening Method (MSM) was applied to exclude the unimportant parameters given the choice of model output and model structure. Second, a quasi-Monte Carlo (qMC) fitting algorithm was used on the reduced parameter subset to determine the parameters that are identifiable by comparing simulate RV deformation curves to measured RV deformation in AC-related mutation carriers. Parameter reduction was done based on the importance and identifiability of the parameters and validated using PSO.

Methods

Patient Cohort

A total of 15 AC subjects (6 males and 9 females, age 21.0 ± 15.2 years) were included in this study. The subjects were selected from a larger cohort from the University Medical Center Utrecht, which has been previously described in more detail by Mast et al. [5]. The study was approved by the local institutional ethics review board. The selected cohort was ensured to contain subjects with PKP2 and DSG2 mutations and to cover a wide range of AC disease severity according to the 2010 TFC [4]. Six of the included subjects were in a concealed stage, four showed electrical criteria, and five also showed structural criteria.

The echocardiographic protocol has been described in more detail elsewhere [13]. In brief, all data were obtained on a Vivid 7 or Vivid E9 ultrasound machine (GE Healthcare, Horten, Norway) using a broadband M3S transducer. All echocardiographic studies were analysed for structural abnormalities fulfilling 2010 TFC [4]. To quantify myocardial deformation, the conventional apical 2-, 3- and 4-chamber views and the RV-focused 4-chamber view were stored for offline left ventricular (LV) and RV deformation analysis by a single operator, blinded for clinical data. Two-dimensional speckle tracking was performed using EchoPAC version 202 (GE Healthcare, Horten, Norway), in order to obtain longitudinal strain curves of the LV free wall (LVfw), inter-ventricular septum (IVS), and the apical, mid, and basal segment of the RV free wall (RVfw). LV strain curves were acquired according to the standardized 18-segment model [14]. For IVS deformation, the 6 regional septal strain curves were averaged. For the LVfw deformation, the remaining 12 curves were averaged. The “Measurements” panel of Figure 3.1 shows an example of measured deformation, whereby decreasing longitudinal strain corresponds to shortening of the tissue and increasing strain to lengthening.

Cardiac Mechanics Model: the CircAdapt Model

The CircAdapt model is a lumped parameter model simulating haemodynamics and wall mechanics of the heart and circulation. The one-fibre model links global haemodynamics to local wall tension by assuming spherical walls [15]. The simplified ‘TriSeg’ ventricular geometry couples the LVfw and RVfw via the IVS allowing inter-ventricular interactions [16]. The ‘MultiPatch’ module [7] subdivides the RVfw into three segments with equal wall tension, allowing heterogeneity in tissue properties within the RVfw. No abnormal LVfw and IVS strains were found in the cohort. Therefore, tissue properties in the IVS and LVfw were assumed homogeneous and, thus, the tissue was modelled as a single segment representing the mechanics of the entire wall. Phenomenological models of active and passive myofibre stress generation were used to describe tissue mechanics of each wall segment [7].

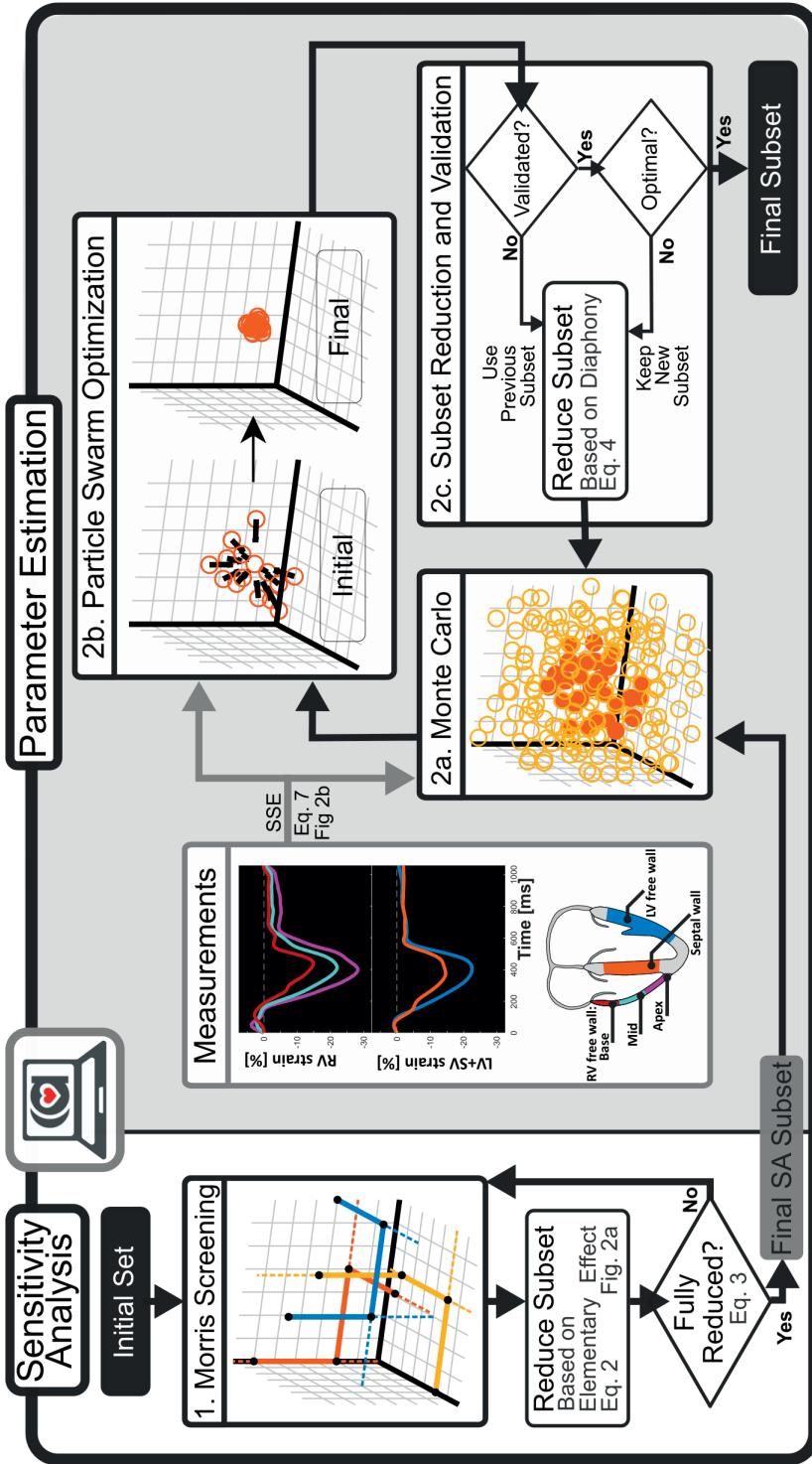


Figure 3.1.: Visualization of the two-step approach. In the first step, Sensitivity Analysis (SA) is performed using the Morris Screening method, which is applied iteratively on the CircAdapt model. Based on the elementary effect, a parameter selection is done. The final SA subset is used in quasi-Monte Carlo. Using the best estimations for each patient from quasi-Monte Carlo as a starting point, Particle Swarm Optimization is applied. Based on PSO results, the previous reduction is validated. Using the diaphony, the subset is further reduced.

A total of 110 CircAdapt parameters were identified and included in the analysis. This set consists of a group of 60 ventricular parameters (i.e. 12 parameters for each of the 3 RVfw segments, the IVS, and the LVfw) and a group of 50 parameters belonging to the other non-ventricular modules of CircAdapt, such as pulmonary and systemic circulations, valves, and atria. All parameters are presented, along with their value range, in Supplemental Table S3.1. The parameter input-space was based on reference values as used in previous work [7]. Because AC is mostly affecting myocardial tissue properties in the RV basal region in this cohort [5], a wide range was assigned to parameters describing tissue properties in both the RV midventricular and basal segment. In contrast, a smaller range was assigned to all other parameters to account for inter-subject variability.

Engineering strain of the sarcomere was extracted from the model and compared with measured strain. In measured strain, the reference length was taken as the length at the onset of the QRS complex, which was obtained using an electrocardiogram. To calculate engineering strain in the model, the reference length was defined as the length at the estimated onset of the QRS complex as done in previous studies [17].

Two-Step Parameter Subset Reduction Approach

Figure 3.1 shows an overview of the methodology used for parameter subset reduction. We applied a two-step approach composed of screening in the first step and parameter estimation and reduction in the second. This framework works with normalized input and uses the output of the model for subset reduction. Therefore, the framework is invariant of the CircAdapt model and could be applied to various other models.

In the first step, we performed MSM iteratively to screen the input-space and eliminate unidentifiable parameters given the chosen input-space size of the model as well as the chosen output measures. In the second step, we performed qMC simulations to identify preferred areas within the sample input-space (i.e. the best realisations) where the modelled strain was close to the measured strain. These areas indicated the identifiability of the parameters relative to the input-space, where unidentifiable parameters are expected to be distributed uniformly and identifiable parameters are expected to have a preferred area. Using these results, the parameter subset was reduced by omitting non-identifiable parameters. We applied PSO for accurate parameter estimation to validate the reduced subset whether the reduction was not induced by the choice of the input-space size. This is done by comparing the average goodness of fit of the cohort, obtained with different parameter subsets. MSM and PSO were repeated until further reduction was not beneficial.

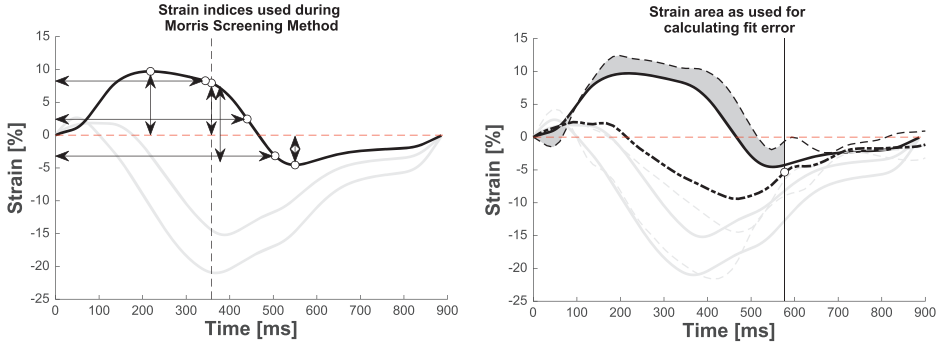


Figure 3.2: (a) Strain indices for one strain curve as used in Morris Screening Method. The same indices are included for the three RVfw segments, as well the LVfw and IVS segment. The indices are time to 10%, 50%, and 90% shortening (1,2,3), prestretch (4), systolic strain (5), post-systolic strain(6), and peak strain (7). The vertical dashed line indicates closure of the pulmonary valve. (b) Area used to calculate fit error X^2 . Area is defined from onset of QRS to 50% relaxation (white dot with vertical line) of the global RVfw strain (thick dashed line) and is calculated for all three RVfw segments, as well the LVfw and IVS segment. For the actual fit error, the area for all three RVfw segments, LVfw segment, and IVS segment are included.

Step 1: Sensitivity Analysis using Morris Screening Method

MSM was used to identify parameters that are unimportant to the model output, irrespective of the input-output space response with respect to linearity, monotonicity, and additivity [8]. A subset of relevant parameters was identified for each model output. As model output, we selected the metrics as shown in Figure 3.2a, which together describe the morphology of regional strain patterns. These metrics are time to 10%, 50%, and 90% total shortening (1,2,3), pre-stretch (4), systolic strain (5), post-systolic strain (6), and peak strain (7).

The input-space $\Omega = \mathbb{R}^D$ was spanned by all model parameters (initially, $D = 110$, for which their domains were linearly normalized to a range from 0 to 1 resulting in dimensionless parameters. Upper and lower bounds are shown in Supplemental Table S3.1. The input-space was discretized into a z -level grid ($z = 8$) with points $x_i \in \{0, \frac{1}{z-1}, \dots, 1\}$ and $i \in \{1, 2, \dots, D\}$. Each trajectory started at a randomly chosen point on the grid and changed parameter values in random order one-at-a-time with step-size $\Delta = \frac{1}{2} \frac{z}{z-1}$, such that all points on the grid were equally likely to be included [8]. CircAdapt was used to calculate each output y_j for each input point x .

The elementary effect E of parameter i on output j in trajectory r is given by

$$E_{ij}(r) = \frac{Y_j(x + e_i \Delta) - Y_j(x)}{\Delta}, \quad 3.1$$

with x any point in the z -level grid, and e_i the unit vector in direction i . To quantify the total elementary effect, the absolute average μ_{ij}^* of all trajectories N_r [9], with $r \in \{1, 2, \dots, N_r\}$ is calculated as

$$\mu_{ij}^* = \frac{1}{N_r} \sum_{r=1}^{N_r} E_{ij}(r), \quad 3.2$$

This elementary effect sensitivity measure μ_{ij}^* is considered a proxy of the variance-based total sensitivity index [9]. Consequentially, unimportant parameters could be considered insensitive to the model output and therefore omitted from the parameter subset. A parameter input X_i was considered to be unimportant if it is unimportant for all output Y_j , i.e.

$$\mu_{ij}^* < \frac{1}{D} \sum_{k=1}^D \mu_{kj}^* \forall j \quad 3.3$$

We aimed for 1000 successfully completed trajectories to represent the entire input-space. Convergence check was done using a leave-one-out method on all trajectories, i.e. when omitting one trajectory, the total set of sensitive parameters should not change. A new subset including all relevant parameters was defined. MSM was repeated until no parameters could be omitted to reduce the input-space as much as possible, which resulted in the final sensitivity analysis subset (see Figure 3.1).

Step 2a: Parameter Estimation using Quasi-Monte Carlo

The simulations obtained with qMC were used to identify preferred areas in the input-space which best described the cohort data and thereby identified the parameters that have the most influence on the fits within the chosen input-space size. In this step, the model output was compared to the measured strain. Within the input-space, one million quasi-random simulations were performed for which the input samples were generated using the Sobol low-discrepancy sequence [18].

For each patient, the fit error as described below was calculated for each simulation. Because simulations may become numerically unstable in case of non-physiological parameter combinations, the error for these crashed simulations was set to infinite. For each parameter subset for each patient, a distribution plot containing the best 100 simulations was made for visualisation of the input-space for these simulations. To quantify parameter preference, the diaphony d_i [10] of the best $N_b = 100$ simulations for each patient was calculated for each parameter i as

$$d_i = \left| \frac{1}{N_b} \sum_{N_b} e^{i2\pi x_i} \right| \quad 3.4$$

Thereby, the diaphony was used as a measure for homogeneity, with $d_i = 0$ for a completely homogeneously distributed sample set and $d_i = 1$ when all parameters had the same value.

Step 2b: Parameter Estimation using Particle Swarm Optimization

Unless qMC runs with a very large number of samples, the qMC estimations do not find an accurate fit due to the large input-space and can only be used to find trends in parameter preference. For validation of the parameter subset reduction based on qMC, the global minimum of each subset should be found and compared. For this purpose, PSO was applied [11,12].

PSO is an evolutionary algorithm, where a population of candidate solutions move through the input-space driven by their own history and the history of the population. For PSO, the simulations with least fit error from qMC were used as starting points to improve the initial solution guess. Initially, the speed was set to zero. During each iteration, a dimensionless velocity $\mathbf{v}_{t,k}$ of particle k was updated depending on its previous velocity and the distance to the local and global minima, by using

$$\begin{aligned} \mathbf{v}_{t+1,k} = & w \cdot \mathbf{v}_{t,k} + c_1 \cdot \mathbf{Z}_1 \cdot (\mathbf{x}_{t,k} - \mathbf{x}_{p_{t,k}}) \\ & + c_2 \cdot \mathbf{Z}_2 \cdot (\mathbf{x}_{t,k} - \mathbf{x}_{t,g}) \end{aligned} \quad 3.5$$

with $\mathbf{x}_{t,k}$ the dimensionless location of particle k at time t , $\mathbf{x}_{p_{t,k}}$ its local optimum, $\mathbf{x}_{t,g}$ the swarms optimum, w the inertia damping factor, c_1 and c_2 the inertia constants to change the velocity towards the local and global optimum, and \mathbf{Z}_i a vector with random numbers following the standard uniform distribution $\mathbf{Z} \in \mathcal{U}(0,1)$. The same settings were chosen as used by Eberhart and Shi [19], i.e. a population size of 30, and using dimensionless constant values which met Clerc's constriction method to enforce convergence [20], i.e. $w = 0.279$ and $c_1 = c_2 = 1.49445$.

The fit error was set to be infinite when the particle was outside the defined parameter space (Supplemental Table S3.1) to ensure physiological values. We assumed a particle k converged when the dimensionless "energy" was below 0.1 for all particle. The energy of a particle was defined as

$$E_k = \mathbf{v}_k^2 + (\mathbf{x}_{t,k} - \mathbf{x}_{p_k})^2 + (\mathbf{x}_{t,k} - \mathbf{x}_g)^2 \quad 3.6$$

Simulations were stopped when all particles converged, or when the limit of 1,000 iterations was reached.

Step 2c: Subset Validation and Reduction

Using the fit error X^2 resulting from PSO, previous subset reduction was validated. If the fit error X^2 in the reduced subset was similar to that in the larger subset, the reduced subset was accepted and further reduction was applied. If not, another reduction of the

previous subset was performed. The subset was considered optimal when all parameters were identifiable and thus no further reduction could be made.

Reduction of the subset was based on the diaphony, which was calculated for each parameter in each patient separately. For each parameter, the maximum diaphony of the subjects is used. The parameters with the lowest diaphony were omitted in the new subset.

Fit Error

In MSM, no patient data was included and strain indices were identified to find the identifiability of model parameters to these indices. In qMC and PSO, however, patient data was included. As discussed before, it is unknown which combination of strain indices fully captures the myocardial strain patterns in all segments. To avoid that the parameter reduction is influenced by the choice of the strain indices, the whole strain curve of all segments was used to compute the fitting error. To reduce the effect of drift in the measurement, only strain from the onset of the QRS-complex up to 50% of relaxation of the global RV strain was included as shown in Figure 3.2.

The fit error as used in qMC and PSO is composed of the squared error of each segment, A_{set}^2 , which uses the difference in modelled strain $\epsilon_{model,seg}$ and measured strain $\epsilon_{meas,seg}$ and is defined by

$$A_{seg}^2 = \int_{t_{onsetQRS}}^{t_{50relax}} (\epsilon_{model,seg} - \epsilon_{meas,seg})^2 dt. \quad 3.7$$

From preliminary studies, it is known that if modelled and measured RV strain match, modelled LVfw and IVS strain curves do not necessarily have to match the measured data. Therefore, we not only used all three RVfw segments but also constrained the strain of IVS and LVfw to fit.

The fit error also contains the error in cycle time. The cycle time T [s] was included in the input-space to perform one qMC for all AC datasets. Therefore, the squared difference between modelled and measured cycle time T [s] was included in the fit error (X^2), which is defined as

$$\begin{aligned} X^2 = & \alpha (A_{RVapex}^2 + A_{RVmid}^2 + A_{RVbase}^2 \\ & + A_{IVS}^2 + A_{LVfw}^2) \\ & + \beta \cdot (T_{model} - T_{meas})^2 \end{aligned} \quad 3.8$$

with $\alpha = 1s^{-1}$ and $\beta = 0.1s^{-2}$.

Numerical Implementation

To reduce computational cost, a C++ version based on the CircAdapt model as in Walmsley et al. [7] was used was developed. Equations were linearized using the Newton-Raphson method and were time-integrated using the Adams-Bashford method with a variable timestep Δt with $\max(\Delta t) = 2ms$. All other coding, including MSM, qMC, and PSO, was done in MATLAB 2018a (MathWorks, Natick, MA, USA). Simulations were run on a PC with 16 GB RAM and an Intel i7-8700 (3.2 GHz, 6 cores).

Results

Morris Screening Method

Out of 3000 trajectories, 1014 were successful in the sense that all simulations converged. Non-converged simulations had numerical instabilities due to parameter value combinations being non-physiological. In the successful trajectories, 48 parameters were relevant for all strain indices. Especially tissue properties of the ventricles were important to describe ventricular strain. Relative parameters were not dependent on one single trajectory, i.e. by leaving one trajectory out, the same parameters remained important.

The second screening step used 2500 trajectories, of which 1064 were successful. In this step, three parameters were unimportant and were omitted. The third step used 2000 trajectories and 1016 were successful. In this step, only one parameter was unimportant. Because the computational cost outweighed the expected parameter reduction, no further screening was done. Remaining parameters in the final subset after screening were all related to LVfw, IVS, or RVfw tissue properties except for one parameter related to the left atrium.

Subset Reduction: Quasi-Monte Carlo & Particle Swarm Optimization

One million qMC simulations were run multicore with a total computational time of 4 days for each subset. Computational time of PSO that ran single-core was approximately 8 hours for each subject.

For the initial qMC subset, we added 5 parameters in the RV wall to the 48 parameters remaining from MSM to ensure that all three segments had the same properties. This resulted in a total of 53 parameters (par53). For par53, the success rate of simulations was 97%. Other simulations had numerical instabilities due to similar reasons as in MSM. The minimum diaphony was 0.0674, the maximum diaphony was 0.9722. The SSE of the best estimation of qMC and PSO are shown in Figure 3.3. As expected, all fit errors X^2 from PSO were lower than those from qMC.

The first reduction omitted the remaining atrial parameter, the relaxation time constant of the LVfw and IVS, the shortening velocity in the LVfw, wall volume of the three RVfw segments, and a passive stiffness-related parameter in the three RVfw patches, resulting in 40 parameters (par40). The success rate was 98%, and the best 100 realisations had a minimum and maximum diaphony of 0.12 and 0.97.

The second reduction omitted LVfw and IVS volume, the contraction time constant in the three RVfw patches, shortening velocity in the three RVfw patches, and mean arterial pressure, resulting in 31 parameters (par31). The success rate was 98%. The minimum diaphony was 0.080 and the maximum diaphony was 0.97.

The third reduction omitted the contraction time constant in the LV, and the zero-stress sarcomere length in IVS and the three RVfw patches, resulting in 26 parameters (par26). The success rate was 98%. The minimum diaphony was 0.10 and the maximum diaphony was 0.97.

In the fourth reduction, the linear stiffness component of the three RVfw patches was omitted, resulting in 23 parameters (par23). The success rate was 97%. The minimum and maximum diaphony were 0.13 and 0.97, respectively.

In a fifth step, all LVfw and IVS parameters were removed, resulting in 16 parameters (par16). For this set, the success rate was 96% with the minimum and maximum diaphony 0.098 and 0.97, respectively.

The minimum error in qMC and the error of the global minimum of the PSO for the subsets par53, par26, par23, and par16 are shown in Figure 3.3. By decreasing the parameter subset size, the average error of qMC decreased for all subsets. By applying PSO, the mean X^2 decreased for all subsets compared to the X^2 after qMC. Decreasing the number of parameters increased the mean X^2 from 14 in par53 to 21 in par23 after applying PSO. Removing LVfw parameters from par23 to par16 resulted in the largest increase in X^2 from 21 in par23 to 29 in par16 after applying PSO.

Fits

An example strain fit for each of the subsets par53, par23, and par16 is shown in Figure 3.4. In par53, par23, and par16, modelled strains are still similar to measured strains despite the increase in fit error. In the par23 and par16, RV strain fit quality is similar. By eyeballing, all parameter subsets are able to capture the strain morphology. The qMC distribution and PSO estimations of these fits are shown in Figure 3.5. Estimated parameter values in par16 are similar to the estimated parameters in the larger subsets.

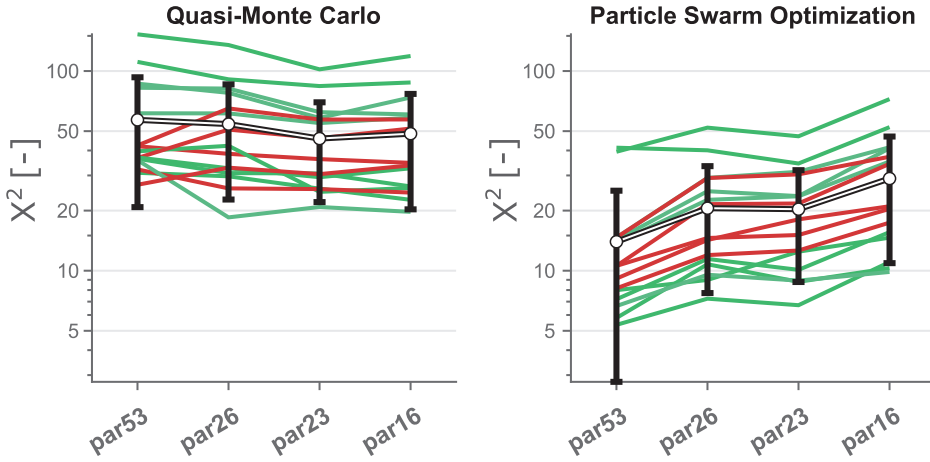


Figure 3.3: Minimum Summed Squared Error (X^2) after quasi-Monte Carlo (left) and after Particle Swarm Optimization (right) of the subsets, where parX indicates the number of parameters included. Green lines indicate subjects in the concealed stage, the light and dark red lines indicate subjects in the electrical and structural stage. Black-white lines show the average summed squared error of all subjects including standard deviation.

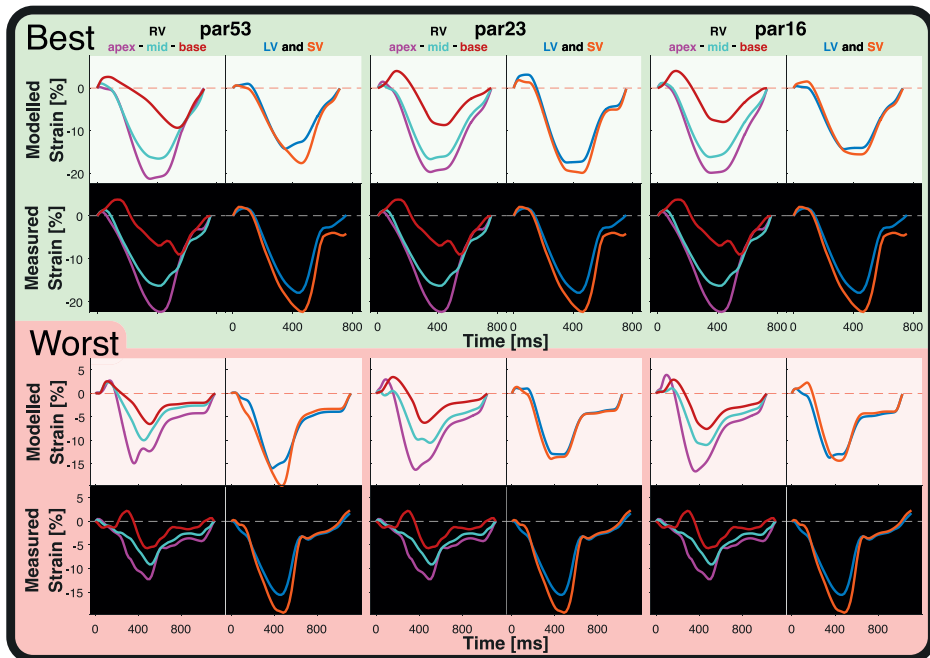


Figure 3.4: Example fits from Particle Swarm Optimization of par53 (left), par23 (middle), and par16 (right) of the best fit (top; subject 12) and worst fit (bottom; subject 14) of subjects with abnormal strain. For subject 12, the summed squared error was 8.2, 13, and 17 for par53, par23, and par16, respectively. For subject 14, the summed squared error was 14, 30, and 37, respectively.

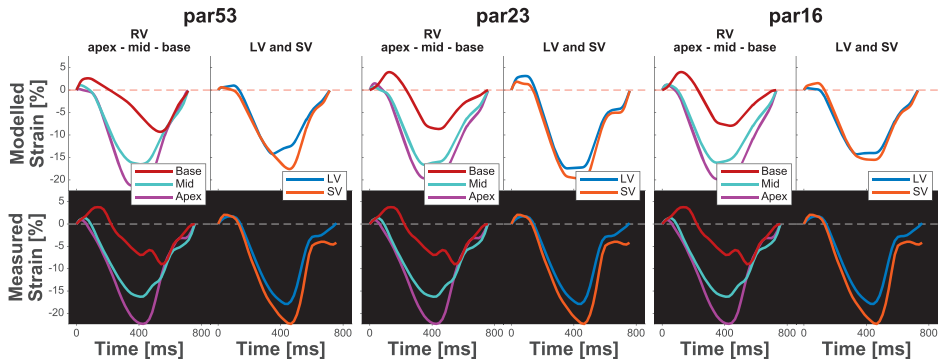


Figure 3.5: Normalized Estimations resulting from quasi-Monte Carlo (qMC) and Particle Swarm Optimization (PSO) of subject 12 (top) and subject 14 (bottom) of the subset with 53, 23, and 16 parameters (par53, par23, and par16, respectively). Included parameters are indicated by the yellow bars. The best 100 simulations from qMC are shown in grey, the global optimum from PSO is shown in the thick black-white line.

Discussion

We successfully designed a new framework to find non-identifiable parameters and to select and estimate a small subset of identifiable parameters from the CircAdapt model to simulate regional RV tissue deformation in AC mutation carriers. This subset could be used to simulate patient-specific RV strain in AC mutation carriers revealing specific regional heterogeneities of RV tissue properties. This selection is done in a two-step approach. First, using MSM, the number of parameters successfully reduced from 110 to 48. Second, using qMC and PSO, the subset was further reduced to 23 parameters, including local contractility, passive stiffness, activation delay, and wall reference area of LVfw, IVS, and RVfw as well as cardiac output, heart rate, AV-delay, and relative systole duration (i.e. myofibre twitch duration). Further reduction to 16 parameters resulted in an unrealistic subset in which LVfw and IVS parameters were excluded.

Morris Screening Method allows Reduction of the Parameter Subset

It is demonstrated that Morris Screening is a successful method to identify unimportant parameters in cardiovascular models. Donders et al. found that 16 out of 73 parameters were important in a model for brachial flow and systolic radial pressure using MSM [21]. MSM has also been applied to an LV finite-element model [22] to investigate the effect of model parameters on local strain. A total of 3 parameters in 16 segments were included in the sensitivity analysis, but the model contained many more parameters. The authors only included measured time to peak strain, decreasing the complexity of the problem.

In this study, MSM removed over half of all parameters in three screening rounds. The relevance of a parameter depends on its own behaviour but also on the chosen parameter value range. Since simulations in the three screening rounds were not compared to the

measurements, we could not validate the chosen range. Therefore, the relevance of some parameters might be under- or overestimated. We presumed that parameters identified by MSM as non-identifiable were not important to model patient-specific strain in AC-related mutation carriers because AC is a myocardial pathology and all ventricular tissue-related parameters were still in the subset. On top of that, in a preliminary one-at-a-time study (results not shown), these parameters did not influence strain significantly compared to parameters related to the pathology. Based on these observations, we concluded that we did not miss out any important parameters in the subset resulting from MSM.

Quasi-Monte Carlo and Particle Swarm Optimization allows Further Reduction based on Clinical Strain

Further decrease in the number of parameters was done by applying qMC. Validation was done with PSO. Within the smaller subsets par23 and par16, all parameters were identifiable and therefore, the subset is usable for patient-specific parameter estimation. For these subsets, modelled strain sufficiently resembled the measured strains.

PSO has been previously used for parameter estimation in a study by Mineroff et al. [23], who interestingly, also used the CircAdapt model. They used the CircAdapt model to model volumes and pressures in the cardiac cycle and showed that PSO is a suitable algorithm for patient-specific estimation of parameters in the CircAdapt model. A total of 9 parameters were estimated combining cardiac tissue properties and circulation parameters

Although only a small part of the input-space has been explored by qMC, trends in parameter values can be seen already in the largest subset (par53). In the smaller parameter sets (par31, par26, par23, par16), there were more parameters with a larger diaphony, suggesting the model converged to a unique point.

Selected Parameters may describe AC Disease Progression

Parameters included in the final subset (par23) are likely to be related to AC disease progression. As earlier hypothesized, our framework selects contractility and stiffness as important parameters for describing strain in AC mutation carriers. The parameter SfAct scales the active force generation and is a measure for contractility. The parameter k1 scales the passive stress nonlinearly and is a measure for stiffness. Because disease progression in AC mutation carriers has been found to be associated with functional and structural myocardial changes (e.g. fibro-fatty replacement of myocytes [1], altered calcium handling [24], and fibrosis [25]), contractility and stiffness are likely to change during disease progression. Activation delay dT is in this model defined as the difference in time of activation between the segments and the IVS, whereas the activation of IVS is set to be the model's atrioventricular delay. Abnormal electrical activation is found in AC subjects [26] and therefore, it is important to include it in the final subset. It is known

that altered activation delay is related to AC disease. The remaining four parameters in the final subset par23 were heart rate, cardiac output, relative systole duration, and atrioventricular delay. All these parameters have an influence on ventricular mechanics during both ejection and filling (preload) and are therefore important for patient-specific modelling of strain.

The parameter subset reduction is applied to the CircAdapt model, which has a low computational cost. The final parameter subset is inherent to the CircAdapt model, although, it could give insight in which tissue properties should indicate to model AC disease substrates in more complex models such as three-dimensional electro-mechanical cardiac models ([27,28]). These models are computationally more expensive compared to the CircAdapt model, so applying our parameter reduction framework would increase the computational cost and patient-specific parameter would be challenging. These more complex models, however, could give more insight in the mechanisms playing a role on a more local scale.

Limitations

In this study, we compare measured longitudinal strain with simulated strain along the myofibre. Because RV subendocardial myofibres are predominantly directed longitudinally [29], it is assumed that any potential difference between the two is negligible.

The objective function to minimize the error between measured and modelled strain is an important choice for fit quality and computational time. In this study, we did not investigate how to optimize the objective function, and therefore we used the area between measured and modelled strain curves. By using this objective function, we did not correct for any measurement errors, such as time-misregistration between the four echo views, beat-to-beat variability or inter- and intra-observer variability. Future studies could investigate how to design an objective function using strain indices or other measurements, such as valve timings, blood flow velocity, or ejection fraction, to develop a more efficient fitting algorithm with an objective function invariant of measurement uncertainties. This should result in potentially better fits.

Future Work

This study focusses on the development of a platform enable to reduce the number of model parameters while conserving the model's ability to simulate measured strain and is not designed to draw any conclusions on the clinical applications of fitting of deformation curves. Future work will focus on optimizing the parameter estimation algorithm regarding computational time and assess the accuracy and precision of the fits. This allows us to apply parameter estimation on a larger cohort which might expand our knowledge about the disease and its progression.

Accuracy of the parameter estimation algorithm could be estimated by repeating the algorithm to determine the precision, and by using synthetic data for determining trueness. Both are assessable using the parameter estimation framework. Using ground truth measurements for determining trueness instead of synthetic data is more difficult or even impossible. Firstly because we used a lumped parameter model, whereby the parameters are the lumped effect of the tissue and secondly because these ground truth measurements are challenging to obtain. While estimated regional mechanical activation delays can potentially be compared to non-invasive or invasive electrical mapping data, it is challenging to compare regional passive and contractile tissue function parameters to ground truth measurements. Because these tissue properties are not directly measurable, our inverse modelling approach could give more insight into the underlying substrate.

Other measurements, such as voluminal information or valvular flows, may have added value to our framework and might improve accuracy and precision. However, this requires reassessment of parameter sensitivity and identifiability and more parameters might remain in the final parameter subset increasing the complexity of parameter estimation. Future work will show whether sufficient predicting information is captured from strain, or whether more complexity is necessary.

Although recent studies have demonstrated good reproducibility of echocardiographic RV strain measurements [5,30,31], future studies should quantify the uncertainty of the parameter estimation caused by inter- and intra-observer variability of RV strain measurements

In this cohort, neglecting LVfw and IVS parameters (from par23 to par16) only had a small influence on parameter estimation. However, by not estimating LVfw and IVS tissue properties, no abnormalities in these walls could be found. In later stadia of the disease and in other cohorts with other mutations, AC is also expressed with LV involvement [32]. Therefore, par23 rather than par16 was considered the final subset.

Conclusion

To identify the set of parameters needed for patient-specific modelling of RV myocardial disease in AC mutation carriers using the CircAdapt model, we set up a framework for parameter subset reduction. Using MSM and qMC, we successfully reduced the number of parameters from 110 to 23. The final subset includes regional tissue contractility, passive stiffness, activation delay, and wall size. By estimating these parameters using PSO, the CircAdapt model was still able to accurately simulate strain in AC-related mutation carriers. Future work should use strain indices instead of the whole curve to optimize the fitting algorithm. This will allow us to apply the algorithm on larger cohorts, as well as to relate estimated parameters to disease progression and outcome.

References

1. Basso C, Corrado D, Marcus FI, Nava A, Thiene G. 2009 Arrhythmogenic right ventricular cardiomyopathy. *Lancet* **373**, 1289–1300. (doi:10.1016/S0140-6736(09)60256-7)
2. Thiene G, Nava A, Corrado D, Rossi L, Pennelli N. 1988 Right Ventricular Cardiomyopathy and Sudden Death in Young People. *N. Engl. J. Med.* **318**, 129–133. (doi:10.1056/NEJM198801213180301)
3. Groeneweg JA *et al.* 2015 Clinical Presentation, Long-Term Follow-Up, and Outcomes of 1001 Arrhythmogenic Right Ventricular Dysplasia/Cardiomyopathy Patients and Family Members. *Circ. Cardiovasc. Genet.* **8**, 437–446. (doi:10.1161/CIRCGENETICS.114.001003)
4. Marcus FI *et al.* 2010 Diagnosis of Arrhythmogenic Right Ventricular Cardiomyopathy/Dysplasia: Proposed Modification of the Task Force Criteria. *Eur. Heart J.* **31**, 806–814. (doi:10.1093/eurheartj/ehq025)
5. Mast TP *et al.* 2016 Right Ventricular Imaging and Computer Simulation for Electromechanical Substrate Characterization in Arrhythmogenic Right Ventricular Cardiomyopathy. *J. Am. Coll. Cardiol.* **68**, 2185–2197. (doi:10.1016/j.jacc.2016.08.061)
6. Mast TP *et al.* 2019 The Prognostic Value of Right Ventricular Deformation Imaging in Early Arrhythmogenic Right Ventricular Cardiomyopathy. *JACC Cardiovasc. Imaging*, 14 March. **12**, 446–455. (doi:10.1016/j.jcmg.2018.01.012)
7. Walmsley J, Arts T, Derval N, Bordachar P, Cochet H, Ploux S, Prinzen FW, Delhaas T, Lumens J. 2015 Fast Simulation of Mechanical Heterogeneity in the Electrically Asynchronous Heart Using the MultiPatch Module. *PLoS Comput. Biol.* **11**, 1–23. (doi:10.1371/journal.pcbi.1004284)
8. Morris MD. 1991 Factorial Sampling Plans for Preliminary Computational Experiments. *Technometrics.* **33**.
9. Campolongo F, Cariboni J, Saltelli A. 2007 An effective screening design for sensitivity analysis of large models. *Environ. Model. Softw.* **22**, 1509–1518. (doi:10.1016/j.envsoft.2006.10.004)
10. Hornfeck W, Kuhn P. 2015 Diaphony, a measure of uniform distribution, and the Patterson function. *Acta Crystallogr. Sect. A Found. Adv.* **71**, 382–391. (doi:10.1107/S2053273315007123)
11. Kennedy J, Eberhart R. In press. Particle swarm optimization. In *Proceedings of ICNN'95 - International Conference on Neural Networks*, pp. 1942–1948. IEEE. (doi:10.1109/ICNN.1995.488968)
12. Shi Y, Eberhart R. 1998 A modified particle swarm optimizer. *IEEE*, 69–73. (doi:10.1109/icec.1998.699146)
13. Teske AJ, De Boeck BW, Melman PG, Sieswerda GT, Doevendans PA, Cramer MJ. 2007 Echocardiographic Quantification of Myocardial Function using Tissue Deformation Imaging, a Guide to Image Acquisition and Analysis using Tissue Doppler and Speckle Tracking. *Cardiovasc. Ultrasound.* **5**, 27. (doi:10.1186/1476-7120-5-27)
14. Voigt JU *et al.* 2015 Definitions for a common standard for 2D speckle tracking echocardiography: consensus document of the EACVI/ASE/Industry Task Force to standardize deformation imaging. *Eur. Heart J. Cardiovasc. Imaging* **16**, 1–11. (doi:10.1093/ehjci/jeu184)
15. Arts T, Bovendeerd PH, Prinzen FW, Reneman RS. 1991 Relation between left ventricular cavity pressure and volume and systolic fiber stress and strain in the wall. *Biophys. J.* **59**, 93–102. (doi:10.1016/S0006-3495(91)82201-9)
16. Lumens J, Delhaas T, Kirn B, Arts T. 2009 Three-wall segment (TriSeg) model describing mechanics and hemodynamics of ventricular interaction. *Ann. Biomed. Eng.* **37**, 2234–2255. (doi:10.1007/s10439-009-9774-2)
17. Van Everdingen WM *et al.* In press. Echocardiographic Prediction of Cardiac Resynchronization Therapy Response Requires Analysis of Both Mechanical Dyssynchrony and Right Ventricular Function: A Combined Analysis of Patient Data and Computer Simulations. (doi:10.1016/j.echo.2017.06.004)
18. Sobol' I. 1967 On the distribution of points in a cube and the approximate evaluation of integrals. *USSR Comput. Math. Math. Phys.* **7**, 86–112. (doi:10.1016/0041-5553(67)90144-9)
19. Eberhart RC, Shi Y. 2000 Comparing inertia weights and constriction factors in particle swarm optimization. In *Proceedings of the 2000 Congress on Evolutionary Computation, CEC 2000*, pp. 84–88. (doi:10.1109/CEC.2000.870279)
20. Clerc M, Kennedy J. 2002 The particle swarm-explosion, stability, and convergence in a multidimensional complex space. *IEEE Trans. Evol. Comput.* **6**, 58–73. (doi:10.1109/4235.985692)
21. Donders WP, Huberts W, van de Vosse FN, Delhaas T. 2015 Personalization of models with many model parameters: An efficient sensitivity analysis approach. *Int. j. numer. method. biomed. eng.* **31**, 1–18. (doi:10.1002/cnm.2727)

22. Le Rolle V, Galli E, Danan D, El Houari K, Hubert A, Donal E, Hernández AI. 2019 Sensitivity Analysis of a Left Ventricle Model in the Context of Intraventricular Dyssynchrony. *Acta Biotheor.* (doi:10.1007/s10441-019-09362-y)
23. Mineroff J, McCulloch AD, Krummen D, Krishnamurthy GA. 2019 Optimization Framework for Patient-Specific Cardiac Modeling. *Submitt. to Biomech. Model. Mechanobiol.* (doi:10.1007/s13239-019-00428-z)
24. van Opbergen CJM *et al.* 2019 Plakophilin-2 Haploinsufficiency Causes Calcium Handling Deficits and Modulates the Cardiac Response Towards Stress. *Int. J. Mol. Sci.* **20**, 4076. (doi:10.3390/ijms20174076)
25. Tandri H *et al.* 2005 Noninvasive detection of myocardial fibrosis in arrhythmogenic right ventricular cardiomyopathy using delayed-enhancement magnetic resonance imaging. *J. Am. Coll. Cardiol.* **45**, 98–103. (doi:10.1016/j.jacc.2004.09.053)
26. Haqqani HM, Tschabrunn CM, Betensky BP, Lavi N, Tzou WS, Zado ES, Marchlinski FE. 2012 Layered activation of epicardial scar in arrhythmogenic right ventricular dysplasia possible substrate for confined epicardial circuits. *Circ. Arrhythmia Electrophysiol.* **5**, 796–803. (doi:10.1161/CIRCEP.111.967935)
27. Kerckhoffs RCP, Neal ML, Gu Q, Bassingthwaighe JB, Omens JH, McCulloch AD. 2007 Coupling of a 3D finite element model of cardiac ventricular mechanics to lumped systems models of the systemic and pulmonary circulation. *Ann. Biomed. Eng.* **35**, 1–18. (doi:10.1007/s10439-006-9212-7)
28. Augustin CM, Neic A, Liebmann M, Prassl AJ, Niederer SA, Haase G, Plank G. 2016 Anatomically accurate high resolution modeling of human whole heart electromechanics: A strongly scalable algebraic multigrid solver method for nonlinear deformation. *J. Comput. Phys.* **305**, 622–646. (doi:10.1016/j.jcp.2015.10.045)
29. Kovács A, Lakatos B, Tokodi M, Merkely B. 2019 Right ventricular mechanical pattern in health and disease: beyond longitudinal shortening. *Heart Fail. Rev.* , 511–520. (doi:10.1007/s10741-019-09778-1)
30. Liu BY *et al.* 2019 Comparison of the capability of risk stratification evaluation between two- and three-dimensional speckle-tracking strain in pre-capillary pulmonary hypertension. *Pulm. Circ.* **9**. (doi:10.1177/2045894019894525)
31. Mahfouz RA, Gouda M, Arab M. 2019 Right ventricular mechanics and exercise capacity in patients with microvascular angina: The impact of microvascular function. *Echocardiography* , 71–76. (doi:10.1111/echo.14563)
32. Vives-Gilabert Y *et al.* 2019 Left ventricular myocardial dysfunction in arrhythmogenic cardiomyopathy with left ventricular involvement: A door to improving diagnosis. *Int. J. Cardiol.* **274**, 237–244. (doi:10.1016/j.ijcard.2018.09.024)

Supplemental Material

Table S3.1: Model parameters after Morris Screening. Continues on next page.

Parameter Name	Lower boundary	Upper boundary	par53	par40	par31	par26	par23	par16
SfAct RVapex	96kPa	144kPa	✓	✓	✓	✓	✓	✓
SfPas RVapex	18kPa	27kPa	✓	✓	✓	✓		
k1 RVapex	8	12	✓	✓	✓	✓	✓	✓
dT RVapex	-0.025ms	0.025ms	✓	✓	✓	✓	✓	✓
LsOPas RVapex	1.7µm	1.9µm	✓	✓	✓			
vMax RVapex	5.6µm/ms	8.4µm/ms	✓	✓				
TR RVapex	0.2ms	0.3ms	✓	✓				
TD RVapex	0.2ms	0.3ms	✓					
VWall RVapex	16.792mL	25.188mL	✓	✓	✓	✓	✓	✓
AmRef RVapex	3440mm2	5160mm2	✓					
dLsPas RVapex	0.48	0.72	✓					
SfAct RVmid	0kPa	120kPa	✓	✓	✓	✓	✓	✓
SfPas RVmid	11kPa	228kPa	✓	✓	✓	✓		
k1 RVmid	5	50	✓	✓	✓	✓	✓	✓
dT RVmid	-0.025ms	0.075ms	✓	✓	✓	✓	✓	✓
LsOPas RVmid	1.7µm	1.9µm	✓	✓	✓			
vMax RVmid	0.01µm/ms	7µm/ms	✓	✓				
TR RVmid	0.2ms	0.3ms	✓	✓				
TD RVmid	0.2ms	0.3ms	✓					
VWall RVmid	16.792mL	41.98mL	✓	✓	✓	✓	✓	✓
AmRef RVmid	3440mm2	5160mm2	✓					
dLsPas RVmid	0.01	1.2	✓					
SfAct RVbase	0kPa	120kPa	✓	✓	✓	✓	✓	✓
SfPas RVbase	11kPa	228kPa	✓	✓	✓	✓		
k1 RVbase	5	50	✓	✓	✓	✓	✓	✓
dT RVbase	-0.025ms	0.075ms	✓	✓	✓	✓	✓	✓
LsOPas RVbase	1.7µm	1.9µm	✓	✓	✓			
vMax RVbase	0.01µm/ms	7µm/ms	✓	✓				
TR RVbase	0.2ms	0.3ms	✓	✓				
TD RVbase	0.2ms	0.3ms	✓					
VWall RVbase	16.792mL	25.188mL	✓	✓	✓	✓	✓	✓
AmRef RVbase	3440mm2	5160mm2	✓					
dLsPas RVbase	0.01	1.2	✓					
LsOPas LA	1.7µm	1.9µm	✓					
SfAct LV	96kPa	144kPa	✓	✓	✓	✓	✓	
k1 LV	8	12	✓	✓	✓	✓	✓	
dT LV	-0.025ms	0.025ms	✓	✓	✓	✓	✓	
vMax LV	5.6µm/ms	8.4µm/ms	✓					
TR LV	0.2ms	0.3ms	✓	✓	✓			

Table S3.1 (continued)

Parameter Name	Lower boundary	Upper boundary	par53	par40	par31	par26	par23	par16
TD LV	0.2ms	0.3ms	✓					
VWall LV	76.808mL	115.212mL	✓	✓	✓	✓	✓	
AmRef LV	7840mm ²	11760mm ²	✓	✓				
SfAct SV	96kPa	144kPa	✓	✓	✓	✓	✓	
k1 SV	8	12	✓	✓	✓	✓	✓	
LsOPas SV	1.7µm	1.9µm	✓	✓	✓			
TD SV	0.2ms	0.3ms	✓					
VWall SV	25.888mL	38.832mL	✓	✓	✓	✓	✓	
AmRef SV	3920mm ²	5880mm ²	✓	✓				
p0	9.76kPa	14.64kPa	✓	✓				
q0	4.08L/min	6.12L/min	✓	✓	✓	✓	✓	✓
tCycle	0.6s	1.25s	✓	✓	✓	✓	✓	✓
dTauAv	-0.025ms	0.025ms	✓	✓	✓	✓	✓	✓
TimeFac	0.5	1.5	✓	✓	✓	✓	✓	✓

4



Electromechanical Substrate Characterization in Arrhythmogenic Cardiomyopathy using imaging-based patient-specific Computer Simulations

Based on: **Nick van Osta**^{*}, Feddo P. Kirkels^{*}, Aurore Lyon, Tijmen Koopsen, Tim van Loon, Maarten J. Cramer, Arco J. Teske, Tammo Delhaas, Joost Lumens
“Electromechanical substrate characterization in arrhythmogenic cardiomyopathy using imaging-based patient-specific computer simulations”
EP Europace, 23(Supplement_1), i153-i160 (2021)

^{*}NvO and FK contributed equally.

Abstract

Arrhythmogenic Cardiomyopathy (AC) is an inherited cardiac disease, characterized by life-threatening ventricular arrhythmias and progressive cardiac dysfunction. The aim of this study is to use computer simulations to non-invasively estimate the individual patient's myocardial tissue substrates underlying regional right ventricular (RV) deformation abnormalities in a cohort of AC mutation carriers.

In 68 AC mutation carriers and 20 control subjects, regional longitudinal deformation patterns of the RV free wall (RVfw), interventricular septum (IVS) and left ventricular free wall (LVfw) were obtained using speckle-tracking echocardiography. We developed and used a patient-specific parameter estimation protocol based on the multi-scale CircAdapt cardiovascular system model to create virtual AC subjects. Using the individual's deformation data as model input, this protocol automatically estimated regional RVfw and global IVS and LVfw tissue properties.

The computational model was able to reproduce clinically measured regional deformation patterns for all subjects, with highly reproducible parameter estimations. Simulations revealed that regional RVfw heterogeneity of both contractile function and compliance were increased in subjects with clinically advanced disease compared to mutation carriers without clinically established disease ($17\pm 13\%$ vs. $8\pm 4\%$, $p=0.01$ and $18\pm 11\%$ vs. $10\pm 7\%$, $p<0.01$, respectively). No significant difference in activation delay was found.

Regional RV deformation abnormalities in AC mutation carriers were related to reduced regional contractile function and tissue compliance. In clinically advanced disease stages, a characteristic apex-to-base heterogeneity of tissue abnormalities was present in the majority of the subjects, with most pronounced disease in the basal region of the RVfw.

Introduction

Arrhythmogenic cardiomyopathy is an inherited heart muscle disorder characterized by fibrofatty replacement of primarily the right ventricular (RV) myocardium, which predisposes to ventricular arrhythmias and sudden cardiac death in young individuals [1,2]. Variable disease expression is found in familial AC [3], ranging from sudden cardiac death (SCD) in young individuals to a lifelong absence of any phenotype. To prevent apparently healthy AC mutation carriers from SCD, early detection of potentially pro-arrhythmic tissue substrates is important.

Using speckle-tracking echocardiography, our groups [4] found distinct regional RV deformation abnormalities in AC mutation carriers. Predominantly the basal (subtricuspid) part of the RV free wall was affected, even in the absence of electrocardiographic or structural 2010 Task Force Criteria (TFC, [5]). Using computer simulations, it was hypothesized that these deformation abnormalities resulted from a decreased contractility and an increased stiffness within this segment. In a follow-up study, these RV deformation abnormalities were found to be associated with AC disease progression [6]. Another approach, as reported by Sarvari et al. [7] showed that RV mechanical dispersion, defined as the standard deviation in time-to-peak strain, is a marker for arrhythmic events in AC patients. The latter study demonstrate the prognostic value of RV longitudinal strain, while the disease substrates underlying the deformation abnormalities remain unknown. Together with the first study by Mast et al. [4], these studies suggest that identification of the disease substrate causing RV deformation abnormalities could be used to better understand disease progression and support risk stratification. Patient-specific characterization of the electromechanical disease substrates in early-stage AC may lead to better arrhythmic risk stratification and ultimately to the identification of possible therapeutic targets, thereby enabling personalized medicine. Since invasive tissue characterization is accompanied by important risks, and is rarely performed, non-invasive ways of tissue characterization should be investigated.

The aim of this study is to non-invasively estimate the pathophysiological substrates underlying regional deformation abnormalities in the individual AC mutation carrier, using imaging-based patient-specific computer simulations. We use a parameter estimation protocol based on a previously established framework [8] which simulates myocardial deformation to identify regional tissue properties.

Methods

Patient Cohort

This study was performed on a previously reported consecutive cohort of pathogenic desmosomal mutation carriers, who were evaluated at the UMC Utrecht in the Netherlands between 2006 and 2015 [4]. During this period, 87 subjects carrying a pathogenic plakophilin-2 (PKP2), desmoglein-2 (DSG2), or desmoplakin (DSP) mutation were evaluated. Additionally, 20 healthy volunteers were included as control subjects. The study was approved by the local institutional ethics review board.

The echocardiographic protocol has been detailed elsewhere [9]. Briefly, all echocardiographic data were obtained on a Vivid 7 or Vivid E9 ultrasound machine (GE Vingmed Ultrasound, Horten, Norway) using a broadband M3S transducer and were analysed for fulfilling 2010 TFC for structural abnormalities [5]. Only exams during sinus rhythm were eligible for inclusion. Conventional 2-, 3-, and 4-chamber views, as well as an RV-focused apical 4-chamber view, were used to visualize the RV lateral free wall (RVfw), interventricular septum (IVS), and LV free wall (LVfw). Cineloops were stored for offline two-dimensional speckle tracking using EchoPAC v. 202 (GE Vingmed Ultrasound, Horten, Norway). A single observer, blinded to clinical information, obtained segmental longitudinal strain curves of the RVfw and the LV.

In this study, we focussed on regional heterogeneity of RVfw tissue abnormalities because the RVfw is the most affected area in pathogenic desmosomal mutation carriers [10]. Therefore, three segmental deformation patterns of the RVfw (i.e. apical, mid-ventricular and basal) were used to personalize the computational model (Figure 4.1). Additionally, two global deformation patterns of the LVfw and IVS were used to ensure realistic mechanical boundary conditions for the RVfw in terms of ventricular interaction. Global LVfw and IVS deformation patterns were obtained by averaging the 12 LVfw and 6 IVS segmental deformation curves, respectively, using the standardized 18-segment model [11].

Cardiac magnetic resonance imaging (CMR) was performed on a 1.5-T scanner (Achieva, Philips Healthcare, Best, the Netherlands), according to standard AC protocols [12], and included measurements of the RV end diastolic volume, RV ejection fraction, and LV ejection fraction. LV stroke volume was used to personalize cardiac output (CO) in the computer simulations.

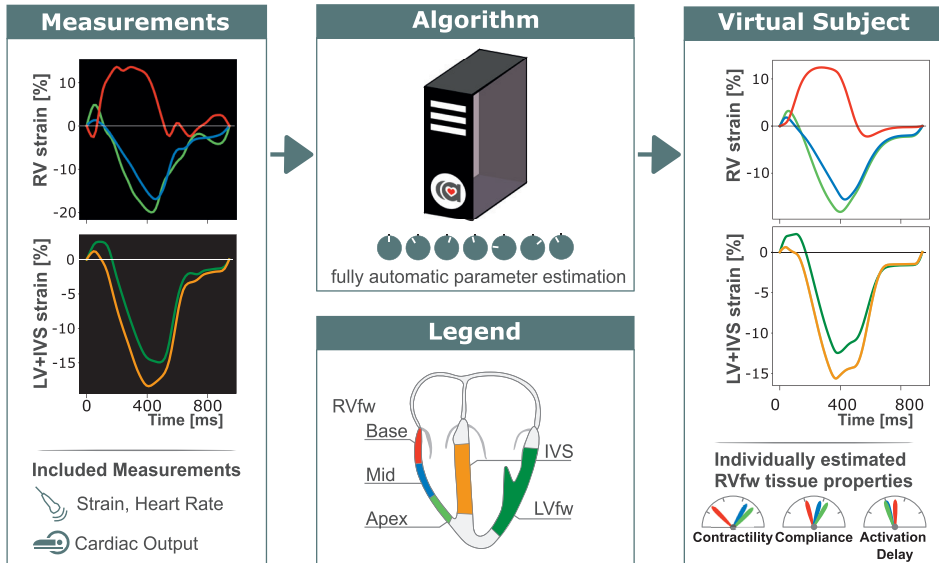


Figure 4.1: Methodology. Right ventricular (RV), interventricular septal (IVS), and left ventricular (LV) strain were obtained using speckle-tracking echocardiography, and cardiac output was obtained using cardiovascular magnetic resonance imaging (CMR). Using a fully automatic estimation protocol, virtual subjects reproducing the clinical measures were generated and local tissue properties were extracted.

For further analysis, RV disease substrates were categorized by three different non-invasive imaging approaches, which have been published previously:

1. following the revised 2010 TFC [5], AC can be divided into three consecutive clinical stages: a) subclinical (concealed) stage with absence of any 2010 TFC, except for harbouring a pathogenic mutation; b) electrical stage, with only electrocardiographic (ECG) or Holter abnormalities; and c) structural stage, with structural abnormalities on non-invasive imaging, regardless of the history of ventricular arrhythmias or presence of ECG or Holter abnormalities [5,13].
2. based on the pattern of basal RVfw deformation following the predefined criteria published by Mast et al. [4]. A Type-I pattern is defined as normal deformation; a Type-II pattern is characterized by delayed onset of shortening, reduced systolic peak strain and minor post-systolic shortening; a Type-III pattern is characterized by little or no systolic peak strain, predominantly systolic stretching and major post-systolic shortening;
3. based on RV mechanical dispersion (RVMD), an index of segmental heterogeneity in contraction in the RVfw and IVS. RVMD was calculated on 6 segments of the RV, including the IVS, and defined as the standard deviation of the segmental time intervals from onset Q/R on the surface ECG to peak negative strain [7]. A previously established cut-off value of 30ms [14] was used in this study to define a group with low and high RVMD.

Computer Simulations

Regional RV, IVS, and LV myocardial deformation were simulated using the CircAdapt model [15], which is a closed-loop lumped parameter computer model of the human heart and circulation. It enables simulation of cardiac haemodynamics and regional wall mechanics, using a phenomenological model describing active and passive myofibre mechanics [16]. Ventricular interactions are modelled using the TriSeg model using the concept of conservation of energy [17]. LVfw and IVS were modelled as a single segment representing the mechanics of the entire wall. Three RVfw segments representing the apical, mid-ventricular, and basal regions were modelled using the previously validated MultiPatch model [16].

Patient-Specific Simulation Protocol

Computer simulations were personalized by automatically tuning model parameters to optimize the modelled myofibre strain to measured longitudinal strain (Figure 4.1). A parameter subset with 21 parameters essential for modelling regional RVfw, IVS, and LVfw deformation in AC mutation carriers was previously identified [8] and shown in Supplementary Table S4.1. CO and heart rate (HR) were direct input parameters of the model and thereby set from the measurements. The former was obtained from CMR data, while the latter was obtained from the RV focused 4-chamber view. The other 19 parameters describe the size of the RVfw, IVS, and LVfw (3 model parameters), myocardial twitch duration and thus relative systolic duration (1 parameter), and three regional tissue properties per myocardial segment being contractility, compliance, and activation delay (i.e. 15 model parameters in total).

Objective function

The objective function describes the agreement between modelled and measured strain. Measured strain is by definition relative to the stretch on $t = t_0$, which is defined as the onset of the QRS complex, obtained from ECG. This cannot be modelled in CircAdapt. Therefore, modelled segmental strain is shifted in time to best match strain around $t = t_0$. Modelled strain is obtained from the modelled sarcomere length l_s , using

$$\epsilon_{model,seg} = \left(\frac{l_{s,seg}}{l_{s,seg}|_{t=t_0}} - 1 \right) \cdot 100\% \quad 4.1$$

Using the objective function, goodness of the simulation is quantified relative to the measurements. It is unknown which strain indices identify the strain. Therefore, the used objective function is based on the full strain curve. To reduce the effect of drift, and reduce

the effect of the atria on the estimate, only strain is used from start of QRS complex up to 50% of relaxation. The modelled onset of shortening is matched with the measured onset of shortening. The quadratic difference of each segment is defined as

$$A_{seg}^2 = \frac{\int_{t_{onsetQRS}}^{t_{50relax}} (\epsilon_{model,seg} - \epsilon_{meas,seg})^2 dt}{t_{50relax} - t_{onsetQRS}} \quad 4.2$$

The used segments are the apical, mid, and basal segment of the RVfw, and the LVfw and IVS strain.

To prevent the parameter estimation protocol from exploring non-physiological area in the input space, a maximum mean left atrial pressure is added as a penalty function. There are signs of increased atrial volumes in this cohort [18], but no invasive pressure measurements are available. Therefore, we cannot rule out increased diastolic pressures. No pulmonary hypertension was observed in this cohort, so it can be assumed that the mean left atrial pressure (mLAP) not exceeds 15 mmHg [19]. To constrain our simulation results to physiological values without having too much effect on the estimation protocol, we use a threshold mLAP of $p_{thres} = 25 \text{ mmHg}$. This is implemented as a penalty function

$$e_{pressure} = \begin{cases} \bar{p}_{la} - p_{thres} & \text{if } \bar{p}_{la} > p_{thres} \\ 0 & \text{else} \end{cases} \quad 4.3$$

The final objective function results in

$$e^2 = \frac{1}{3} \cdot \left(1/3 \frac{A_{RVapex}^2}{\alpha^2} + 1/3 \frac{A_{RVmid}^2}{\alpha^2} + 1/3 \frac{A_{RVbase}^2}{\alpha^2} + \frac{A_{IVS}^2}{\alpha^2} + \frac{A_{LVfw}^2}{\alpha^2} \right) + \frac{e_{pressure}^2}{\beta^2} \quad 4.4$$

With $\alpha = 1\%$ and $\beta = 1 \text{ mmHg}$

Parameter Estimation protocol

Parameters were individually estimated using a parameter estimation framework previously described in more detail [8]. This framework estimates model parameters using the clinical data as described above and results in a virtual subject that reproduces the clinical data. In brief, the parameter estimation framework consisted of two steps. First, with CO and HR set to the measured values, 5000 quasi-random Monte Carlo simulations were performed from which the best 60 simulations were used as initial candidate solutions. Second, these candidate simulations were optimized using the stochastic multi-swarm particle swarm optimization (MSPSO, [20,21]). MSPSO is an evolutionary algorithm, where a population of candidate solutions moves through the input space driven by their

history and the history of a changing subpopulation. Eventually, this parameter estimation protocol results in a virtual patient, from which regional tissue properties can be extracted.

Local tissue properties

RVfw contractility, compliance, and activation delay were extracted from the resulting virtual patient simulations and the heterogeneity of these tissue properties was investigated. Due to the nonlinearity, non-monotonicity, and non-additivity of the lumped system, the individual estimated parameters were not interpreted directly, but local tissue properties were derived from the simulated time signals of myofibre stress and strain. As the RVfw is typically most affected in desmosomal mutation carriers [1], we focus on the heterogeneity in regional RVfw tissue properties. To limit the degrees of freedom in the model, parameters in the LV and IVS were not estimated on a segmented level, but in a single segment representing the entire wall to include ventricular interaction.

Regional myocardial contractility, compliance, and activation delay were used to quantify regional mechanical tissue properties. In brief, segmental contractility was defined as the maximum rate of active stress rise $\frac{d\sigma_{act}}{dt}$, which can be seen as the equivalent of the maximum rate of ventricular systolic pressure rise (dP/dt_{max}) on a local tissue level. Segmental wall compliance was defined as the inverse slope of the end diastolic passive myofibre stress (σ_{pas}) and strain (ϵ) relationship, obtained using a preload manipulation. This is the regional equivalent of the slope of the global end diastolic pressure-volume relation. Furthermore, regional activation delay was defined as the time delay of onset active stress development relative to the first activated segment. Their equations are given by

$$Contractility = \max \frac{d\sigma_{act}}{dt} \quad 4.5$$

$$Compliance = \frac{d\epsilon}{d\sigma_{pas}} \quad 4.6$$

$$t_{con} = t \Big|_{\max \frac{d\sigma_{act}}{dt}} \quad 4.7$$

$$Activation Delay = t_{con} - \frac{\sigma_{act} \Big|_{t_{con}}}{Contractility} - t_{RA activation} \quad 4.8$$

Reproducibility

To determine reproducibility, a separate validation set was used. Two separate observers blinded to clinical data performed deformation analysis twice in nine subjects with a pathogenic desmosomal mutation, resulting in four different deformation datasets per patient. Each dataset was used three times as input for the estimation framework

described above. Inter- and intra-observer agreement, as well as the uniqueness of parameter estimation were determined using the intraclass correlation coefficient (ICC) [22]. To calculate this coefficient, the average estimation of patient i was considered the true estimation (α_i) and errors originate from inter-observer variability $\epsilon_{o,i}$, intra-observer variability $\epsilon_{m,i}$, and inter-simulation variability $\epsilon_{e,i}$.

$$Y_{o,m,e,i} = \alpha_i + \epsilon_{o,i} + \epsilon_{m,i} + \epsilon_{e,i} \quad 4.9$$

The interclass correlation coefficient for each of the error origins is

$$ICC_{type} = \frac{\sigma_{\alpha}^2}{\sigma_{\alpha}^2 + \sigma_{\epsilon_{type}}^2} \quad 4.10$$

Statistical analysis and Computational Setup

Continuous data were presented as mean \pm SD. Normal distribution was tested using the Shapiro-Wilk test. Comparison between subgroups of continuous variables was done using a one-way analysis of variance, t-test, Kruskal-Wallis, or Mann-Whitney U test as appropriate. Bonferroni correction was used to adjust for multiple comparisons. All statistical analyses were performed in Python 3.6.4 using the packages *SciPy* (modified BSD License) and *statsmodels* (modified BSD License).

The CircAdapt model was coded in C++ and compiled using MSVC 14.1. All other code was written in Python and interpreted with Python 3.6.4. The parameter estimation protocol was written for single thread computation. The estimation of subjects ran parallel on Windows 10 system (AMD Ryzen Threadripper 3970X 32-Cores 4.5GHz and 128GB RAM).

Results

From the 87 AC mutation carriers who were evaluated, 3 subjects were excluded due to inadequate echocardiographic imaging quality and 16 were excluded due to missing CMR data. All remaining exams were obtained during sinus rhythm. The 68 AC mutation carriers included in this study (18 probands and 50 family members) had a mean age of 39 ± 17 years and 41 (60%) were female. Among the different pathogenic mutations, PKP2 was most common in this cohort (90%). A total of 20 control subjects (9 [45%] females, mean age 28 ± 6 years) were also included in the study. Using the 2010 TFC, 18 (26%) mutation carriers were classified in the subclinical stage, 15 (22%) in the electrical stage, and 35 (51%) in the structural stage. The median time between echocardiography and CMR was 26 days (interquartile range [-7, 398 days]). (Table 4.1)

Typical examples of measured and simulated ventricular deformation curves in a control subject and subjects in the subclinical, electrical, and structural AC disease stages are shown in Figure 4.2. Most healthy controls ($n=20$, 100%) and subclinical stage subjects

(n=12, 67%) had a Type-I deformation pattern and thus showed relatively homogeneous deformation patterns in the three RVfw segments. However, 6 (33%) subclinical subjects had an abnormal Type-II deformation pattern in the RVfw basal segment. Most subjects in the electrical stage showed heterogeneous deformation patterns with predominantly basal abnormalities (Type-II: n=8 [53%] and Type-III: n=3 [20%]), which were even more severe in the structural stage subjects (Type-II: n=10 [29%] and Type-III: n=23 [66%]).

Contractility

Overall, heterogeneity in regional RVfw contractility was higher in the electrical and structural stage groups compared to the subclinical stage and control groups (control: $9.98 \pm 4.27\%$; subclinical: $7.57 \pm 4.47\%$; electrical: $17.23 \pm 15.92\%$; structural: $16.94 \pm 13.28\%$, $p=0.011$). In general, the basal contractility was lower compared to the apical contractility (Figure 4.3). A few individuals (n=9, 13%), however, were found to have lower apical than basal contractility. No significant difference was found in average RVfw contractility (control: 363 ± 175 kPa/s ; subclinical: 373 ± 131 kPa/s; electrical: 421 ± 167 kPa/s; structural: 442 ± 174 kPa/s) ($p=0.470$).

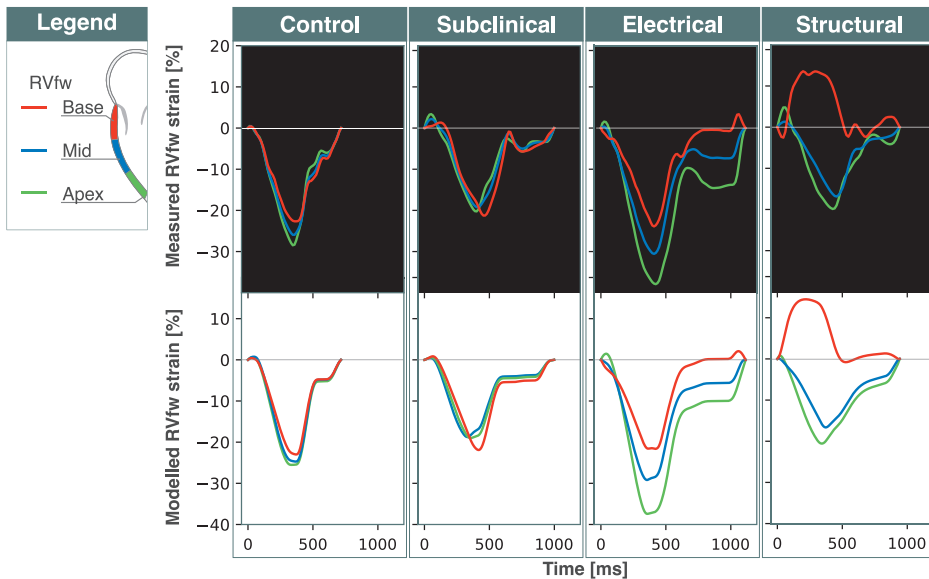


Figure 4.2: Typical regional right ventricular free wall (RVfw) strain patterns. Control subjects and most subjects in subclinical stage showed homogeneous strain patterns. Most subjects in the electrical and structural stage showed abnormal heterogeneous strain patterns.

Table 4.1: Clinical Characteristics.

	Controls (n = 20)	Subclinical Stage (n = 18)	Electrical Stage (n = 15)	Structural Stage (n = 35)	
Age, yrs	28±6	27±14	40±17 [§]	44±16 ^{^^}	p<0.001
Female	9 (45%)	11 (61%)	12 (80%)	18 (51%)	
BSA, m ²	1.87±0.17	1.80±0.21	1.84±0.17	1.91±0.22	p=0.280
Probands	0 (0%)	0 (0%)	0 (0%)	18 (53%)	
AC diagnosis	0 (0%)	0 (0%)	5 (33%)	35 (100%)	
2010 TFC					
Structural		0 (0%)	0 (0%)	35 (100%)	
Depolarization		1 (6%)	12 (80%)	17 (49%)	
Repolarization		1 (6%)	3 (20%)	20 (57%)	
Arrhythmia		0 (0%)	5 (33%)	32 (91%)	
Mutations					
PKP2 mutation		15 (83%)	14 (93%)	32 (91%)	
DSG2 mutation		3 (17%)	1 (7%)	2 (6%)	
DSP mutation		0 (0%)	0 (0%)	1 (3%)	
CMR					
CO, L/min/m ²	3.7±0.6	3.3±0.5	3.5±0.6	3.2±0.8	p=0.041
RV-EDVi, mL/m ²	108±17	87±17	94±12	132±41 [*]	p<0.01
LV-EDVi, mL/m ²	98±14	85±13	93±14	91.8±15	p=0.063
RVEF, %	54±6	56±8	51±6	36±11 [*]	p<0.001
LVEF, %	61±7	58±4	57±7	56±9	p=0.182
LGE presence	0 (0%)	0 (0%)	0 (0%)	20 (57%)	
Echocardiography					
HR	62±10	67±16	63±11	58±9	p=0.088
LV-GLS, %	-21.1±1.7	-20.0±1.7	-19.0±3.0	-17.8±3.3 [*]	p<0.001
LVEF, %	60.6±6.9	58.4±4.3	56.6±6.8	55.8±9.2	p=0.159
RV-GLS, %	-27.6±4.0	-25.4±3.6	-21.7±4.7 [§]	-15.0±5.6 [*]	p<0.001
RV basal pattern					
Type-I	20 (100%)	12 (67%)	4 (27%)	2 (6%)	
Type-II	0 (0%)	6 (33%)	8 (53%)	10 (29%)	
Type-III	0 (0%)	0 (0%)	3 (20%)	23 (66%)	
RVMD, ms	-	16.4±7.5 [^]	32.2±16.1	50±27	p<0.01

AC: Arrhythmogenic Cardiomyopathy; TFC: Task Force Criteria (both minor and major criteria included); PKP2: plakophilin-2; DSG2: desmoglobin-2; DSP: desmoplakin; CMR: cardiovascular magnetic resonance imaging; CO: cardiac output; RV: right ventricle; LV: left ventricle; EDVi: end diastolic volume indexed for BSA; RVEF: right ventricular ejection fraction; LVEF: left ventricular ejection fraction; LGE: late gadolinium enhancement; HR: Heart rate; GLS: global longitudinal strain; RVMD: right ventricular mechanical dispersion; *: p<0.05 structural stage versus all other groups (Bonferroni correction) ; ^: p<0.05 structural stage versus control group and subclinical stage; §: p<0.05 electrical stage versus control

Compliance

Heterogeneity in regional RVfw compliance was increased in the electrical and structural stage groups compared to the subclinical stage and control groups (control: $9.16 \pm 4.84\%$; subclinical: $10.46 \pm 7.11\%$; electrical: $12.49 \pm 9.63\%$; structural: $18.45 \pm 11.00\%$, $p=0.002$). On average, compliance was lower in the basal segment compared to the apical segment (Figure 4.3). Average RVfw compliance was not significantly different between the groups (control: 500 ± 325 %/kPa; subclinical: 551 ± 561 %/kPa ;electrical: 1002 ± 723 %/kPa; structural: 742 ± 595 %/kPa, $p=0.094$).

Activation delay

No significant difference was found in heterogeneity of regional RVfw activation delay (control: 10 ± 11 ms; subclinical: 8.9 ± 10.1 ms; electrical: 21 ± 30 ms; structural: 18 ± 22 ms, $p=0.267$). However, the electrical and structural stage groups contained more individuals with a relatively late activated basal segment than the subclinical stage and control groups.

Basal deformation patterns

The simulations revealed that heterogeneity in RVfw contractility was increased in compared to the Type-I and control groups (control: $9.98 \pm 4.27\%$; Type-I: $6.52 \pm 5.20\%$; Type-II: $12.19 \pm 11.25\%$; Type-III: $21.81 \pm 14.09\%$, $p < 0.001$). Also, the heterogeneity in compliance was increased in the groups with Type-II and Type-III RV basal deformation patterns compared to the Type-I and control groups (control: $9.16 \pm 4.84\%$; Type-I: $9.43 \pm 5.78\%$; Type-II: $13.00 \pm 8.46\%$; Type-III: $20.63 \pm 11.74\%$, $p < 0.001$). No significant difference was found in activation delay (control: 10.0 ± 11.1 ms; Type-I: 8.4 ± 6.3 ms; Type-II: 16.6 ± 25.5 ms; Type-III: 21.3 ± 24.7 ms, $p=0.472$).

Right ventricular mechanical dispersion

Increased RVMD in pathogenic desmosomal mutation carriers was only related to increased heterogeneity in contractility ($20.0 \pm 14.7\%$) compared to the group with normal RVMD ($7.70 \pm 4.99\%$) ($p < 0.001$). Regional heterogeneities of both compliance and activation delay were not significantly different between subjects with low and high RVMD (compliance: $16.0 \pm 10.5\%$ vs $13.8 \pm 10.2\%$, $p=0.054$; activation delay: 20.6 ± 26.0 ms vs 11.1 ± 15.6 ms, $p=0.195$).

Parameter estimation

The estimated RV tissue properties were highly reproducible, with a minimum inter- and intra-observer ICC of 0.91 and 0.86, respectively. Reproducibility of the simulations was sufficient, with a minimum ICC of 0.76. In all simulations of the same subject, the trend in local RVfw heterogeneity was similar. Supplemental Table S4.2 shows the ICC of the

estimated model parameters and Supplemental Table S4.3 shows the ICC of the individual estimated tissue properties.

The simulations ran on average in 25 ± 10 hours per patient. The duration of the simulations depended on the heart rate, the quality of the initial subset, and the number of beats needed to find a haemodynamic stable simulation for each random state. The average dimensional error between modelled and measured strain was 0.84 ± 0.35 .

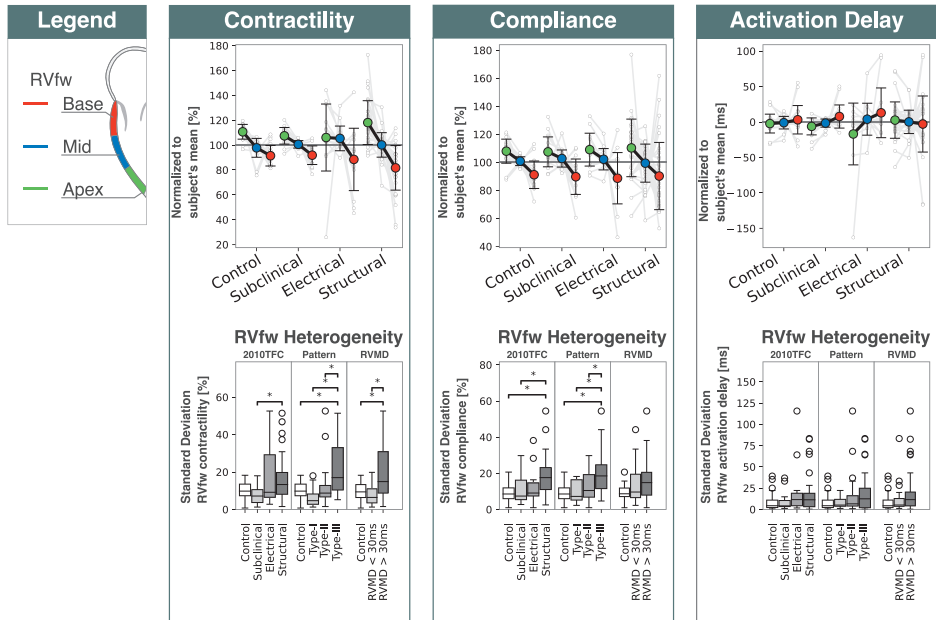


Figure 4.3: Estimated Tissue Properties. In the top row, RV regional estimations of contractility, compliance, and activation delay are shown relative to the mean value. In the bottom row, the standard deviation of these three properties is shown in a boxplot, characterized by 2010 TFC (subclinical, electrical, structural), strain morphology (Type-I, Type-II, and Type-III), and RV mechanical dispersion (RVMD). * indicates a significant difference with $p < 0.05$

Discussion

In this study, patient-specific simulations were successfully used to estimate regional RVfw tissue properties from echocardiographic deformation imaging data in 68 subjects with a pathogenic AC mutation and 20 control subjects. Regional heterogeneities of contractility and compliance in the RV free wall were largest in subjects in the structural disease stage. Our patient-specific simulations suggested that structural abnormalities according to the 2010 TFC were associated with an increased heterogeneity in RVfw myocardial tissue contractility and compliance. The most advanced disease substrates

were found predominantly in the RVfw basal segment. To our knowledge, this is the first time that regional ventricular tissue properties are quantified using patient-specific simulations based on non-invasively measured longitudinal strain patterns. This method reveals potentially important information about myocardial disease substrates and thereby paves the way for personalized medicine.

In a previous study, we showed that desmosomal mutation carriers with more advanced AC disease stages have the most abnormal RV basal deformation pattern [4]. In the same study, using computer simulations it was concluded that this abnormal mechanical behaviour of the RV cannot be explained by an electromechanical activation delay alone. Non-personalized simulations representing subgroups of AC mutation carriers showed that at least some degree of local mechanical dysfunction was needed to reproduce the measured RV deformation abnormalities. A recently published sensitivity analysis [8] confirmed that model parameters related to both activation delay and mechanical dysfunction are essential to reproduce myocardial deformation using the CircAdapt model [8]. The current study extends this previous work by estimating patient-specific myocardial substrates in all three RVfw segments and by including the LV mechanics for a more realistic approach of the patient's haemodynamics. These patient-specific simulations confirmed hypothesis that abnormal deformation patterns are related to increased regional heterogeneity in contractility and compliance without a heterogeneity in activation delay [4].

AC mutation carriers classified with structural abnormalities according to the 2010 TFC, being wall motion abnormalities such as akinesia, dyskinesia, or aneurysm in combination with RV dilatation or impaired RV systolic function measured by either CMR or echocardiography [5]. These structural abnormalities result from fibrofatty replacements of the RV myocardium, which affects regional wall motion and eventually global RV systolic function [2]. Also our computer simulations revealed the largest heterogeneity of RVfw tissue properties in the patients with structural stage disease, with the basal region of the RVfw being most affected by the disease. The few structural stage subjects with a relatively low heterogeneity of RV tissue properties showed highly impaired RV deformation with decreased contractility and compliance in all three segments, suggesting highly advanced AC disease.

Our patient-specific simulations suggested that the RV apex-to-base heterogeneity of mechanical behaviour in the more advanced AC disease stages is mostly due to decreased basal contractility and compliance. Several potential causes for AC-related changes in active and passive myocardial tissue properties have been identified in clinical and pre-clinical studies. One is the fibrofatty replacement of the myocardium[2], which results in loss of contractile function and a change in passive tissue behaviour. Besides,

Cerrone et al. found altered calcium transients in mice with a loss of PKP2 expression, including an increased calcium transient with an increased time-to-peak and a slower decay [23], suggesting a change in contractile function. To identify the exact (sub)cellular mechanisms underlying the regional RV deformation abnormalities in AC subjects beyond changes of tissue contractility and compliance, a more complex model of the myocardial electromechanics is needed.

In previous clinical studies, RVMD was associated with arrhythmic outcome [7]. In our modelling study, a higher RVMD was associated with an increased heterogeneity of contractility in the RVfw, but not with myocardial compliance. These contractile abnormalities could reflect calcium handling abnormalities, which form a possible pro-arrhythmic substrate. Interestingly, using the classification defined by Mast et al. [4], an abnormal Type-III deformation pattern was reproduced by both abnormal contractility and abnormal compliance. Where RVMD is based only on timing of the longitudinal strain, the pattern classification is based on information of both timing and amplitude. Our computer simulations suggest that both classifications can detect a different kind of tissue substrate.

An RVfw apex-to-base heterogeneity was already present in the deformation measurements of healthy controls, resulting in heterogeneity in estimated tissue properties. Some level of 'physiological' heterogeneity in deformation is to be expected, since regional differences of ventricular tissue properties, such as activation delay [24], action potential morphology [25], and wall thickness [26], also exist in healthy hearts. Because the control group and subclinical group have a similar heterogeneity in tissue properties, it can be assumed that the observed heterogeneity in regional RV tissue properties is not abnormal.

Study Limitations

Estimations are based on the average CO obtained from CMR and on regional LV and RV strain obtained from speckle tracking echocardiography. CMR volumes were used because they provided the most reliable non-invasive estimation of CO and ventricular volumes. Because the CMR and the echocardiographic examination cannot be performed simultaneously, there is a potential mismatch between the two measurements. This mismatch might result in global under- or overestimation of ventricular tissue properties but is not expected to have a significant effect on the heterogeneity in RVfw tissue properties.

The deformation measurements were obtained from four different heartbeats. We did not correct for any measurement errors, such as timing errors between the four echo views, beat-to-beat variability, or respiration. Future studies could investigate how to design an objective function using strain indices or other measurements, such as valve

timings, blood flow velocity or ejection fraction, to develop a more efficient fitting algorithm with an objective function invariant of measurement uncertainties.

Future Work

A longitudinal study, in which follow-up data is included, should be performed to reveal whether and how this disease substrate progresses in individuals, and whether any kind of disease evolution could be used for prediction of arrhythmic outcome in a clinical setting.

The majority of this retrospective study cohort consisted of PKP2 mutation carriers. Future prospective verification studies are needed to confirm our findings and to determine whether our results can be extrapolated to AC patients with a different genetic background. The CircAdapt model is not limited to modelling AC disease substrates, so future work could also explore to which extent this framework is applicable to identify disease substrates in other cardiac pathologies.

Conclusion

We presented a patient-specific modelling approach and showed its ability to reproduce regional ventricular deformation patterns and to estimate the underlying tissue properties in AC mutation carriers. Patient-specific simulations revealed that regional RV deformation abnormalities were related to reduced contractile function and tissue compliance. In most subjects, a characteristic apex-to-base heterogeneity of tissue abnormalities was present, whereby the basal region of the RVfw was most affected. Tissue abnormalities were most pronounced in the subjects with a clinically more advanced disease stage. Future studies should investigate whether simulation-based characterization of patient-specific disease substrates can be used for personalised prediction of AC disease progression or arrhythmic events.

References

1. Thiene G, Nava A, Corrado D, Rossi L, Pennelli N. 1988 Right Ventricular Cardiomyopathy and Sudden Death in Young People. *N. Engl. J. Med.* **318**, 129–133. (doi:10.1056/NEJM198801213180301)
2. Basso C, Corrado D, Marcus FI, Nava A, Thiene G. 2009 Arrhythmogenic right ventricular cardiomyopathy. *Lancet* **373**, 1289–1300. (doi:10.1016/S0140-6736(09)60256-7)
3. Groeneweg JA *et al.* 2015 Clinical Presentation, Long-Term Follow-Up, and Outcomes of 1001 Arrhythmogenic Right Ventricular Dysplasia/Cardiomyopathy Patients and Family Members. *Circ. Cardiovasc. Genet.* **8**, 437–446. (doi:10.1161/CIRCGENETICS.114.001003)
4. Mast TP *et al.* 2016 Right Ventricular Imaging and Computer Simulation for Electromechanical Substrate Characterization in Arrhythmogenic Right Ventricular Cardiomyopathy. *J. Am. Coll. Cardiol.* **68**, 2185–2197. (doi:10.1016/j.jacc.2016.08.061)
5. Marcus FI *et al.* 2010 Diagnosis of Arrhythmogenic Right Ventricular Cardiomyopathy/Dysplasia: Proposed Modification of the Task Force Criteria. *Eur. Heart J.* **31**, 806–814. (doi:10.1093/eurheartj/ehq025)
6. Mast TP *et al.* 2019 The Prognostic Value of Right Ventricular Deformation Imaging in Early Arrhythmogenic Right Ventricular Cardiomyopathy. *JACC Cardiovasc. Imaging*, 14 March. **12**, 446–455. (doi:10.1016/j.jcmg.2018.01.012)
7. Sarvari SI, Haugaa KH, Anfinsen OG, Leren TP, Smiseth OA, Kongsgaard E, Amlie JP, Edvardsen T. 2011 Right ventricular mechanical dispersion is related to malignant arrhythmias: A study of patients with arrhythmogenic right ventricular cardiomyopathy and subclinical right ventricular dysfunction. *Eur. Heart J.* **32**, 1089–1096. (doi:10.1093/eurheartj/ehr069)
8. van Osta N *et al.* 2020 Parameter subset reduction for patient-specific modelling of arrhythmogenic cardiomyopathy-related mutation carriers in the CircAdapt model. *Philos. Trans. A. Math. Phys. Eng. Sci.* **378**, 20190347. (doi:10.1098/rsta.2019.0347)
9. Teske AJ, De Boeck BW, Melman PG, Sieswerda GT, Doevendans PA, Cramer MJ. 2007 Echocardiographic Quantification of Myocardial Function using Tissue Deformation Imaging, a Guide to Image Acquisition and Analysis using Tissue Doppler and Speckle Tracking. *Cardiovasc. Ultrasound.* **5**, 27. (doi:10.1186/1476-7120-5-27)
10. Te Riele ASJM *et al.* 2013 Mutation-positive arrhythmogenic right ventricular dysplasia/ cardiomyopathy: The triangle of dysplasia displaced. *J. Cardiovasc. Electrophysiol.* **24**, 1311–1320. (doi:10.1111/jce.12222)
11. Voigt JU *et al.* 2015 Definitions for a common standard for 2D speckle tracking echocardiography: consensus document of the EACVI/ASE/Industry Task Force to standardize deformation imaging. *Eur. Heart J. Cardiovasc. Imaging* **16**, 1–11. (doi:10.1093/ehjci/jeu184)
12. Dalal D *et al.* 2009 Morphologic Variants of Familial Arrhythmogenic Right Ventricular Dysplasia/ Cardiomyopathy: A Genetics–Magnetic Resonance Imaging Correlation Study. *J. Am. Coll. Cardiol.* **53**, 1289–1299. (doi:10.1016/J.JACC.2008.12.045)
13. Te Riele ASJM *et al.* 2014 Yield of serial evaluation in at-risk family members of patients with ARVD/C. *J. Am. Coll. Cardiol.* **64**, 293–301. (doi:10.1016/j.jacc.2014.04.044)
14. Haugaa KH *et al.* 2017 Comprehensive multi-modality imaging approach in arrhythmogenic cardiomyopathy—an expert consensus document of the European Association of Cardiovascular Imaging. *Eur. Heart J. Cardiovasc. Imaging* **18**, 237–253. (doi:10.1093/ehjci/jew229)
15. Arts T, Delhaas T, Bovendeerd P, Verbeek X, Prinzen F. 2005 Adaptation to Mechanical Load Determines Shape and Properties of Heart and Circulation: the CircAdapt Model. *Am. J. Physiol. Heart Circ. Physiol.* **288**, 1943–1954. (doi:10.1152/ajpheart.00444.2004.)
16. Walmsley J, Arts T, Derval N, Bordachar P, Cochet H, Ploux S, Prinzen FW, Delhaas T, Lumens J. 2015 Fast Simulation of Mechanical Heterogeneity in the Electrically Asynchronous Heart Using the MultiPatch Module. *PLoS Comput. Biol.* **11**, 1–23. (doi:10.1371/journal.pcbi.1004284)
17. Lumens J, Delhaas T, Kirn B, Arts T. 2009 Three-wall segment (TriSeg) model describing mechanics and hemodynamics of ventricular interaction. *Ann. Biomed. Eng.* **37**, 2234–2255. (doi:10.1007/s10439-009-9774-2)
18. Zghaib T *et al.* 2018 Atrial Dysfunction in Arrhythmogenic Right Ventricular Cardiomyopathy. *Circ. Cardiovasc. Imaging* **11**, e007344. (doi:10.1161/CIRCIMAGING.117.007344)
19. Galìè N *et al.* 2016 2015 ESC/ERS Guidelines for the diagnosis and treatment of pulmonary hypertension. *Eur. Heart J.* **37**, 67–119. (doi:10.1093/eurheartj/ehv317)
20. Kennedy J, Eberhart R. In press. Particle swarm optimization. In *Proceedings of ICNN'95 - International Conference on Neural Networks*, pp. 1942–1948. IEEE. (doi:10.1109/ICNN.1995.488968)

21. Liang JJ, Suganthan PN. 2005 Dynamic multi-swarm particle swarm optimizer. *Proc. - 2005 IEEE Swarm Intell. Symp. SIS 2005* **2005**, 127–132. (doi:10.1109/SIS.2005.1501611)
22. Koo TK, Li MY. 2016 A Guideline of Selecting and Reporting Intraclass Correlation Coefficients for Reliability Research. *J. Chiropr. Med.* **15**, 155–163. (doi:10.1016/j.jcm.2016.02.012)
23. Cerrone M *et al.* 2017 Plakophilin-2 is required for transcription of genes that control calcium cycling and cardiac rhythm. *Nat. Commun.* **8**, 106. (doi:10.1038/s41467-017-00127-0)
24. Durrer D, van Dam RT, Freud GE, Janse MJ, Meijler FL, Arzbaecher RC. 1970 Total Excitation of the Isolated Human Heart. *Circulation* **41**, 899–912. (doi:10.1161/01.CIR.41.6.899)
25. Antzelevitch C, Fish J. 2001 Electrical heterogeneity within the ventricular wall. *Basic Res. Cardiol.* **96**, 517–527. (doi:10.1007/s003950170002)
26. Kawel-Boehm N *et al.* 2015 Normal values for cardiovascular magnetic resonance in adults and children. *J. Cardiovasc. Magn. Reson.* **17**, 1–33. (doi:10.1186/s12968-015-0111-7)

Supplemental Material

Supplemental Table 4.1: Parameter description

Model Parameter	Description	Location	REF	MC	PSO
SfAct Lv [kPa]		LV	120	[90,150]	[0,300]
SfAct Sv [kPa]		IVS	120	[90,150]	[0,300]
SfAct RvApex [kPa]	Linear scaling factor for active stress	RVfw apex	120	[30,150]	[0,300]
SfAct RvMid [kPa]		RVfw mid	120	[30,150]	[0,300]
SfAct RvBase [kPa]		RVfw base	120	[30,150]	[0,300]
k1 Lv [-]		LV	10	[5,15]	[1,100]
k1 Sv [-]		IVS	10	[5,15]	[1,100]
k1 RvApex [-]	Non-linear scaling factor for passive stress	RVfw apex	10	[5,20]	[1,100]
k1 RvMid [-]		RVfw mid	10	[5,20]	[1,100]
k1 RvBase [-]		RVfw base	10	[5,20]	[1,100]
dT Lv [ms]		LV	0	[-25,25]	[-150,150]
dT Sv [ms]		IVS	0	[-25,25]	[-150,150]
dT RvApex [ms]	Activation delay of segment relative to estimated AV-delay	RVfw apex	0	[-25,50]	[-150,150]
dT RvMid [ms]		RVfw mid	0	[-25,50]	[-150,150]
dT RvBase [ms]		RVfw base	0	[-25,50]	[-150,150]
AmRef Lv [cm2]	Segment area at sarcomere length $L_s = 2\mu m$	LVfw	98	[0.8,1.2]*98	[0.5,2]*98
AmRef Sv [cm2]		IVS	49	[0.8,1.2]*49	[0.5,2]*49
AmRef Rv [cm2]		RVfw	129	[0.8,1.2]*129	[0.5,2]*129
TimeFac [-]	Scaling factor for myocardial twitch duration	Global	1	[0.8,1.2]	[0.1,2]

REF: reference value; MC: Monte Carlo; PSO: particle swarm optimization

Supplemental Table 4.2: ICC of estimated model parameters

Inter	SfAct	0.85	0.86	SfAct	0.93	SfAct	0.92	SfAct	0.85	K1	0.98	K1	0.94	IVS	K1	0.97	RfWw apex	K1	0.90	RfWw mid	K1	0.91	RfWw base	DT	0.88	LVTw	DT	0.97	IVS	DT	0.95	RfWw Apex	DT	0.96	RfWw Mid	DT	0.94	RfWw Base	AmRet	0.99	LVTw	AmRet	0.89	IVS	AmRet	0.95	RfWw	TimeFac	0.99
Intra	SfAct	0.71	0.68	SfAct	0.92	SfAct	0.92	SfAct	0.84	K1	0.95	K1	0.90	IVS	K1	0.83	RfWw apex	K1	0.85	RfWw mid	K1	0.89	RfWw base	DT	0.81	LVTw	DT	0.80	IVS	DT	0.89	RfWw Apex	DT	0.94	RfWw Mid	DT	0.96	RfWw Base	AmRet	0.96	LVTw	AmRet	0.82	IVS	AmRet	0.97	RfWw	TimeFac	0.91
Model	SfAct	0.47	0.58	SfAct	0.86	SfAct	0.87	SfAct	0.75	K1	0.90	K1	0.69	IVS	K1	0.80	RfWw apex	K1	0.69	RfWw mid	K1	0.73	RfWw base	DT	0.56	LVTw	DT	0.63	IVS	DT	0.74	RfWw Apex	DT	0.96	RfWw Mid	DT	0.95	RfWw Base	AmRet	0.92	LVTw	AmRet	0.76	IVS	AmRet	0.92	RfWw	TimeFac	0.93

Supplemental Table 4.3: ICC of estimated tissue properties

Inter	Contractility	0.98	0.96	Contractility	0.95	Contractility	0.97	Compliance	0.98	RfWw Base	0.96	Compliance	0.96	Activation Delay	RfWw base	0.94
Intra	Contractility	0.95	0.93	Contractility	0.95	Contractility	0.88	Compliance	0.97	RfWw Mid	0.97	Compliance	0.97	Activation Delay	RfWw Mid	0.89
Model	Contractility	0.94	0.91	Contractility	0.92	Contractility	0.76	Compliance	0.97	RfWw Apex	0.96	Compliance	0.96	Activation Delay	RfWw Apex	0.83

5



Uncertainty Quantification of Regional Cardiac Tissue Properties in Arrhythmogenic Cardiomyopathy using Adaptive Multiple Importance Sampling

Based on: **Nick van Osta**^{*}, Feddo P. Kirkels^{*}, Tim van Loon, Tijmen Koopsen, Aurore Lyon, Roel Meiburg, Wouter Huberts, Maarten J. Cramer, Tammo Delhaas, Kristina H. Haugaa, Arco J. Teske, Joost Lumens. “Uncertainty quantification of regional cardiac tissue properties in Arrhythmogenic Cardiomyopathy using adaptive multiple importance sampling” *Frontiers in Physiology* 12:738926 (2021)

^{*}NvO and FK contributed equally.

Abstract

Computational models of the cardiovascular system are widely used to simulate cardiac (dys)function. Personalization of such models for patient-specific simulation of cardiac function remains challenging. In this study, we present a methodology for patient-specific estimation and uncertainty quantification of parameters in the closed-loop CircAdapt model of the human heart and circulation using echocardiographic deformation imaging. Based on patient-specific estimated parameters we aim to reveal the mechanical substrate underlying deformation abnormalities in patients with arrhythmogenic cardiomyopathy (AC).

We used adaptive multiple importance sampling to estimate the posterior distribution of regional myocardial tissue properties. This methodology is implemented in the CircAdapt cardiovascular modelling platform and applied to estimate active and passive tissue properties underlying regional deformation patterns, left ventricular volumes, and right ventricular diameter. First, we tested the accuracy of this method and its inter- and intraobserver variability using nine datasets obtained in AC patients. Second, we tested the trueness of the estimation using nine in silico generated virtual patient datasets representative for various stages of AC. Finally, we applied this method to two longitudinal series of echocardiograms of two pathogenic mutation carriers without established myocardial disease at baseline.

Tissue characteristics of virtual patients were accurately estimated with a highest density interval containing the true parameter value of 9% (95% CI [0 – 79]). Variances of estimated posterior distributions in patient data and virtual data were comparable, supporting the reliability of the patient estimations. Estimations were highly reproducible with an overlap in posterior distributions of 89.9% (95% CI [60.1 – 95.9]). Clinically measured deformation, ejection fraction, and end diastolic volume were accurately simulated. In presence of worsening of deformation over time, estimated tissue properties also revealed functional deterioration.

This method facilitates patient-specific simulation-based estimation of regional ventricular tissue properties from non-invasive imaging data, taking into account both measurement and model uncertainties. Two proof-of-principle case studies suggested that this cardiac Digital Twin technology enables quantitative monitoring of AC disease progression in early stages of disease.

Introduction

Computational models of the cardiovascular system are widely used to simulate cardiac (dys)function and related clinical application of therapies for cardiac disease [1]. Various attempts to generate a Digital Twin of the human heart have been made [2]. Previously, we proposed a framework to create a Digital Twin [3] for quantification of the disease substrate underlying abnormal tissue deformation in patients with arrhythmogenic cardiomyopathy (AC) [4].

Inheritable AC primarily affects the right ventricle (RV) and predisposes to ventricular arrhythmias and sudden cardiac death in young individuals [5,6]. Therefore, early disease detection is important. We previously determined an *in silico* disease substrate with decreased regional RV contractility and compliance, with the potential to predict disease progression on a patient-specific level [4]. This method was, however, not able to include uncertainty present in both measurement and model.

Uncertainty will inevitably play a role in comparing estimated properties and thus Bayesian inference methods should be used to estimate the posterior distribution of model parameters, rather than only providing point estimates. Cardiovascular computational models are in general complex, meaning that the posterior distribution cannot be calculated analytically. Various techniques have been proposed to solve this problem, in which Markov chain Monte Carlo (MCMC) methods are often used [7–9]. Adaptive multiple importance sampling (AMIS) is an important alternative to MCMC since it enables estimation of the posterior distribution in a model with a relatively high number of input parameters [10,11].

In this study, we apply AMIS to quantify parameter uncertainties in Digital Twins based on echocardiographic deformation imaging. We validate the methodology based on both *in silico* generated virtual data and datasets obtained from patients with AC and mutation positive family-members at risk of developing the disease. Furthermore, we use longitudinal series of echocardiograms in two AC patients to validate clinical applicability of this methodology.

Materials and Methods

This section and Figure 5.1 elucidate the methodology used to estimate parameters and related uncertainties using the CircAdapt model. First, we elaborate the mathematical basis and implementation of AMIS, which is generally applicable. Secondly, we describe the mathematical problem and introduce the included clinical measurements and the computational model used for the likelihood function. Finally, we explain the simulation protocol. The source code as well as the virtual patient datasets are available.

Mathematical basis of adaptive multiple importance sampling

We consider an n_θ - dimensional vector as a set of parameters θ of a numerical model $z = \mathcal{M}(\theta)$. This model $\mathcal{M}: \mathcal{R}^{n_\theta} \rightarrow \mathcal{R}^{n_z}$ maps the parameter vector to an n_z -dimensional vector of modelled data z . Measurement uncertainties are included in the likelihood function $p(z|\theta)$ representing the similarity between patient observation and model output. The posterior distribution $p(\theta|z)$ is the probability of having parameters θ given the observation z and is given by Bayes' rule as

$$p(\theta|z) = \frac{p(z|\theta)p(\theta)}{p(z)} \propto p(z|\theta)p(\theta), \quad 5.1$$

with $p(\theta)$ the prior knowledge of the parameters and $p(z)$ the normalizing constant. No prior knowledge of the parameters $p(\theta)$ is known, so $p(\theta)$ was assumed to be uniform.

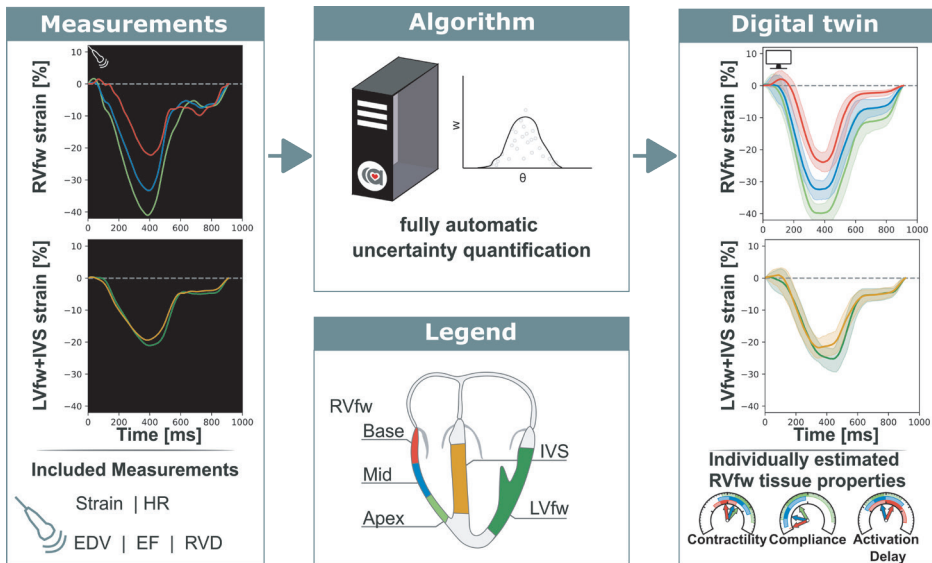


Figure 5.1: Non-invasive measurements were used as input for a fully automatic automated uncertainty quantification algorithm. This algorithm produced a Digital Twin based on estimated parameters with accompanying uncertainty. This Digital Twin can be used to get more insight in the estimated tissue properties. RVfw: right ventricle free wall; LVfw: left ventricle free wall; IVS: inter ventricular septum; HR: heart rate; EDV: end diastolic volume; EF: ejection fraction; RVD: right ventricular diameter;

Importance sampling is an algorithm which estimates the posterior distribution $p(\theta|z)$ [11]. The set of samples $\theta = \{\theta \sim q(\theta)\}$ drawn from the proposal distribution $q(\theta)$ form an empirical estimation of the posterior distribution $p(\theta|z)$ in which each sample is weighted with the sample weight w described by

$$w(\theta) \propto \frac{p(\theta|z)}{q(\theta)}. \quad 5.2$$

The weights are normalized such that $\sum_{\theta \in \Theta} w(\theta) = 1$. Importance sampling is most effective when the proposal distribution $q(\theta)$ is close to the posterior distribution $p(\theta|z)$ such that variance in weight of the samples is small and the effective sample size is close to the actual sample size. Since no information was available on the posterior distribution, we used adaptive importance sampling in which the proposal distribution is iteratively updated to better describe the posterior distribution [11].

The computational cost of calculating the likelihood $p(z|\theta)$ in cardiovascular models is relatively high compared to the cost of calculating the probability density function of the proposal distribution $q(\theta)$, so the samples from all previous iterations were included in defining the proposal distribution $q(\theta)$ to optimally recycle past simulations following the adaptive multiple importance sampling (AMIS) (see Figure 5.2) [10].

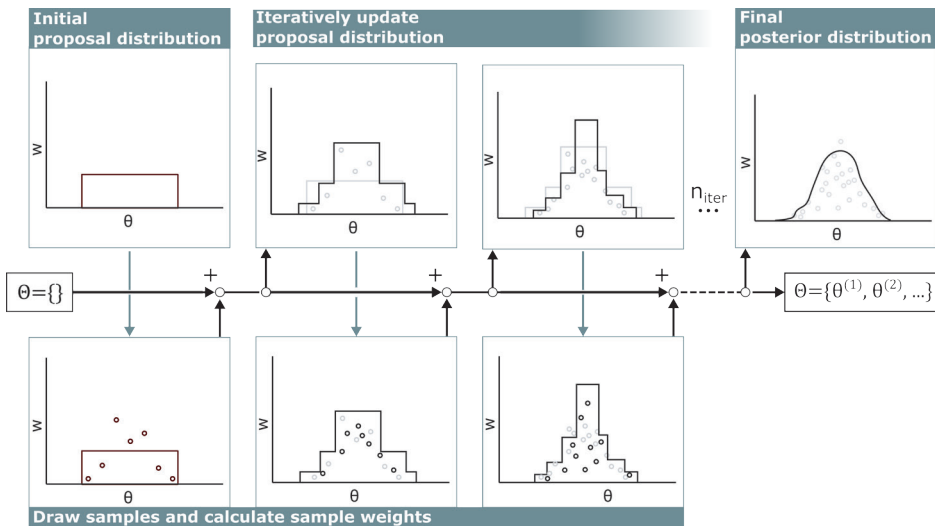


Figure 5.2: Visualization of adaptive multiple importance sampling. In the first iteration, samples θ are drawn from a uniform distribution and stored in the sample set Θ . For each sample, the corresponding sample weight w is calculated. Then, based on all previous samples θ in the sample set Θ and corresponding sample weight w , the next proposal distribution is defined and new samples are added to the sample set Θ . This iterates n_{iter} times.

Each iteration in this algorithm consists of two stages. First, samples are drawn from the proposal distribution and weights of all samples are updated. Second, the proposal distribution is updated based on the new sample weights.

Draw samples and calculate sample weights

At the start of each iteration i , 100 samples are drawn from the current proposal distribution $\pi_i(\theta)$. Samples are drawn without statistical dependencies between parameters, which may result in non-physiological combinations of parameters. For example, the model is not parameterized for a low contractile heart to be able to supply a high cardiac output (CO) and is therefore likely to become numerically unstable. To circumvent this, only a small uniform distribution around the reference is used as initial proposal distribution $q_0(\theta)$. AMIS will increase and decrease the search area of the proposal distribution and will move this to the area of interest in which physiological samples will be drawn close to the desired posterior distribution.

Each iteration, the weights are updated based on the proposal function and likelihood (Equation 5.2). The probability density function of all previous proposal distributions is given by the sum of all individual proposal distributions

$$q_i(\theta) = \frac{1}{N_{samples}} \sum_{i=0}^{n_{iter}-1} n_{samples,i} \cdot \pi_i(\theta), \quad 5.3$$

with $n_{samples,i}$ the number of samples in iteration i and $N_{samples} = \sum_{i=0}^{n_{iter}-1} n_{samples,i}$ the total number of samples. Samples drawn from poorly performing proposal distributions are eliminated through the erosion of their low weights [10].

The likelihood function is defined based on the normalized dimensionless summed squared error $X(\theta)^2$. This $X(\theta)^2$ is problem dependent and the X^2 used in this study is described in the Section ‘Problem Description’. We assumed a non-informative uniform prior and neglected all interactions between individual errors. Furthermore, annealed adaptive importance sampling [12] was used to prevent the algorithm from premature convergence [13,14], resulting in a likelihood

$$p(z|\theta, T_i) \propto e^{-\frac{X(\theta)^2}{T_i}}, \quad 5.4$$

in which $T_i \geq 1$ in each iteration i and represents the annealing temperature. This method is included to control convergence rate, thereby improving global search capabilities and limiting premature convergence towards local minima. The initial temperature is set to $T_{max} = 10$, and decreases each iteration i such that

$$T_{i+1} = \begin{cases} \min(10, T_i + \Delta X_{opt}^2) & \text{if } X^2 \text{ is improved} \\ \max(1, 0.8 \cdot T_i) & \text{else} \end{cases} \quad 5.5$$

with ΔX_{opt}^2 the difference between the old and new X^2 of the best sample.

Update proposal distribution

Each iteration, the proposal distribution is updated based on all drawn samples in the sample set Θ and its corresponding weight w . In the updated proposal distributions, samples were drawn along the principal component axes of the weighted sample set Θ . This protocol ran for at least 500 iterations. Additional iterations were performed in the case that the effective sample size $N_{eff} > 10 \cdot n_{\theta}$ was not fulfilled. The Kish effective sample size N_{eff} was used [15], which is defined as

$$N_{eff} = \frac{[\sum_{\theta \in \Theta} w(\theta)]^2}{\sum_{\theta \in \Theta} (w(\theta)^2)}. \quad 5.6$$

Problem description***Clinical data***

Patient-specific simulations were based on echocardiographic data from AC mutation carriers in various disease stages. Besides clinically measured LV and RV regional deformation imaging data, the LV end diastolic volume (EDV), LV ejection fraction (EF) and right ventricular basal diameter (RVD) were used as model input. We used echocardiographic data of nine pathogenic AC mutation carriers which were evaluated in the University Medical Center Utrecht, the Netherlands. As previously described [4], deformation analyses of these echocardiograms were performed twice by two observers to determine clinical inter- and intra-observer variability. Lastly, longitudinal datasets with >2 echocardiograms per patient at different time points were used to explore applicability of the model for follow-up of tissue properties over time. These longitudinal datasets were acquired from AC mutations carriers which were evaluated in the Oslo University Hospital, Norway.

All echocardiographic data were obtained on a Vivid 7, Vivid 9 or Vivid E95 ultrasound machine (GE Vingmed, Horten, Norway). The echocardiographic protocol was described previously [16]. In this study, we focused on the right ventricular free wall (RVfw). This is typically the most affected area in AC mutation carriers [17], which is expressed in typical deformation abnormalities (delayed onset of shortening, decreased peak systolic strain, post-systolic shortening, and increased RV mechanical dispersion) [16]. Therefore, deformation patterns of three RVfw segments (apical, mid-ventricular and basal) were used as input for our modelling framework (Figure 5.1) [4]. Additionally, LV free wall (LVfw) and interventricular septal (IVS) deformation patterns were included to ensure realistic mechanical boundary conditions for the RVfw in terms of ventricular interaction. These patterns were obtained by averaging the 12 LVfw and 6 IVS segmental deformation curves, respectively, using the standardized 18-segment model [18].

Computational model of heart and circulation

Clinical measures were simulated using the CircAdapt model. This model is a fast biomechanical lumped parameter model of the heart and circulation. Via the one fibre model [19], wall stress is related to cavity pressure. The TriSeg module allows inter-ventricular interaction over the IVS [20]. Phenomenological material laws prescribe the stress-strain relation in the spherical walls. The MultiPatch module allows for regional heterogeneity of tissue properties within a single wall [21] and is used to describe the heterogeneity in the RVfw. Three segments were created in the RVfw to model the mechanics in the three different RVfw segments (apical, mid-ventricular, and basal).

The parameter subset θ included for estimation was based on a previous sensitivity analysis [4] and is shown in Table 5.1. Parameters included were regional parameters describing the constitutive behaviour of active (SfAct) and passive stress (k1), activation delay (dT), reference wall area (AmRef), and global parameters relative systole duration (RSD), and CO. Heart rate (HR) in the model was set to match clinically measured HR to ensure equal cycle lengths in measured and modelled signals.

Strain was defined as the segmental displacement relative to its reference length at end diastole. Additionally, EF, EDV, and RVD were included. Modelled EDV was defined as the maximum cavity volume of the LV cavity assuming perfect valve behaviour. EF was defined as the ratio of stroke volume over maximum volume. RVD was defined as the maximum cavity diameter between the RVfw and IVS.

Likelihood function

As shown in Equation 5.4, the likelihood function was based on the summed squared error X^2 . This error consists of the error in strain of the 5 segments and on the error in EF, EDV, and RVD. Because the measured diastolic strain is less reliable due to the drift affecting most of this phase, we only included strain during the systolic phase in this study. This systolic phase was defined from the onset of the QRS complex until 100ms after peak strain of the segment with longest shortening phase.

To account for dependencies in strain, we included weighted dimensionless errors based on strain ($e_{\epsilon,seg}^2$), strain rate ($e_{\dot{\epsilon},seg}^2$), and inter-segmental strain differences ($e_{\Delta\epsilon_{inter}}^2$). Errors in EF (e_{EF}^2), EDV (e_{EDV}^2) and RVD (e_{RVD}^2) were assumed independent, resulting in the X^2 to be the sum of all individual weighted dimensionless errors e^2 :

$$X^2 = \sum_{seg \in segments} (e_{\epsilon,seg}^2 + e_{\dot{\epsilon},seg}^2) + \sum_{inter \in interseg} e_{\Delta\epsilon_{inter}}^2 + \sum_{m \in [EF, EDV, RVD]} e_m^2. \quad 5.7$$

Standard deviations used to normalize each individual term were manually estimated a priori to meet differences between the inter- and intraobserver datasets. Standard deviations used to normalize EF, EDV, and RVD were set a priori in consultation with clinical partners.

Table 5.1: parameters included in the optimization protocol

Model parameter	Unit	Description	Sample distribution	Parameter range	Parameter Location				
					Rv Apex	Rv Mid	Rv Base	IVS	LVfw
SfAct	kPa	Active stress scaling factor	logit-uniform	[0, 1000]	x	x	x	x	x
k1	-	Stiffness exponent	logit-uniform	[1, 100]	x	x	x	x	x
dT	ms	Activation delay	logit-uniform	[-200, 800]	x	x	x	x	x
AmRef	cm ²	Eccentric hypertrophy	log-uniform	[0, ∞]	<i>combined</i>			x	x
RSD	-	Global systolic duration scaling	log-uniform	[0, ∞]	<i>global</i>				
Q0	L/min	Cardiac Output	log-uniform	[0, ∞]	<i>global</i>				
					Total: 20				

RV tissue properties

To relate our simulations to clinical measures, four RV tissue properties were investigated, namely contractility, activation delay, compliance, and myocardial work. Segmental contractility was defined as the maximum rate of active stress rise, which can be seen as the equivalent of the maximum rate of ventricular systolic pressure rise (dp/dt_{max}) on a local tissue level. Segmental wall compliance was defined as the slope of the end diastolic myofibre stress-strain relationship at time before first ventricular activation and can be interpreted as the regional equivalent of the slope of the global end

diastolic pressure-volume relation. Myocardial work density was defined as the area within the stress-strain loop and can be interpreted as the regional equivalent of global stroke work.

Simulation protocol

Uncertainty Quantification of Real Patient datasets

Nine clinical datasets in which the echocardiographic images were analysed twice by two independent observers were included to test reproducibility, leading to 36 datasets. For each individual dataset, parameters were estimated three times resulting in 108 estimations in total. Since no ground truth exists for estimated model parameters, only the reproducibility of estimations was evaluated. Three kinds of reproducibility were investigated, namely computational reproducibility, reproducibility including interobserver

variability, and reproducibility including intraobserver variability. First, computational reproducibility was defined as the reproducibility of the exact same clinical dataset and quantified by the mutual information (MI) between two model parameter estimations. The same protocol was repeated three times with a different random seed. To calculate the MI, two distributions were discretized into 100 bins. The MI was then defined as the overlap divided by the union of the distributions. Secondly, reproducibility including interobserver variability was tested on the nine patient datasets, whereby a second blinded observer performed deformation imaging analysis on the same echocardiographic loops as the first observer. It was defined as MI between two estimated model parameter distributions from two datasets observed by the two different observers. Finally, reproducibility including intraobserver variability was quantified similarly from two different datasets, whereby the observer performed the deformation analysis again after at least two weeks, blinded to previous results. The median MI with 95% confidence interval (CI) of all parameter estimations was reported. In case the estimations from different observations fully overlap, $MI=100\%$. In case of no overlap at all, $MI=0\%$.

Uncertainty Quantification of Virtual Patient datasets

To test the trueness of the estimation, in silico generated virtual patients were generated. To ensure these virtual patients to be representable for real AC patients, nine virtual patients were created based on the nine real patient datasets. For each real patient, the simulation with maximum likelihood was selected. The output of this simulation was used as virtual patient dataset, which was used as input of the modelling framework.

Trueness of the virtual estimations was tested by comparing the estimated distribution with the known true parameter values. For each parameter, the highest density interval (HDI) for which the true value is in the interval was calculated. The HDI was defined as the area of the distribution for which the posterior holds $p(\theta|z) > p(\theta_{true}|z)$. The distribution was approximated with a histogram with bin width defined by the Freedman-Diaconis rule [22]. The HDI for each parameter should be near 0% meaning the true value is near the maximum a posteriori.

Application in longitudinal datasets

Two subjects with a baseline and two follow-up echocardiograms were selected (Table 5.2). For all six datasets, clinical data was extracted and the datasets were estimated independently of each other, similarly as described above. The two longitudinal sets of estimated tissue properties were investigated. Due to the retrospective nature of this study, LV EDV was only available at baseline. We assumed that it did not change during follow-up.

Table 5.2: Patient characteristics of the two subjects at baseline and follow-up used in the likelihood function

	Subject 1			Subject 2		
	0	4.5	9.1	0	5.2	7.3
Time after baseline [yr]	0	4.5	9.1	0	5.2	7.3
LV EDV [mL]	112	*	*	150	*	*
LV EF [%]	61	61	61	59	64	57
RVD [mm]	43	43	42	45	38	40

* LV EDV was only recorded at baseline. It was assumed not to change during follow-up

Code implementation

The CircAdapt model was written in C++. All other code was written in Python. Each individual dataset was solved sequentially and independently. The source code of the CircAdapt model has been made available before [3]. All other source code is publicly available on Zenodo (<https://doi.org/10.5281/zenodo.5084657>). Datasets were estimated in parallel with Python 3.9.4 on a AMD Ryzen Threadripper 3970X.

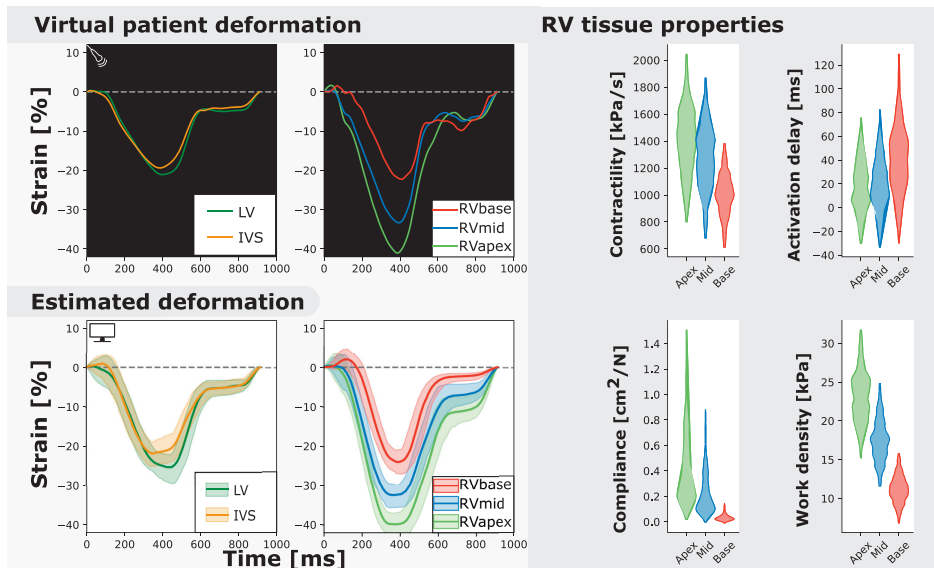


Figure 5.3: Measured and estimated strain of real subject (left) and violin plots of estimated parameters (right). Deformation patterns and regional heterogeneity was well captured by the model. The best simulation in the sample set was in good agreement with to the patients dataset ($\chi^2_{opt} = 8.9$).

Results

Uncertainty Quantification of Real Patient datasets

Regional deformation characteristics were accurately simulated close to the measured deformation and with reasonable uncertainty ($\chi^2_{opt} = 9.4$ (95% CI [5.4 – 20.9])).

Figure 5.3 (left) shows a representative example. The modelled strain followed the pattern of clinically measured strain during systole and heterogeneity between the segments was well captured. A 1D representation of the convergence of the proposal distribution, corresponding to the estimated model parameters is shown in Figure 5.4. In the first 50 iterations, the proposal distribution decreased, increased, and moved to the area of interest. From the 50th iteration, most proposal distributions stabilized. This behaviour was also observed in estimations in other datasets.

The estimated posterior distributions of the model parameters (Figure 5.1) of most parameters were estimated with small variances, except for parameters SfAct and k1, because they were unidentifiable in some segments. The posterior correlation matrix (Figure 5.5) shows the correlation between estimated posterior distributions. Notable are the correlations between model parameters SfAct, k1, dT, and AmRef describing mechanics in the same wall segment. Additionally, there was a high correlation between different segments for the model parameters dT and AmRef. From the two global parameters, only RSD seemed to correlate with dT.

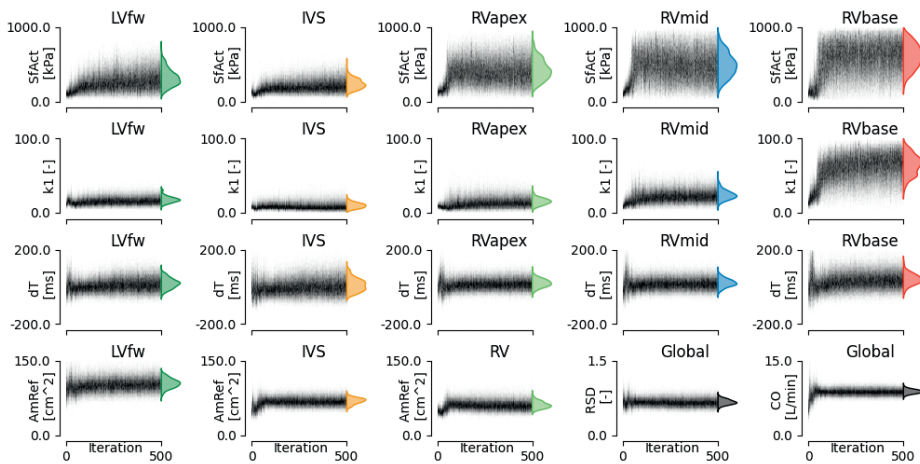


Figure 5.4: Convergence of estimated model parameters. The distributions on the right show the final estimated posterior distribution.

Figure 5.3 (right) shows the estimated regional RV model parameters and the RV tissue properties contractility, activation delay, compliance, and work density. The RV tissue properties were estimated with distributions with a smaller variance compared to the estimated model parameters. A decrease in basal contractility, compliance, and work density with respect to the apical and mid segment was found which is in line with the abnormal basal deformation pattern.

Figure 5.5 (bottom) shows the correlation between posterior model parameter distributions with the RV tissue properties contractility, compliance, and work density.

Contractility was mostly correlated with SfAct, AmRef, and CO. In the RVapex and RVmid, contractility was not only dependent on the parameters prescribing its own segmental mechanics, but also on the parameters prescribing other segmental mechanics. Similar results were observed for compliance, which was correlated with SfAct, k1, and dT. Compliance showed no correlation with AmRef, RSD, and CO. Work density was mostly correlated with CO.

Estimated model parameters were highly reproducible. Computational reproducibility was found with an MI of 89.9% (95% CI [60.1 – 95.9]). The reproducibility error given inter- and intraobserver variability were estimated with an MI of 86.5% (95% CI [46.0 – 95.2]) and 85.9% (95% CI [43.7 – 95.3]), respectively.

Uncertainty Quantification of Virtual Patient datasets

Nine virtual patients were created based on the nine real-patient estimations. As an example, Figure 5.6 shows the virtual patient based on the patient results described above. Regional deformation characteristics were simulated close to the virtual patients deformation characteristics ($X_{opt}^2 = 2.0$ (95% CI = [1.2 – 3.0])). The true parameter values were well captured by the estimated distributions. The HDI of the true parameter values was 9% (95% CI [0 – 79]). Heterogeneity in model parameters was well preserved. The width of the distribution in virtual fits was similar to that in the original patient estimation.

Application: Longitudinal datasets

Two subjects with a baseline and two follow-up echocardiograms were included in this study (Table 5.2). The first subject had a follow-up examination after 4.5 and 9.1 years and the second subject after 5.2 and 7.3 years. Results of these case studies are shown in Figure 5.7 and Figure 5.8.

Subject 1 developed an abnormal deformation pattern of the basal RV segment at last follow-up which was not seen at baseline. Computer simulations showed homogeneous RV contractility, activation delay, compliance, and work at baseline. In the last follow-up examination, an apex-to-base heterogeneity in compliance and work density was present.

Subject 2 showed normal RV deformation patterns at baseline and did not develop clear deformation abnormalities during follow-up. Contractility, activation delay, compliance, and work density were estimated homogeneously at baseline. In the final follow-up, a small apex-to-base heterogeneity in compliance was present.

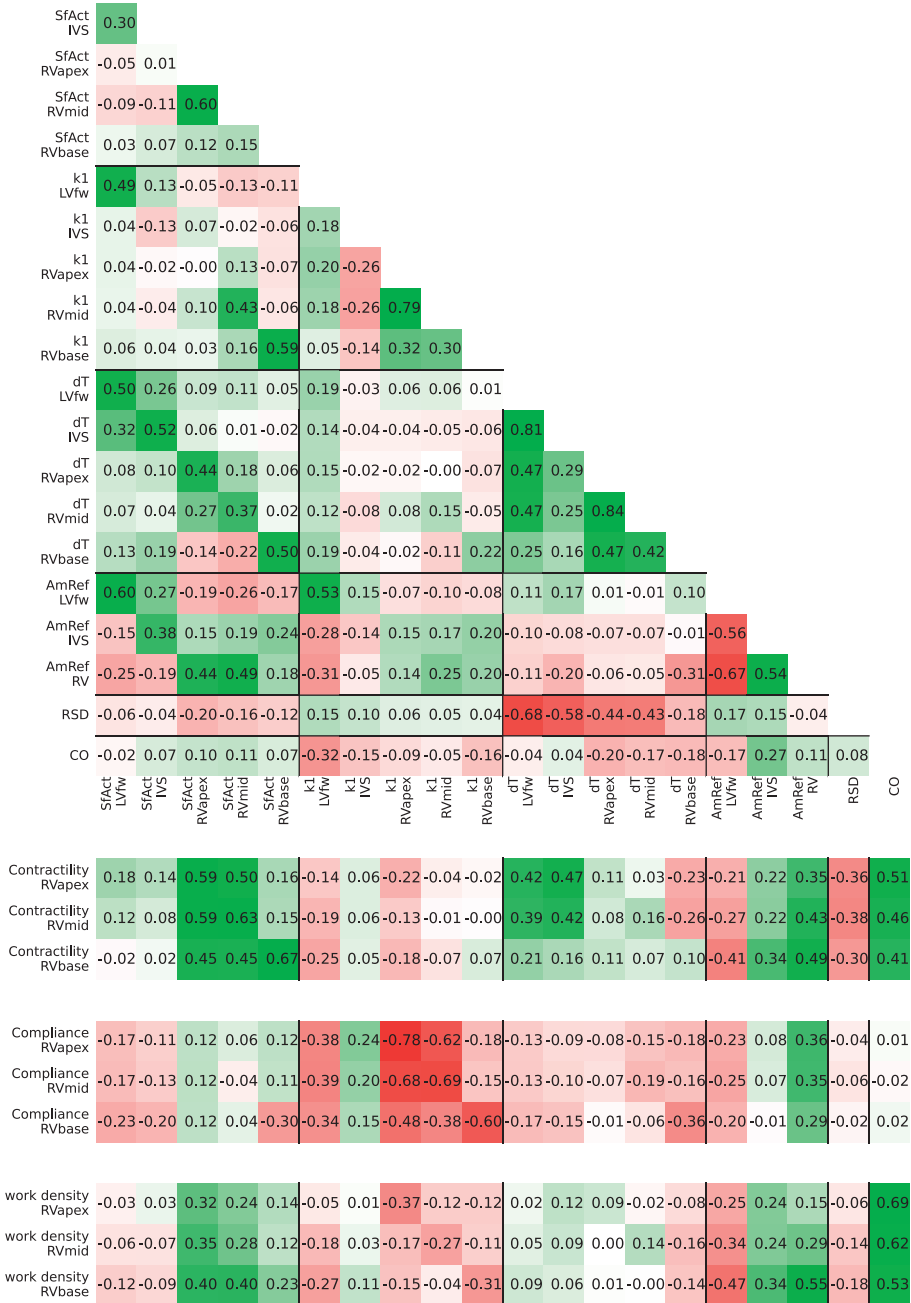


Figure 5.5: Posterior correlation matrix of the estimated model parameters (top) and the correlation between the posterior distribution of model parameters and derived tissue properties (bottom).

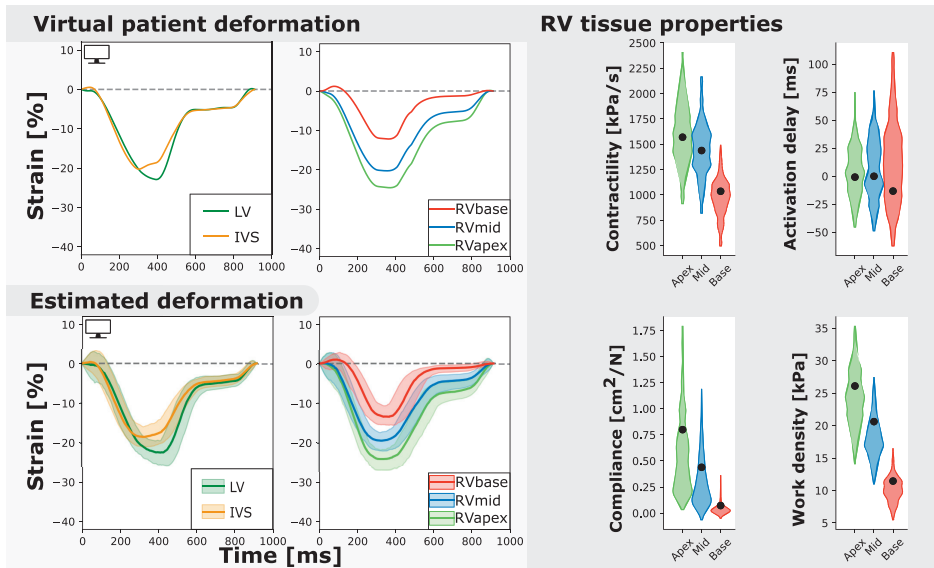


Figure 5.6: Measured and estimated strain of virtual subject (left) and violin plots of estimated parameters (right). Estimated properties are close to the true properties (black dot) and the heterogeneity is well captured. The best simulation in the sample set was closely related to the virtual patients dataset ($\chi^2_{opt} = 2.0$).

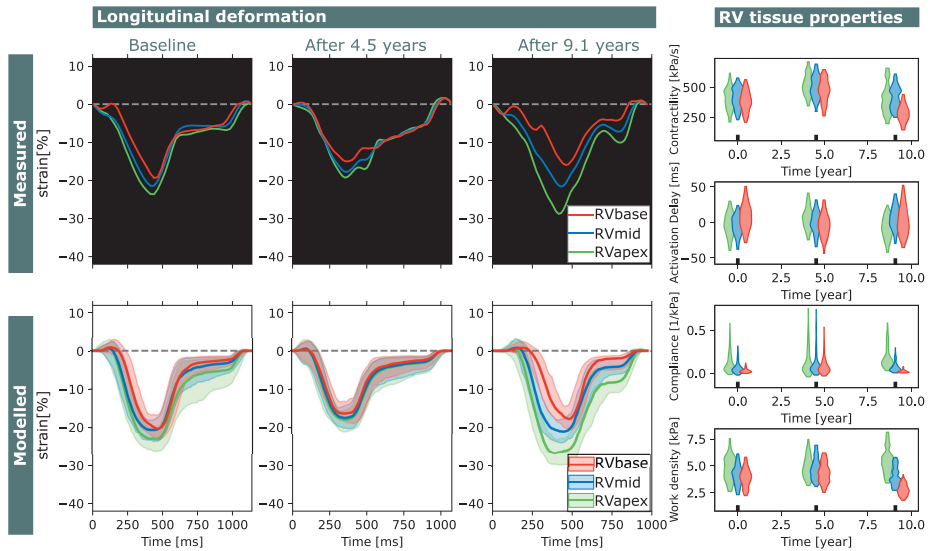


Figure 5.7: Longitudinal estimations subject 1. Echocardiographic deformation imaging was performed at baseline, and after 4.5 and 9.1 years of follow-up. Computer simulations showed homogeneous RV contractility, activation delay, compliance, and work at baseline. At last follow-up, subject 1 developed an abnormal deformation pattern of the basal RV. Estimation of RV tissue properties from these deformation data showed an apex-to-base heterogeneity in activation delay, compliance and work density.

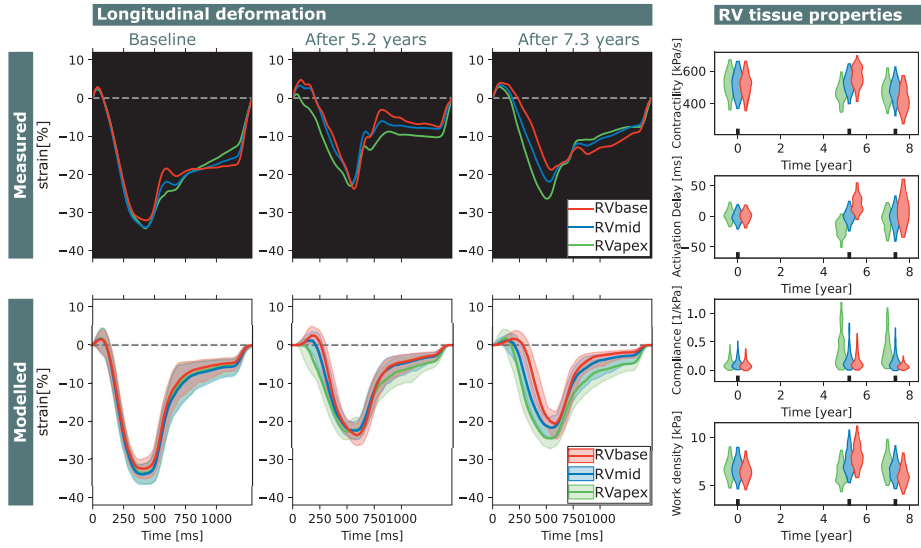


Figure 5.8: Longitudinal estimations subject 2. Echocardiographic deformation imaging was performed at baseline, and after 5.2 and 7.3 years of follow-up. Subject 2 had normal RV deformation patterns at baseline and did not develop clear deformation abnormalities during follow-up. Contractility, compliance, and work density were estimated homogeneously at baseline.

Discussion

In this work, we successfully applied adaptive multiple importance sampling (AMIS) to estimate posterior distributions of model parameters describing local passive and active tissue behaviour based on echocardiographic deformation measurements. Estimated deformation closely resembled the clinically measured myocardial deformation with a realistic level of uncertainty originating from both the measurement and the model. Estimated RV tissue properties reflected progression of the disease substrate over time present in the clinical case studies.

Model-based inference

Personalization of cardiac computational models is becoming more popular and several approaches have been proposed. Schiavazzi et al. [7] used MCMC to estimate model parameters in a simplified model of the single-ventricular heart in a close-looped circulation, based on clinically measured pressures and flows. Corrado et al. [23] used a Reduced Order Unscented Kalman Filter to estimate model parameters to optimize body surface potential maps and myocardial displacement. Meiburg et al. [8] used the Unscented Kalman Filter to predict post-intervention haemodynamics after trans-aortic valve implantation. Zenker [24] used importance sampling to estimate model

parameters in a cardiovascular model. Dhamala et al. [25] used high-dimensional Bayesian optimization for parameter personalization of a cardiac electrophysiological model. Coveney and Clayton [26] used history matching to calibrate the maximum conductance of ion channels and exchangers in two detailed models of the human atrial action potential against measurements of action potential biomarkers. Daly et al. [27] used sequential Monte Carlo Approximate Bayesian Inference to quantify the uncertainty amplification resulting in a cellular action potential model. Camps et al. [28] used the same technique to estimate key ventricular activation properties based on non-invasive electrocardiography and cardiac magnetic resonance imaging.

These studies used computational models with different levels of model complexity in both anatomical and physiological detail. Complex models allow personalization with a high number of details, however, they suffer from a high-dimensional unknown space increasing the difficulty of personalization due to unidentifiability of the model parameters. This problem can be solved by reducing the complexity of the optimization problem by assuming global model parameters [29] or regional model parameters [30]. However, this does not reduce the computational cost and increases model discrepancy. It is suggested to use a surrogate model to approximate the exact posterior probability density function [31], but this creates a new source of uncertainty. Including model discrepancy in the estimation often fails due to the non-identifiability between model parameter estimations and model discrepancy [32]. The pseudo-true parameter value found by ignoring model discrepancy can still be valuable for clinical interpretation.

Another approach is to reduce the complexity of the model. Various lumped parameter models of the heart and circulation have been used for fast personalization [7,8,24]. The cost of low complexity may lead to an increase in model discrepancy due to model assumptions and simplifications [32]. It was, however, demonstrated before that the CircAdapt model is highly efficient in simulating regional mechanics and is able to simulate realistic haemodynamics [21,33]. We previously showed that the CircAdapt model can simulate segmental mechanics with a similar spatial resolution as in clinical strain imaging measurements with low discrepancy [4,21]. Therefore, we assume the CircAdapt model is a suitable model for modelling regional strain in AC patients.

In this study, we chose importance sampling because it is highly effective for complex high-dimensional models [11]. The computational cost of our model was approximately 1000 times higher compared to the calculation of the probability density of a sample drawn from the proposal distribution. Therefore, AMIS was the most suitable variant to optimally reuse all samples [10].

Efficiency of AMIS heavily depends on the definition of the proposal distribution [11]. A wider proposal distribution ensures to visit the full input space of interest, but is

accompanied by a risk of non-converging estimations due to the high number of samples with a low sample weight. On the other hand, a more narrowed search has the risk of finding a local minimum in which the wrong posterior is estimated, or the risk of collapsing when the weight of the found minimum drops to zero. As the number of samples goes to infinity, the sample weight will be equally distributed. However, for the limited number of samples drawn, an optimal balance should be found. We successfully implemented annealed adaptive importance sampling to prevent the model from premature convergence while still being able to narrow the proposal distribution in the later iterations. More research should go into defining the proposal distribution or the initial proposal distribution.

In this study, it took approximately 16h per dataset to converge. This time includes generating the proposal distributions, generating samples, running simulations, obtaining the likelihood function, and calculating the sample weights. The total duration mainly depends on the duration of each individual simulation, since the number of iterations in the estimations was equal or close to 500. The duration of each simulation depended on heart rate, numerical stability, and number of beats needed to get a haemodynamically stable solution. Computational time can be reduced in future studies, since AMIS allows parallel calculation of simulations. This reduction in computational time will be essential for clinical application of our method on a larger scale.

Uncertainty Quantification in Arrhythmogenic Cardiomyopathy

Cardiovascular models are, in general, complex models with a multitude of parameters. To create Digital Twins with the CircAdapt model, we used a parameter subset that we determined in a previous study [3]. This subset includes model parameters related to regional RV contractile function, compliance, and activation delay. This is in line with functional and structural myocardial changes found in AC patients (e.g. fibro-fatty replacement of myocytes [6], altered calcium handling [34], and fibrosis [35]) and early generic simulation based hypotheses [36]. These structural changes might cause abnormal electrical activation observed in patients with AC [37]. The RV tissue properties are useful to quantify the substrate, however, the model cannot distinguish the cellular origin of the substrate.

The likelihood function was based on our prior knowledge of the pathology. It is not trivial how to include this information as the amount of uncertainty and its dependencies is not known but heavily affects the posterior distribution. In this study, we limited the objectives in the likelihood function to only that information in the longitudinal study that our model can simulate realistically. The main contributor is regional RV strain, as regional deformation abnormalities are found in early stages of the disease [36,38–42]. LV strain, RVD, LV EF, and LV EDV are included in the likelihood to personalize geometric properties

of the model. Because of the complex geometry of the thin-walled RV, our 2D imaging methods did not provide a comprehensive measure of RV size and wall thickness. In future studies, 3D imaging methods might provide a more comprehensive inclusion of geometric variability of the RV. The RVD was included to account for large geometrical differences between patients and geometrical changes over time. Wall volumes were not included in the parameter subset because they were unidentifiable given the available measurements.

Dependencies in strain were partially included by including strain rate and strain differences. Based on the used likelihood function, posterior distributions were estimated with a relatively wide variance (Figure 5.4) suggesting not all parameters are identifiable. The low reproducibility in some parameters (HDI 95% CI [0-79%]) is probably related to this unidentifiability. Heterogeneity in model parameters is, however, well preserved, suggesting that measurements that are sensitive to segment-averaged model parameters should also be included in the likelihood function. Further prospective studies could investigate the error propagation of dependent and independent uncertainties, whether all components of the likelihood are essential to include, and which other measurements should be included to increase the identifiability of the model parameters.

Derived tissue properties were estimated more precise and reproducible compared to model parameters, suggesting that different parameter combinations can result in the same haemodynamic state. Mechanics of the three RV segments were modelled with the same mathematical equations, however, they have different interactions with the surrounding walls as shown in Figure 5.5. Compliance in the basal segment was estimated more precise compared to the other segments (Figure 5.12). This results from the non-linear behaviour of the model, as basal model parameters were differently estimated due to basal deformation abnormalities. Therefore, compliance in the basal segment was less correlated with the other segments.

In this study, we used a single definition for myocardial contractility and compliance related to other more global definitions. There is no consensus on a single indicator for contractility and compliance, and often multiple (non-invasive) measures are used to get an impression. For contractility, the maximum pressure-time derivative dP/dt_{max} is the most commonly used index of contractility in the field of drug safety assessment [43]. Although this measure is preload and afterload dependent, the regional stress-time derivative as local equivalent gives insight in the regional differences in RV contractile function. Other global measures have been proposed to bypass preload and afterload dependencies, such as dP/dt_{max} at a specific pressure [43] or end systolic pressure-volume relation [44]. New techniques might be useful for future validation of RV tissue properties, such as shear wave imaging [45] to quantify cardiac stiffness.

The gold-standard assessment of RV stiffness (inverse of compliance) is the end diastolic pressure-volume relation [46]. The local equivalent is the models material law

describing the stress-sarcomere length relation. The actual amount of stress prescribed by this law depends on the sarcomere length during the cycle [19]. Due to the complexity of the model, which includes mechanics based on sarcomere length, an accurate estimation of compliance is difficult. The compliance measure as used in this study only includes the compliance at the end diastolic sarcomere length and is therefore load-dependent. To obtain a load-independent measure, more information on the loading conditions should be included in the likelihood distribution.

Case study and future research directions

The two subjects included in the case study showed different behaviour over time. The first subject developed an abnormal basal RV deformation pattern during follow-up which was reflected in changes in estimated local tissue properties. The second subject did not develop clear deformation abnormalities, but did develop slight abnormal heterogeneity in tissue properties. In both cases, only small changes in estimations were observed from baseline to follow-up. It has previously been shown that heterogeneity in deformation patterns has prognostic value for disease progression [38] and life-threatening arrhythmia [39]. Although no further follow-up of these subjects was available, we can hypothesize our model might identify abnormal tissue substrates before this is clearly visible in deformation patterns. Further studies should investigate whether our approach is able to detect AC in an early stage and whether it has added prognostic value.

In this study, we estimated model parameters to predict tissue mechanics under mechanical loading similar to loading during measurement. To achieve this, we included CO in the parameter subset and EDV and EF in the likelihood function. The model could be used for predicting the behaviour of the heart under different loading conditions. This could facilitate the study of loading effects of drug interventions in the Digital Twin. Besides, the effect of exercise, which is an important modulator of phenotypic expression of AC [47], could be studied in the Digital Twin. For the latter, a virtual cardiac exercise performance test as proposed by Van Loon et al.[48] could be used to give more insight in the severity of the substrate and possible triggers for disease progressions. To allow the CircAdapt model to extrapolate its state to other loading conditions such as exercise, more information should be included.

Limitations

Uncertainties are assumed statistically independent and additive, however, this is in fact more complicated. Measurements have multiple sources for uncertainty. We have only included inter- and intra-observer variability of the speckle tracking imaging in our study. Global longitudinal strain has proven to be reproducible, however, it has been

shown that beat-to-beat variability affects segmental peak strain, end systolic strain and post-systolic strain.[49] More research should elucidate the origin of this uncertainty, its effect on normalized strain morphology as included in our study, and how to optimally include uncertainty in defining the likelihood function. This could also facilitate inclusion of realistic noise on virtual patient datasets, which was outside the scope of this study.

AC is not only characterized by structural disease manifestation, but electrophysiologic substrates play an important role as well [50]. Currently, the CircAdapt model only contains the lumped effect of electrophysiology to describe the mechanical behaviour. Future studies could extend the model with a more detailed electromechanical coupling, such as proposed by Lyon et al. [51], to be able to describe the electrophysiologic substrate.

Conclusion

We presented a patient-specific modelling approach taking into account uncertainties. With this approach, we were able to reproduce regional ventricular deformation patterns and estimate the underlying tissue properties in AC mutation carriers with an acceptable level of uncertainty. Virtual estimations were precise and real-world estimations were highly reproducible. Two subjects in our case study revealed the evolution of early-stage AC disease over time using longitudinal follow-up datasets. Future studies should apply our method on a larger cohort and investigate the course of early stage RV disease development at individual as well as patient population levels.

References

1. Niederer SA, Lumens J, Trayanova NA. 2019 Computational models in cardiology. *Nat. Rev. Cardiol.* **16**, 100–111. (doi:10.1038/s41569-018-0104-y)
2. Corral-Acero J *et al.* 2020 The 'Digital Twin' to enable the vision of precision cardiology. *Eur. Heart J.* **41**, 4556–4564B. (doi:10.1093/eurheartj/ehaa159)
3. van Osta N *et al.* 2020 Parameter subset reduction for patient-specific modelling of arrhythmogenic cardiomyopathy-related mutation carriers in the CircAdapt model: Parameter Subset Reduction. *Philos. Trans. R. Soc. A Math. Phys. Eng. Sci.* **378**, 20190347. (doi:10.1098/rsta.2019.0347)
4. Van Osta N *et al.* 2021 Electromechanical substrate characterization in arrhythmogenic cardiomyopathy using imaging-based patient-specific computer simulations. *Europace* **23**, 153–160. (doi:10.1093/europace/euaa407)
5. Thiene G, Nava A, Corrado D, Rossi L, Pennelli N. 1988 Right Ventricular Cardiomyopathy and Sudden Death in Young People. *N. Engl. J. Med.* **318**, 129–133. (doi:10.1056/NEJM198801213180301)
6. Basso C, Corrado D, Marcus FI, Nava A, Thiene G. 2009 Arrhythmogenic right ventricular cardiomyopathy. *Lancet* **373**, 1289–1300. (doi:10.1016/S0140-6736(09)60256-7)
7. Schiavazzi DE, Baretta A, Pennati G, Hsia TY, Marsden AL. 2017 Patient-specific parameter estimation in single-ventricle lumped circulation models under uncertainty. *Int. j. numer. method. biomed. eng.* **33**, 1–34. (doi:10.1002/cnm.2799)
8. Meiburg R, Zelis JM, van 't Veer JM, van Velthoven SJA, van de Vosse FN, Tonino PAL, Rutten MCM. 2021 Model-based aortic power transfer: A potential measure for quantifying aortic stenosis severity based on measured data. *Med. Eng. Phys.* **90**, 66–81. (doi:10.1016/j.medengphy.2021.02.009)
9. Dhamala J, Arevalo HJ, Sapp J, Horáček BM, Wu KC, Trayanova NA, Wang L. 2018 Quantifying the uncertainty in model parameters using Gaussian process-based Markov chain Monte Carlo in cardiac electrophysiology. *Med. Image Anal.* **48**, 43–57. (doi:10.1016/j.media.2018.05.007)
10. Cornuet JM, Marin JM, Mira A, Robert CP. 2012 Adaptive Multiple Importance Sampling. *Scand. J. Stat.* **39**, 798–812. (doi:10.1111/j.1467-9469.2011.00756.x)
11. Bugallo MF, Elvira V, Martino L, Luengo D, Miguez J, Djuric PM. 2017 Adaptive Importance Sampling: The past, the present, and the future. *IEEE Signal Process. Mag.* **34**, 60–79. (doi:10.1109/MSP.2017.2699226)
12. Li W, Lin G. 2015 An adaptive importance sampling algorithm for Bayesian inversion with multimodal distributions. *J. Comput. Phys.* **294**, 173–190. (doi:10.1016/j.jcp.2015.03.047)
13. Černý V. 1985 Thermodynamical approach to the traveling salesman problem: An efficient simulation algorithm. *J. Optim. Theory Appl.* **45**, 41–51. (doi:10.1007/BF00940812)
14. Neal RM. 2001 Annealed importance sampling. *Stat. Comput.* **11**, 125–139. (doi:10.1023/A:1008923215028)
15. Beskos A, Crisan D, Jasra A. 2014 On the stability of sequential Monte Carlo methods in high dimensions. *Ann. Appl. Probab.* **24**, 1396–1445. (doi:10.1214/13-AAP951)
16. Kirkels FP, Lie ØH, Cramer MJ, Chivulescu M, Rootwelt-Norberg C, Asselbergs FW, Teske AJ, Haugaa KH. 2021 Right Ventricular Functional Abnormalities in Arrhythmogenic Cardiomyopathy: Association With Life-Threatening Ventricular Arrhythmias. *JACC. Cardiovasc. Imaging* **14**, 900–910. (doi:10.1016/j.jcmg.2020.12.028)
17. Marcus FI *et al.* 2010 Diagnosis of Arrhythmogenic Right Ventricular Cardiomyopathy/Dysplasia: Proposed Modification of the Task Force Criteria. *Eur. Heart J.* **31**, 806–814. (doi:10.1093/eurheartj/ehq025)
18. Voigt JU *et al.* 2015 Definitions for a common standard for 2D speckle tracking echocardiography: consensus document of the EACVI/ASE/Industry Task Force to standardize deformation imaging. *Eur. Heart J. Cardiovasc. Imaging* **16**, 1–11. (doi:10.1093/ehjci/jeu184)
19. Arts T, Delhaas T, Bovendeerd P, Verbeek X, Prinzen F. 2005 Adaptation to Mechanical Load Determines Shape and Properties of Heart and Circulation: the CircAdapt Model. *Am. J. Physiol. Heart Circ. Physiol.* **288**, 1943–1954. (doi:10.1152/ajpheart.00444.2004.)
20. Lumens J, Delhaas T, Kirn B, Arts T. 2009 Three-wall segment (TriSeg) model describing mechanics and hemodynamics of ventricular interaction. *Ann. Biomed. Eng.* **37**, 2234–2255. (doi:10.1007/s10439-009-9774-2)
21. Walmsley J, Arts T, Derval N, Bordachar P, Cochet H, Ploux S, Prinzen FW, Delhaas T, Lumens J. 2015 Fast Simulation of Mechanical Heterogeneity in the Electrically Asynchronous Heart Using the MultiPatch Module. *PLoS Comput. Biol.* **11**, 1–23. (doi:10.1371/journal.pcbi.1004284)
22. Freedman D, Diaconis P. 1981 On the histogram as a density estimator:L2 theory. *Zeitschrift für Wahrscheinlichkeitstheorie und Verwandte Gebiete* **57**, 453–476. (doi:10.1007/BF01025868)

23. Corrado C, Gerbeau JF, Moireau P. 2015 Identification of weakly coupled multiphysics problems. Application to the inverse problem of electrocardiography. *J. Comput. Phys.* **283**, 271–298. (doi:10.1016/j.jcp.2014.11.041)
24. Zenker S. 2010 Parallel particle filters for online identification of mechanistic mathematical models of physiology from monitoring data: Performance and real-time scalability in simulation scenarios. *J. Clin. Monit. Comput.* **24**, 319–333. (doi:10.1007/s10877-010-9252-2)
25. Dhamala J, Bajracharya P, Arevalo HJ, Sapp JLL, Horáček BM, Wu KC, Trayanova NA, Wang L. 2020 Embedding high-dimensional Bayesian optimization via generative modeling: Parameter personalization of cardiac electrophysiological models. *Med. Image Anal.* **62**, 101670. (doi:10.1016/j.media.2020.101670)
26. Coveney S, Clayton RH. 2018 Fitting two human atrial cell models to experimental data using Bayesian history matching. *Prog. Biophys. Mol. Biol.* **139**, 43–58. (doi:10.1016/j.pbiomolbio.2018.08.001)
27. Daly AC, Cooper J, Gavaghan DJ, Holmes C. 2017 Comparing two sequential Monte Carlo samplers for exact and approximate Bayesian inference on biological models. *J. R. Soc. Interface* **14**. (doi:10.1098/RSIF.2017.0340)
28. Camps J, Lawson B, Drovandi C, Minchole A, Wang ZJ, Grau V, Burrage K, Rodriguez B. 2021 Inference of ventricular activation properties from non-invasive electrocardiography. *Med. Image Anal.* **73**, 102143. (doi:10.1016/J.MEDIA.2021.102143)
29. Davies V, Noè U, Lazarus A, Gao H, Macdonald B, Berry C, Luo X, Husmeier D. 2019 Fast parameter inference in a biomechanical model of the left ventricle by using statistical emulation. *J. R. Stat. Soc. Ser. C (Applied Stat.)* **68**, 1555–1576. (doi:10.1111/rssc.12374)
30. Dhamala J, Arevalo HJ, Sapp J, Horacek M, Wu KC, Trayanova NA, Wang L. 2017 Spatially adaptive multi-scale optimization for local parameter estimation in cardiac electrophysiology. *IEEE Trans. Med. Imaging* **36**, 1966–1978. (doi:10.1109/TMI.2017.2697820)
31. Paun LM, Colebank M, Qureshi U, Olufsen M, Hill N, Husmeier D. 2019 MCMC with delayed acceptance using a surrogate model with an application to cardiovascular fluid dynamics. *Proc. Int. Conf. Stat. Theory Appl.*, 1–8. (doi:10.11159/icsta19.28)
32. Lei CL *et al.* 2020 Considering discrepancy when calibrating a mechanistic electrophysiology model Subject Areas :
33. Arts T, Lumens J, Kroon W, Delhaas T. 2012 Control of whole heart geometry by intramyocardial mechano-feedback: A model study. *PLoS Comput. Biol.* **8**. (doi:10.1371/journal.pcbi.1002369)
34. van Opbergen CJM *et al.* 2019 Plakophilin-2 Haploinsufficiency Causes Calcium Handling Deficits and Modulates the Cardiac Response Towards Stress. *Int. J. Mol. Sci.* **20**, 4076. (doi:10.3390/ijms20174076)
35. Tandri H *et al.* 2005 Noninvasive detection of myocardial fibrosis in arrhythmogenic right ventricular cardiomyopathy using delayed-enhancement magnetic resonance imaging. *J. Am. Coll. Cardiol.* **45**, 98–103. (doi:10.1016/j.jacc.2004.09.053)
36. Mast TP *et al.* 2016 Right Ventricular Imaging and Computer Simulation for Electromechanical Substrate Characterization in Arrhythmogenic Right Ventricular Cardiomyopathy. *J. Am. Coll. Cardiol.* **68**, 2185–2197. (doi:10.1016/j.jacc.2016.08.061)
37. Haqqani HM, Tschabrunn CM, Betensky BP, Lavi N, Tzou WS, Zado ES, Marchlinski FE. 2012 Layered activation of epicardial scar in arrhythmogenic right ventricular dysplasia possible substrate for confined epicardial circuits. *Circ. Arrhythmia Electrophysiol.* **5**, 796–803. (doi:10.1161/CIRCEP.111.967935)
38. Mast TP *et al.* 2019 The Prognostic Value of Right Ventricular Deformation Imaging in Early Arrhythmogenic Right Ventricular Cardiomyopathy. *JACC Cardiovasc. Imaging*, 14 March. **12**, 446–455. (doi:10.1016/j.jcmg.2018.01.012)
39. Sarvari SI, Haugaa KH, Anfinsen OG, Leren TP, Smiseth OA, Kongsgaard E, Amlie JP, Edvardsen T. 2011 Right ventricular mechanical dispersion is related to malignant arrhythmias: A study of patients with arrhythmogenic right ventricular cardiomyopathy and subclinical right ventricular dysfunction. *Eur. Heart J.* **32**, 1089–1096. (doi:10.1093/eurheartj/ehr069)
40. Leren IS, Saberniak J, Haland TF, Edvardsen T, Haugaa KH. 2017 Combination of ECG and Echocardiography for Identification of Arrhythmic Events in Early ARVC. *JACC Cardiovasc. Imaging* **10**, 503–513. (doi:10.1016/j.jcmg.2016.06.011)
41. Lie ØH, Rootwelt-Norberg C, Dejgaard LA, Leren IS, Stokke MK, Edvardsen T, Haugaa KH. 2018 Prediction of Life-Threatening Ventricular Arrhythmia in Patients with Arrhythmogenic Cardiomyopathy. *JACC Cardiovasc. Imaging* **11**, 2660. (doi:10.1016/j.jcmg.2018.05.017)

42. Malik N *et al.* 2020 Right ventricular strain predicts structural disease progression in patients with arrhythmogenic right ventricular cardiomyopathy. *J. Am. Heart Assoc.* **9**, 1–9. (doi:10.1161/JAHA.119.015016)
43. Sarazan RD, Mittelstadt S, Guth B, Koerner J, Zhang J, Pettit S. 2011 Cardiovascular function in nonclinical drug safety assessment: Current issues and opportunities. *Int. J. Toxicol.* **30**, 272–286. (doi:10.1177/1091581811398963)
44. Suga H, Sagawa K. 1974 Instantaneous pressure volume relationships and their ratio in the excised, supported canine left ventricle. *Circ. Res.* **35**, 117–126. (doi:10.1161/01.RES.35.1.117)
45. Pernot M, Couade M, Mateo P, Crozatier B, Fischmeister R, Tanter M. 2011 Real-time assessment of myocardial contractility using shear wave imaging. *J. Am. Coll. Cardiol.* **58**, 65–72. (doi:10.1016/j.jacc.2011.02.042)
46. El Hajj MC, Viray MC, Tedford RJ. 2020 Right Heart Failure: A Hemodynamic Review. *Cardiol. Clin.* **38**, 161–173. (doi:10.1016/j.ccl.2020.01.001)
47. Prior D, La Gerche A. 2020 Exercise and Arrhythmogenic Right Ventricular Cardiomyopathy. *Hear. Lung Circ.* **29**, 547–555. (doi:10.1016/j.hlc.2019.12.007)
48. van Loon T, Knackstedt C, Cornelussen R, Reesink KD, Brunner La Rocca H-P, Delhaas T, van Empel V, Lumens J. 2020 Increased myocardial stiffness more than impaired relaxation function limits cardiac performance during exercise in heart failure with preserved ejection fraction: a virtual patient study. *Eur. Hear. J. - Digit. Heal.* **1**, 40–50. (doi:10.1093/ehjdh/ztaa009)
49. Mirea O *et al.* 2018 Variability and Reproducibility of Segmental Longitudinal Strain Measurement: A Report From the EACVI-ASE Strain Standardization Task Force. *JACC Cardiovasc. Imaging* **11**, 15–24. (doi:10.1016/j.jcmg.2017.01.027)
50. Groeneweg JA *et al.* 2015 Clinical Presentation, Long-Term Follow-Up, and Outcomes of 1001 Arrhythmogenic Right Ventricular Dysplasia/Cardiomyopathy Patients and Family Members. *Circ. Cardiovasc. Genet.* **8**, 437–446. (doi:10.1161/CIRCGENETICS.114.001003)
51. Lyon A, Dupuis LJ, Arts T, Crijns HJGM, Prinzen FW, Delhaas T, Heijman J, Lumens J. 2020 Differentiating the effects of β -adrenergic stimulation and stretch on calcium and force dynamics using a novel electromechanical cardiomyocyte model. *Am. J. Physiol. - Hear. Circ. Physiol.* **319**, H519–H530. (doi:10.1152/ajpheart.00275.2020)

6



Monitoring age-related Penetrance of Structural Right Ventricular Disease in Arrhythmogenic Cardiomyopathy

Feddo P Kirkels*, **Nick van Osta***, Christine Rootwelt-Norberg, Monica Chivulescu, Øyvind Lie, Folkert W. Asselbergs, Maarten J. Cramer, Tammo Delhaas, Arco J. Teske, Kristina H. Haugaa, Joost Lumens (**in preparation**)

*NvO and FK contributed equally.

Abstract

Arrhythmogenic cardiomyopathy (AC) is a heritable cardiomyopathy characterized by fibrofatty replacement of primarily the right ventricular (RV) myocardium and risk of life-threatening ventricular arrhythmias. Life-long repeated cardiac imaging of relatives at risk is important to detect penetrant disease in an early stage. However, it is currently not known whether structural disease progression occurs in all age groups, hampering age-tailored follow-up protocols.

To evaluate structural progression in different stages of life, in order to facilitate age-tailoring of follow-up protocols in early AC.

We included 82 early stage AC patients and genotype positive family members (57% female, age 39 ± 17 years, 10% probands) from a consecutive cohort evaluated at Oslo University Hospital, Rikshospitalet, Norway. Patients were divided into three groups based on age at baseline: early presenters (<30 years), mid-life presenters (30-50 years) and late presenters (>50 years). A total of 313 baseline and follow-up echocardiographic assessments were included with a mean follow-up of 6.7 ± 3.3 years. Both global and segmental deformation characteristics deteriorated in all three age-groups. Regional RV tissue properties were estimated based on patient specific deformation characteristics using a recently developed computational modelling framework. The development of local tissue substrates in the RV free wall was expressed in increased heterogeneity in estimated RV tissue properties.

This study showed that deformation imaging can be used to follow-up disease progression in early AC. Patient-specific computer simulations showed the development of a tissue substrate affecting regional RV tissue properties. Since structural progression was seen in all age-groups, age-tailoring of follow-up intervals for cardiac imaging is not supported by our data.

Introduction

Arrhythmogenic cardiomyopathy (AC) is a heritable cardiomyopathy characterized by fibrofatty replacement of primarily the right ventricular (RV) myocardium and risk of life-threatening ventricular arrhythmias [1,2]. Variable disease expression is found in familial AC [3], ranging from sudden cardiac death (SCD) in young individuals to a lifelong absence of any phenotype. To prevent apparently healthy AC mutation carriers from SCD, early detection of potentially pro-arrhythmic tissue substrates is important.

AC has an age-related penetrance, whereby patients classically present in the third or fourth decade of life with symptomatic ventricular arrhythmias [3–7]. However, with increased use of genetic testing for AC, carriers of a (likely-)pathogenic variant across all age-groups are recognized and included in extensive cardiac screening protocols. When a clear phenotype is absent on initial screening, these patients frequently undergo cardiac imaging examinations for detection of early signs of structural disease. It is however currently not known whether structural disease progression occurs in all age groups, hampering age-tailored follow-up protocols. On top of that, conventional echocardiographic measurements included in the 2010 diagnostic task force criteria (TFC) [8] lack sensitivity for detection of early structural disease substrates in AC.

Echocardiographic deformation imaging has emerged over the past decade as a valuable tool for both early detection and prognosis in AC

[9–15]. In this study, we used echocardiographic deformation imaging for follow-up of mechanical alterations in patients with early AC. Besides, we performed imaging-based patient-specific computer simulations to estimate tissue properties of the underlying disease substrate. By using these two methods, we aimed to evaluate structural progression in different stages of life, in order to facilitate age-tailoring of follow-up protocols in early AC.

Methods

Study design and population

We included a consecutive cohort of AC patients and genotype positive family members which were evaluated at Oslo University Hospital, Rikshospitalet, Norway, between 1997 and 2020 with at least two complete clinical evaluations. Part of this cohort was reported in previous follow-up studies in AC patients [16,17]. Patients with previous myocardial infarction and congenital heart disease were excluded. To focus on patients with early stage structural disease, patients with a major echocardiographic 2010 task force criterion (TFC) at baseline were excluded. Also patients who experienced a life-

threatening ventricular arrhythmia (VA, defined as a documented history of sustained ventricular tachycardia, aborted cardiac arrest, or appropriated ICD therapy) at or prior to inclusion were excluded.

Clinical characteristics were recorded at baseline. Patients were divided into three age-groups: early presenters (<30 years), mid-life presenters (30-50 years) and late presenters (>50 years). Time to first life-threatening VA was recorded prospectively from time of inclusion. End of observation was cardiac transplantation, death, or last-clinical follow-up by December 1, 2020.

All patients gave written informed consent. The study complied with the declaration of Helsinki and was approved by the Regional Ethical Committee of South-Eastern Norway.

Echocardiography

All available complete echocardiographic examinations in sinus rhythm between inclusion and last clinical follow-up were analysed. Inclusion was defined at the time of first echocardiography on compatible hardware (GE Vivid 7, E9, or E95, EchoPac 203, GE Vingmed, Horten, Norway). Presence of echocardiographic TFC[8] and left ventricular (LV) volumes were measured at baseline. LV ejection fraction (EF) by Simpson's biplane method and RV basal diameter (RVD) were measured during follow-up. Speckle tracking deformation imaging of both the LV and RV was performed in all examinations, according to previously described protocols [14,18,19]. We assessed segmental RV deformation patterns in an RV-focused 4-chamber view, whereby a single wall tracing of the RV free wall was automatically divided into a basal, mid, and apical segment. Timing of the pulmonary valve closure was assessed by Doppler traces in the RV outflow tract, obtained in the parasternal short-axis view. The following deformation parameters were measured in the basal segment: time to onset of shortening (or electromechanical interval) [19], systolic peak strain[20], and the amount of post-systolic shortening [9]. (definitions in supplemental material) Based on these parameters, a distinction into 3 different deformation patterns has previously been observed in AC and simulated using a computational model [10,21]. Type I is normal deformation; type II is characterized by delayed onset of shortening, reduced systolic peak strain, and minor post-systolic shortening; type III is characterized by little or no systolic peak strain, predominantly systolic stretching, and major post-systolic shortening. The left ventricular global longitudinal strain (GLS) was calculated in a 16-segment left ventricular model [14]. RV free wall longitudinal strain ($RV_{FW}LS$) was defined as the peak negative strain from the global RV free wall deformation characteristic. All measurements were performed by a single observer blinded to clinical information.

Computational simulations

Based on echocardiographic data, patient specific simulations were performed with the CircAdapt model [22], which is a closed-loop lumped parameter computer model of the human heart and circulation. It enables simulation of cardiac haemodynamics with ventricular interactions based on regional wall mechanics, using a phenomenological model describing active and passive myofibre mechanics [23,24]. We used a previously developed modelling framework for patient specific estimation of tissue properties in the CircAdapt model [25]. This framework uses, besides LV and RV deformation data, also EDV, EF and RVD as input. Measurement uncertainty was included in the framework and resulted in an uncertainty on the estimated tissue properties. Four RV tissue properties were estimated: contractility, compliance, activation delay and myocardial work. In brief, segmental contractility was defined as the maximum rate of active stress rise, which can be seen as the equivalent of the maximum rate of ventricular systolic pressure rise (dP/dt_{max}) on a local tissue level. Segmental wall compliance was defined as the slope of the end diastolic myofibre stress–strain relationship at time before first ventricular activation and can be interpreted as the regional equivalent of the slope of the global end diastolic pressure–volume relation. Myocardial work density was defined as the area within the stress–strain loop and can be interpreted as the regional equivalent of global stroke work [25].

Statistical analysis

Statistical analyses were performed using IBM SPSS 25.0 (IBM Corp, Armonk, NY, USA) and Stata SE 16.1 (StataCorp LLC, TX, USA). Values were expressed as mean with standard deviations (SDs) and standard error (SE), frequencies with percentages or median with interquartile range (IQR), and were compared by Fisher's exact test for dichotomous variables and Kruskal Wallis test for continuous variables.

We assessed progression in the three age-groups by entering key parameters from the echocardiographic assessment and the model estimations of RV tissue properties into a linear mixed model with random intercept and exchangeable covariance structure. Heterogeneity in estimated tissue properties was assessed as the normalized standard deviation of tissue properties of the 3 RV free wall segments and was also entered into the linear mixed model. P-values were two-sided, and values <0.05 were considered significant.

Results

Clinical characteristics

We included 82 early stage AC patients and genotype positive family members (57% female, age 39 ± 17 years, 10% probands, Table 6.1). A (likely-)pathogenic variant was found in 92%

of patients, mostly located in the PKP2 gene (84%). During a mean follow-up time of 6.7 ± 3.3 years, a total of 355 echocardiograms were performed (average of 4 exams per patient, range 2 – 9). Forty-two exams were excluded due to irregular heart rhythm or inadequate visualization of one or more RV free wall segments. During follow-up, 6 patients experienced a first life-threatening VA, after a mean of 4 years (range 0.2 – 8.9 years).

Progression of deformation abnormalities

In a linear mixed model analysis of 313 echocardiographic assessments, both global (Figure 6.1) and segmental (Figure 6.2) deformation characteristics deteriorated in all three age-groups. Deterioration in LVEF was not observed in any of the age groups (-0.03% per year [95% CI -0.16 to 0.09], but LV function deteriorated by absolute 0.1% per year (95% CI 0.05 to 0.15) worsening of GLS. Deterioration was faster in the RV lateral wall, expressed by a mean worsening of absolute 0.6% per year (95% CI 0.46 to 0.70). The three segmental deformation characteristics used to classify RV deformation type showed that the basal segment was most impaired in all age-groups, whereby an apex-to-base gradient was maintained during follow-up. (Figure 6.2) When displaying progression of the deformation types during follow-up (Figure 6.3), the deformation pattern of the basal segment was most frequently impaired (type II or III). Progression to a more abnormal deformation pattern occurred in all age groups, whereby the pattern in the basal segment deteriorated in about half of the cases and in the mid segment in about one third. Deformation in the apical segment was normal in most cases, and progression to an abnormal deformation pattern was less likely. (Yearly progression rates and mean values at baseline and last follow-up are provided in Supplemental Table S6.1)

Table 6.1. Baseline table. Values are mean \pm SD, median (IQR), or frequencies (%).

	Total (n = 82)	Age <30 (n = 27)	30 < Age < 50 (n = 32)	Age > 50 (n = 23)	p-value
Age (years)	39 ± 17	20 ± 6	39 ± 6	60 ± 7	<0.001
Female sex, n (%)	47 (57%)	15 (56%)	20 (63%)	12 (52%)	0.723
Proband, n (%)	8 (10%)	0 (0%)	4 (13%)	4 (17%)	0.064
Follow-up time (years)	6.5 ± 3.1	7.1 ± 2.9	6.9 ± 3.5	5.2 ± 2.5	0.109
VA during follow-up, n (%)	6 (7%)	0 (0%)	4 (13%)	2 (9%)	0.197
Pathogenic mutation, n (%)	75 (92%)	27 (100%)	29 (91%)	19 (83%)	0.077
PKP2, n (%)	69 (84%)	24 (89%)	28 (88%)	17 (74%)	0.326
DSG, n (%)	5 (6%)	2 (7%)	1 (3%)	2 (9%)	0.616
DSP, n (%)	1 (1%)	1 (4%)	0 (0%)	0 (0%)	0.610

Abbreviations: DSG2, desmoglein-2 gene; DSP, desmoplakin gene; PKP2, plakophilin-2 gene; VA, life-threatening ventricular arrhythmias.

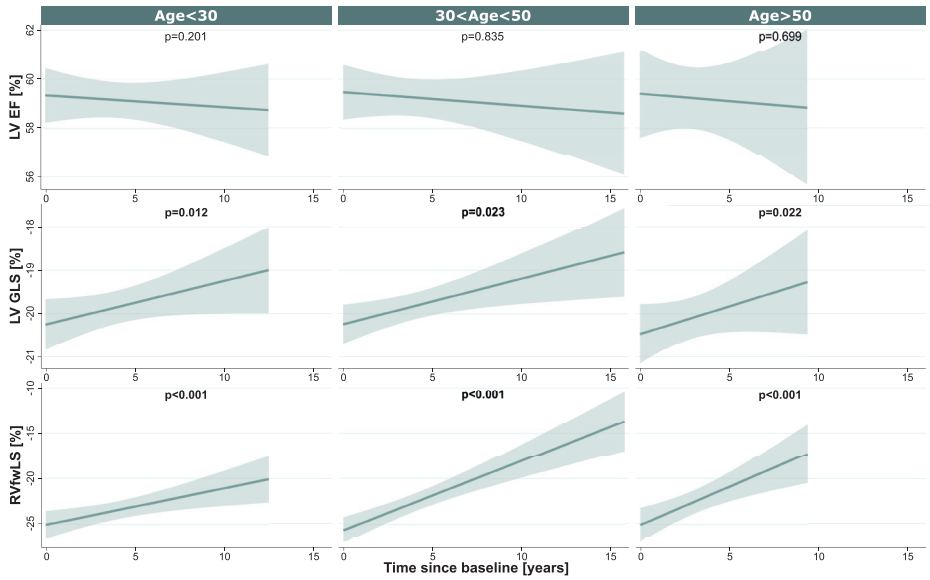


Figure 6.1. Progression of left ventricular (LV) ejection fraction (LVEF), LV global longitudinal strain (LV GLS), and right ventricular free wall longitudinal strain (RVfwLS), separated by age-group. Shown p-values are for progression during follow-up.

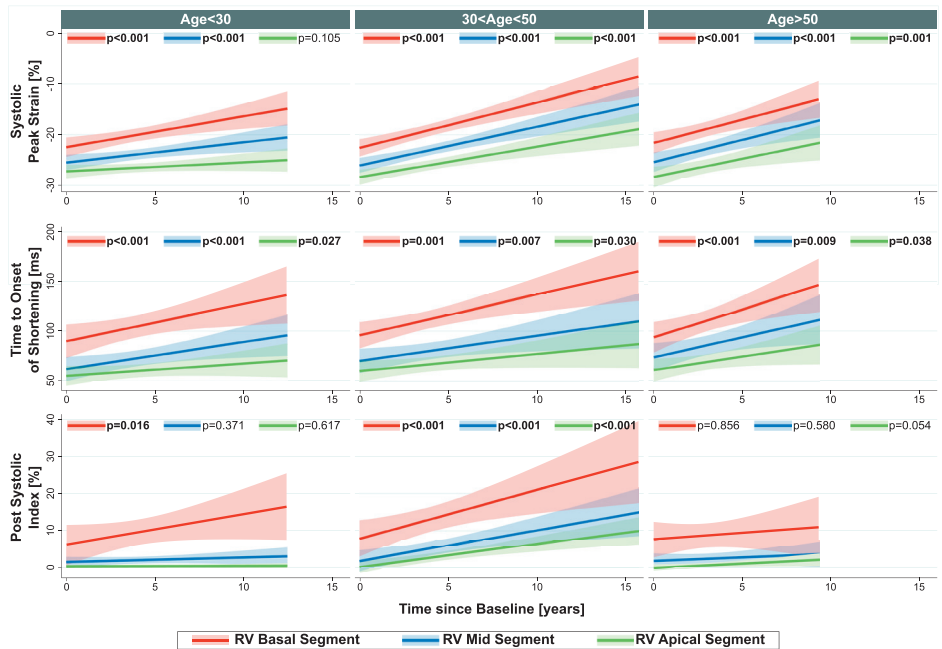


Figure 6.2. Progression of segmental deformation parameters of the right ventricle (RV), separated by age-group. Shown p-values are for progression during follow-up.

Progression of modelled RV tissue properties

Progression of the estimated contractility, compliance, activation delay, and work density was not consistently seen. (Figure 6.4, Supplemental Table S6.2) Contractility of the basal segment decreased in the first two age-groups ($p = 0.005$ and $p = 0.022$, respectively). Estimated compliance increased in the apical segment in all age-groups. When focusing on heterogeneity within the RV free wall, a clear increase was seen for all estimated RV tissue properties in patients below the age of 30 at inclusion. (Figure 6.5, Supplemental Table S6.3) In the two older age-groups, increasing heterogeneity was also observed, but not significant in all four tissue properties.

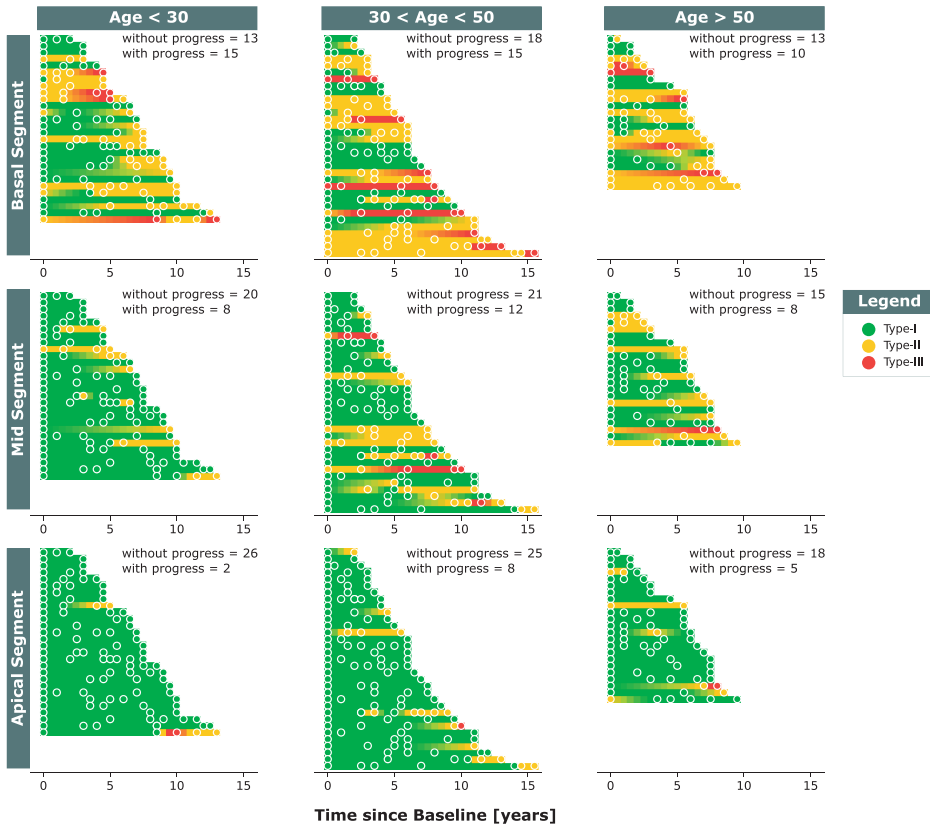


Figure 6.3. Progression of right ventricular (RV) deformation types in the three RV free wall segments, separated by age-group.

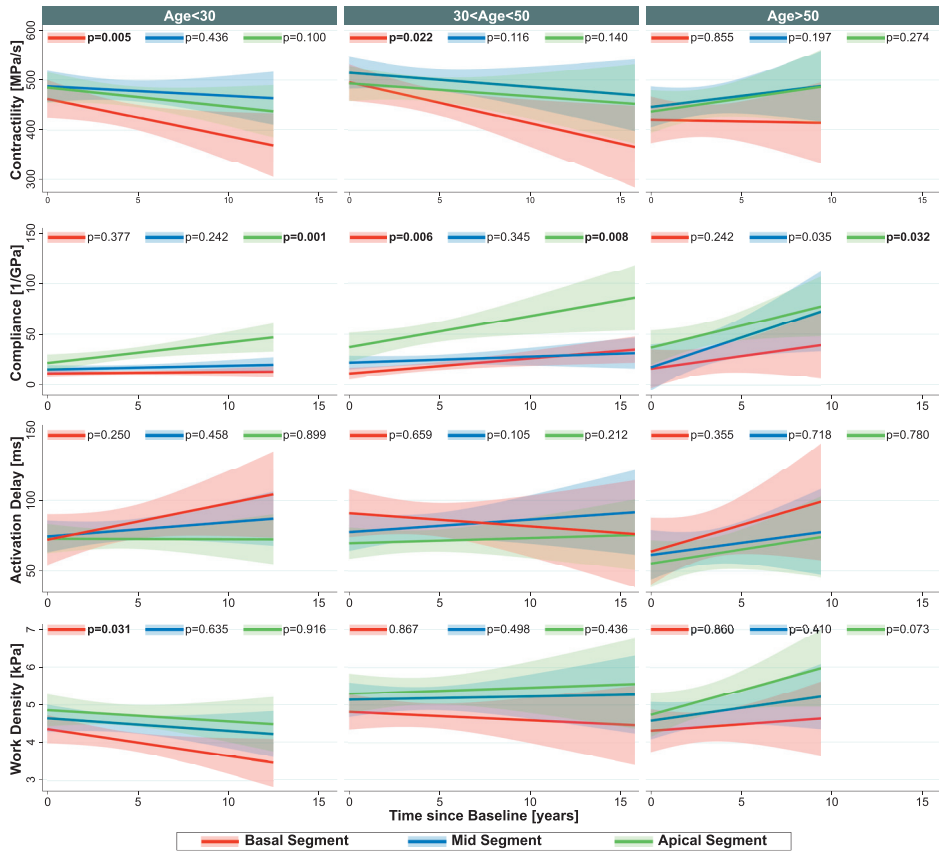


Figure 6.4. Progression of modelled right ventricular tissue properties, separated by age-group.

Case studies of progression

Subject 1 experienced a life-threatening ventricular arrhythmia 2.9 years after baseline evaluation (Figure 6.6). During the first examination, RV deformation was slightly abnormal in the basal segment, with delayed onset of shortening, slightly reduced peak strain and mild post-systolic shortening. During follow-up, deformation patterns became increasingly abnormal in all RV segments, whereby the basal pattern was most effected. The apex-to-base heterogeneity was also expressed in the estimated RV tissue properties. Heterogeneity was first observed in the activation delay and later also in contractility, compliance and work density.

Subject 2 experienced a life-threatening ventricular arrhythmia 5.7 years after baseline evaluation (Figure 6.7). During the first examination, RV deformation was slightly impaired, but contraction in the three segments of the RV free wall was homogeneous. During follow-up, contraction became increasingly heterogenic, whereby deformation in the basal and mid segment was most abnormal. The apex-to-base heterogeneity was also expressed in the estimated RV tissue properties of the two follow-up examinations and preceded the arrhythmic event.

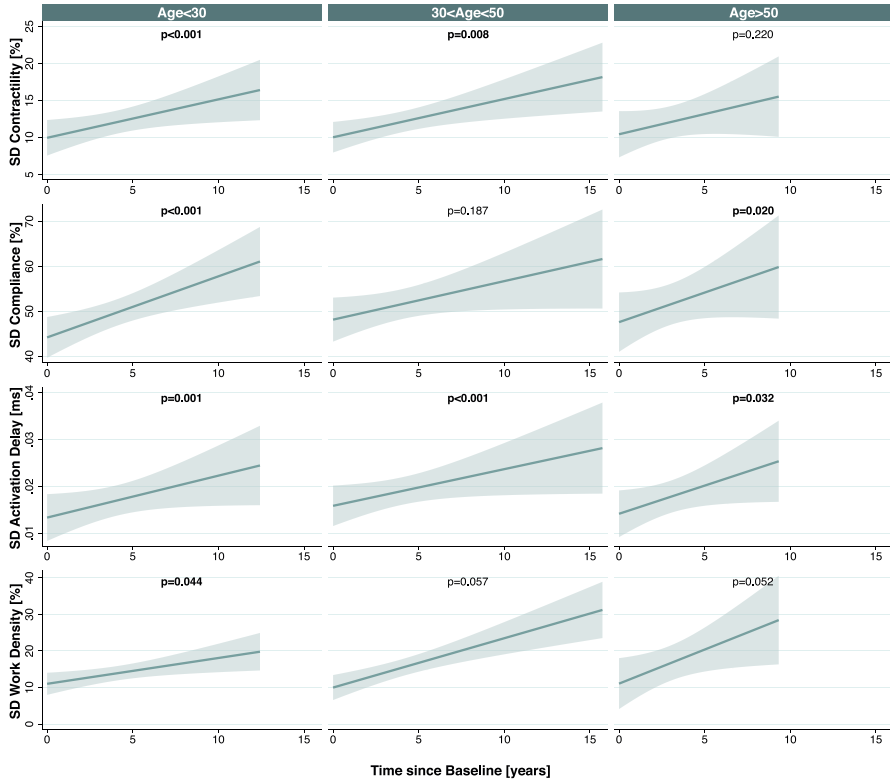


Figure 6.5. Progression of heterogeneity in estimated RV tissue properties between the three RV free wall segments, separated by age-group.

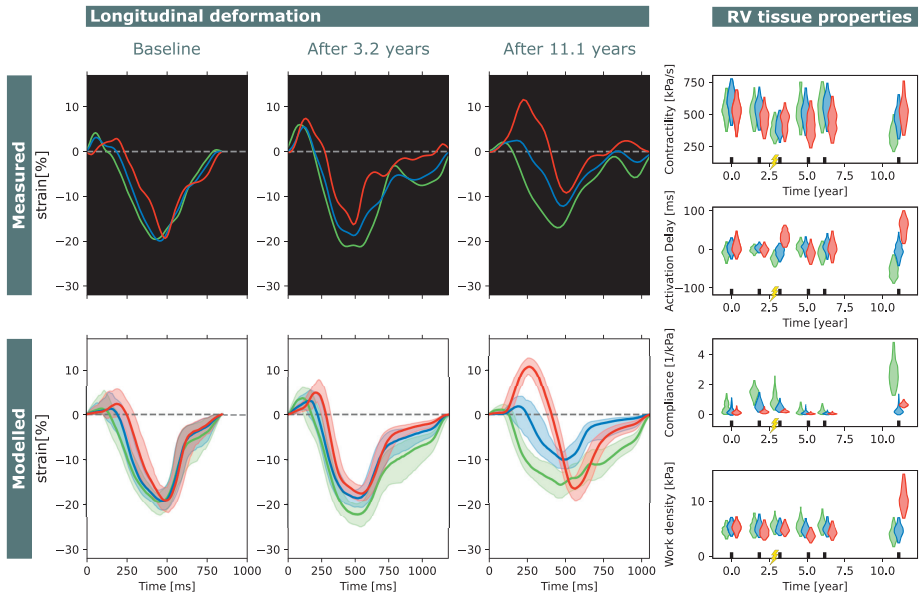


Figure 6.6. Case study patient 1. The patient experienced a life-threatening ventricular arrhythmia 2.9 years after the baseline evaluation.

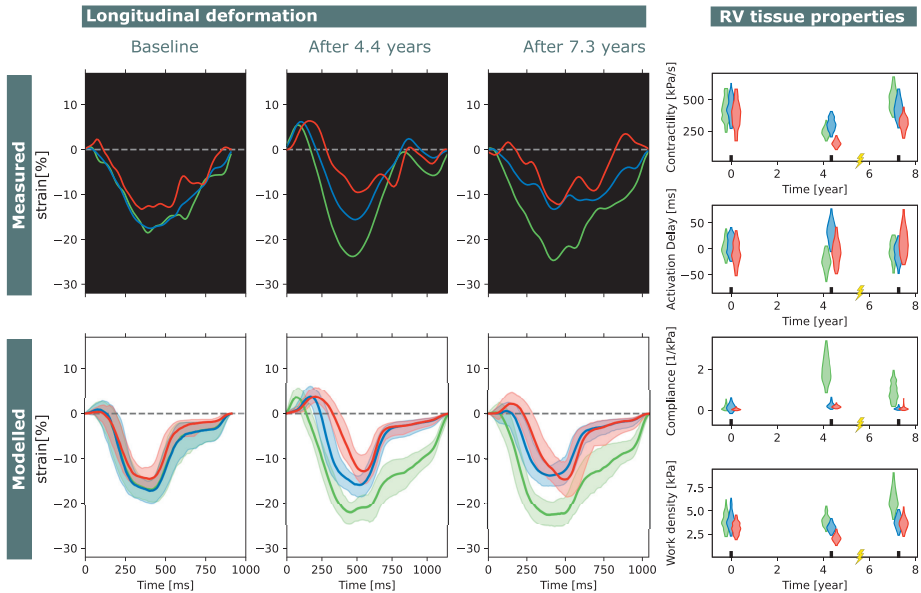


Figure 6.7. Case study patient 2. The patient experienced a life-threatening ventricular arrhythmia 5.7 years after the baseline evaluation.

Discussion

In this study, we have used echocardiographic deformation imaging and computational simulations to evaluate structural disease progression in different age-groups in early AC. We found that LV GLS and most right ventricular deformation abnormalities progressed in all age-groups. Based on these findings, age-tailoring of follow-up intervals would not be recommended.

The computational model was not able to provide extra insight in the underlying disease substrate when looking at absolute values of estimated RV tissue properties on a group level. However, a clear increase in regional heterogeneity revealed progressive local tissue substrates on a group level. On top of that, when applying computational simulations accounting for uncertainty on a patient specific level, estimations can provide extra insight in the etiology of progressive substrates.

Age-related penetrance in AC

(Likely-)pathogenic AC variants are associated with incomplete penetrance and varied disease expression. The penetrance is age-related with onset typically observed in the third and fourth decade of life [3,4,6,7]. Disease expression is, however, recognized in adolescents [3,26,27]. Therefore, a recent expert consensus statement recommended

clinical evaluation with 12-lead ECG, ambulatory ECG and cardiac imaging every 1-3 years starting at 10-12 years of age [7].

While early recognition of disease expression is valuable, prevention of SCD is the most important goal of AC screening. Prior studies report SCD rates up to 23% at presentation, mainly in young AC patients [3,4]. In a cohort study of AC patients who presented ³50 years of age, ventricular tachycardia and pre-existing structural abnormalities were common, but sudden cardiac death was not observed [5]. The latter raises the question at what age you can stop the frequent and demanding screening of AC patients and relatives. In a position statement from 2010, it was suggested that serial screening of relatives can be stopped at the age of 50-60 years, due to completed penetrance [28]. Our study showed progression of deformation abnormalities in both early-, mid-, and late-presenters without an overt structural AC phenotype at baseline, contradicting the statement of completed penetrance after 50 years of age.

Progression of deformation abnormalities

Our study showed that deformation imaging is a useful technique for follow-up of structural disease progression in AC. In a previous study on serial evaluation of AC relatives, one-third showed electrical progression during 4 year follow-up and structural progression was rare [29]. However, structural progression was measured by increase in structural 2010 TFC, which lack sensitivity for detection of early disease manifestation [30]. We have previously shown that RV deformation patterns are superior for detection of early disease [31]. In *Figure 6.3* of the current study, these RV deformation types showed to be a robust classification method during serial analyses, which is able to detect progression over time. In segmental analyses, all deformation parameters were worse in the basal segment. This is in line with previous studies in other cohorts, which showed that the subtricuspid segment of the RV lateral wall is the earliest and most severely affected area in AC [10,21,32,33].

Progression of modelled RV tissue properties

Definitive diagnosis of AC is based on the presence of transmural fibro-fatty replacement of RV myocardium at biopsy, autopsy, or surgery [34,35]. As assessment of transmural myocardium is not possible in the vast majority of patients, TFC guide the diagnosis of AC [8]. The use of personalized computational modelling can give more insight in the patient's underlying substrate as estimated tissue properties are directly related to tissue composition. We have previously developed a patient-specific computer modelling approach to estimate tissue properties of the underlying disease substrate based on echocardiographic deformation data [10,25,36,37]. In the current study, we applied this

modelling approach on serial echocardiographic examinations in a large cohort to achieve more insight in the development of early structural disease substrates in AC.

On a group level, repeated estimation of mean RV tissue properties did not add value over the follow-up of deformation parameters. Since the model is based on deformation characteristics, which are load dependent, more information on loading conditions during the examination should be added for precise estimation of tissue characteristics. Therefore, we concluded that more information is needed for reliable estimation of absolute values of RV tissue properties. On the individual patient level, displaying uncertainty can facilitate more reliable interpretation and make the estimations more useful.

While estimating absolute values of tissue characteristics will require more information, heterogeneity in deformation patterns was well captured in the estimated tissue properties. Local deformation abnormalities, reflecting local disease substrates, resulted in heterogenic tissue estimations very early in the disease. Hereby, the model has the potential to show the consecution of development of local electric and structural abnormalities.

In the two case studies of patients who experienced a life-threatening ventricular arrhythmia while no overt structural phenotype was found by conventional TFC, RV deformation abnormalities and heterogeneity in estimated tissue properties preceded the arrhythmic event. These cases illustrate the potential use of the modelling approach on a patient specific basis, as estimated abnormalities which are present prior to an event might have predictive value. The number of events in this study was however too low to draw any firm conclusions from these findings.

Clinical implications

Cascade genetic screening confronts clinicians with an increasing group of patients at risk of severe arrhythmic events, but without an overt phenotype at first evaluation. These patients undergo frequent cardiac evaluations to detect early signs of disease-penetrance. While conventional echocardiographic TFC lack sensitivity for detection of early disease substrates [29,31], this study supports the use of deformation imaging as a robust follow-up method for AC patients in the out-patient department. Our data showed structural progression in all investigated age-groups, including early presenters (age < 30 years at baseline) and late presenters (age > 50 years at baseline). These findings do not support age-tailoring of cardiac imaging follow-up intervals at the out-patient department. However, since other studies reported low risks of SCD in older relatives, structural progression in this group may be of limited value compared to younger relatives. Future studies with long follow-up of a large cohort of patients >50 years are needed to determine the relation between structural progression and risk of SCD in this group.

The patient-specific computational model supported deformation imaging findings and enabled a link between deformation abnormalities and local tissue substrates. Future studies could investigate the predictive value of the estimated tissue properties and test whether inclusion of more information on the patients' haemodynamic state is essential.

Limitations

Since we excluded patients with overt structural disease at baseline, our cohort had a lower event rate than the average AC cohort. This resulted in a group of only 6 patients who experienced a life-threatening VA during follow-up, which is too small to search for risk factors in deformation imaging or estimated tissue properties on a group level.

Due to the high prevalence of patients with mutations in the PKP2 gene, the generalizability to patient populations with other dominating mutations is uncertain.

Conclusion

This study showed that deformation imaging can be used to follow-up disease progression in early AC. Patient-specific computer simulations showed the development of a tissue substrate affecting contractility, compliance, and activation delay. Since structural progression was seen in all age-groups, age-tailoring of follow-up intervals for cardiac imaging is not supported by our data.

References

1. Thiene G, Nava A, Corrado D, Rossi L, Pennelli N. 1988 Right Ventricular Cardiomyopathy and Sudden Death in Young People. *N. Engl. J. Med.* **318**, 129–133. (doi:10.1056/NEJM198801213180301)
2. Basso C, Corrado D, Marcus FI et al. 2009 Arrhythmogenic right ventricular cardiomyopathy. *Lancet* , 1289–300.
3. Groeneweg JA et al. 2015 Clinical Presentation, Long-Term Follow-Up, and Outcomes of 1001 Arrhythmogenic Right Ventricular Dysplasia/Cardiomyopathy Patients and Family Members. *Circ. Cardiovasc. Genet.* **8**, 437–446. (doi:10.1161/CIRCGENETICS.114.001003)
4. Dalal D et al. 2005 Arrhythmogenic right ventricular dysplasia: A United States experience. *Circulation* (doi:10.1161/CIRCULATIONAHA.105.542266)
5. van der Pols MJ, Mast TP, Loh P, van der Heijden JF, Cramer MJ, Hauer RN, te Riele ASJM. 2016 Clinical characterisation and risk stratification of patients with arrhythmogenic right ventricular dysplasia/cardiomyopathy ≥50 years of age. *Netherlands Hear. J.* (doi:10.1007/s12471-016-0886-7)
6. Sen-chowdhry S, Syrris P, Ward D, Asimaki A, Sevdalis E, McKenna WJ. 2007 Clinical and Genetic Characterization of Families With Arrhythmogenic Right Ventricular Dysplasia / Cardiomyopathy Provides Novel Insights Into Patterns of Disease Expression. , 16–18. (doi:10.1161/CIRCULATIONAHA.106.660241)
7. Towbin JA et al. 2019 2019 HRS expert consensus statement on evaluation, risk stratification, and management of arrhythmogenic cardiomyopathy. *Hear. Rhythm* **16**, e301–e372. (doi:10.1016/j.hrthm.2019.05.007)
8. Marcus FI et al. 2010 Diagnosis of Arrhythmogenic Right Ventricular Cardiomyopathy/Dysplasia: Proposed Modification of the Task Force Criteria. *Eur. Heart J.* **31**, 806–814. (doi:10.1093/eurheartj/ehq025)
9. Teske AJ, Cox MGPJ, Te Riele ASJM, De Boeck BW, Doevendans PA, Hauer RNW, Cramer MJM. 2012 Early Detection of Regional Functional Abnormalities in Asymptomatic ARVD/C Gene Carriers. *J. Am. Soc. Echocardiogr.* **25**, 997–1006. (doi:10.1016/j.echo.2012.05.008)
10. Mast TP et al. 2016 Right Ventricular Imaging and Computer Simulation for Electromechanical Substrate Characterization in Arrhythmogenic Right Ventricular Cardiomyopathy. *J. Am. Coll. Cardiol.* **68**, 2185–2197. (doi:10.1016/j.jacc.2016.08.061)
11. Mast TP et al. 2019 The Prognostic Value of Right Ventricular Deformation Imaging in Early Arrhythmogenic Right Ventricular Cardiomyopathy. *JACC Cardiovasc. Imaging*, 14 March. **12**, 446–455. (doi:10.1016/j.jcmg.2018.01.012)
12. Leren IS, Saberniak J, Haland TF, Edvardsen T, Haugaa KH. 2017 Combination of ECG and Echocardiography for Identification of Arrhythmic Events in Early ARVC. *JACC Cardiovasc. Imaging* **10**, 503–513. (doi:10.1016/j.jcmg.2016.06.011)
13. Lie ØH, Rootwelt-Norberg C, Dejgaard LA, Leren IS, Stokke MK, Edvardsen T, Haugaa KH. 2018 Prediction of Life-Threatening Ventricular Arrhythmia in Patients With Arrhythmogenic Cardiomyopathy: A Primary Prevention Cohort Study. *JACC Cardiovasc. Imaging* **11**, 1377–1386. (doi:10.1016/j.jcmg.2018.05.017)
14. Voigt JU et al. 2015 Definitions for a common standard for 2D speckle tracking echocardiography: consensus document of the EACVI/ASE/Industry Task Force to standardize deformation imaging. *Eur. Heart J. Cardiovasc. Imaging* **16**, 1–11. (doi:10.1093/ehjci/jeu184)
15. Malik N et al. 2020 Right ventricular strain predicts structural disease progression in patients with arrhythmogenic right ventricular cardiomyopathy. *J. Am. Heart Assoc.* **9**, 1–9. (doi:10.1161/JAHA.119.015016)
16. Chivulescu M, Lie ØH, Popescu BA, Skulstad H, Edvardsen T, Jurcut RO, Haugaa KH. 2019 High penetrance and similar disease progression in probands and in family members with arrhythmogenic cardiomyopathy. *Eur. Heart J.* , 1–10. (doi:10.1093/eurheartj/ehz570)
17. Rootwelt-Norberg C et al. 2021 Sex differences in disease progression and arrhythmic risk in patients with arrhythmogenic cardiomyopathy. *Europace* (doi:10.1093/europace/euab077)
18. Badano LP et al. 2018 Standardization of left atrial, right ventricular, and right atrial deformation imaging using two-dimensional speckle tracking echocardiography: A consensus document of the EACVI/ASE/Industry Task Force to standardize deformation imaging. *Eur. Heart J. Cardiovasc. Imaging* **19**, 591–600. (doi:10.1093/ehjci/jey042)
19. Mast TP et al. 2016 Prolonged Electromechanical Interval Unmasks Arrhythmogenic Right Ventricular Dysplasia/Cardiomyopathy in the Subclinical Stage. *J. Cardiovasc. Electrophysiol.* **27**, 303–314. (doi:10.1111/jce.12882)

20. Teske AJ, Cox MG, De Boeck BW, Doevendans PA, Hauer RN, Cramer MJ. 2009 Echocardiographic Tissue Deformation Imaging Quantifies Abnormal Regional Right Ventricular Function in Arrhythmogenic Right Ventricular Dysplasia/Cardiomyopathy. *J. Am. Soc. Echocardiogr.* **22**, 920–927. (doi:10.1016/j.echo.2009.05.014)
21. Kirkels FP, Lie ØH, Cramer MJ, Chivulescu M, Rootwelt-Norberg C, Asselbergs FW, Teske AJ, Haugaa KH. 2021 Right Ventricular Functional Abnormalities in Arrhythmogenic Cardiomyopathy. *JACC Cardiovasc. Imaging* (doi:10.1016/j.jcmg.2020.12.028)
22. T A, T D, P B, X V, Fw P. 2005 The CircAdapt model. *Am. J. Physiol. Circ. Physiol.*
23. Walmsley J, Arts T, Derval N, Bordachar P, Cochet H, Ploux S, Prinzen FW, Delhaas T, Lumens J. 2015 Fast Simulation of Mechanical Heterogeneity in the Electrically Asynchronous Heart Using the MultiPatch Module. *PLoS Comput. Biol.* **11**, 1–23. (doi:10.1371/journal.pcbi.1004284)
24. Lumens J, Delhaas T, Kirn B, Arts T. 2009 Three-wall segment (TriSeg) model describing mechanics and hemodynamics of ventricular interaction. *Ann. Biomed. Eng.* **37**, 2234–2255. (doi:10.1007/s10439-009-9774-2)
25. Osta N van *et al.* 2021 Uncertainty Quantification of Regional Cardiac Tissue Properties in Arrhythmogenic Cardiomyopathy Using Adaptive Multiple Importance Sampling. *Front. Physiol.*
26. Bauce B *et al.* 2011 Clinical phenotype and diagnosis of arrhythmogenic right ventricular cardiomyopathy in pediatric patients carrying desmosomal gene mutations. *Heart. Rhythm* **8**, 1686–1695. (doi:10.1016/j.hrthm.2011.06.026)
27. Te Riele ASJM *et al.* 2015 Arrhythmogenic Right Ventricular Dysplasia/Cardiomyopathy in the Pediatric Population Clinical Characterization and Comparison with Adult-Onset Disease. *JACC Clin. Electrophysiol.* **1**, 551–560. (doi:10.1016/j.jacep.2015.08.004)
28. Charron P *et al.* 2010 Genetic counselling and testing in cardiomyopathies: A position statement of the European Society of Cardiology Working Group on Myocardial and Pericardial Diseases. *Eur. Heart J.* **31**, 2715–2728. (doi:10.1093/eurheartj/ehq271)
29. Te Riele ASJM *et al.* 2014 Yield of serial evaluation in at-risk family members of patients with ARVD/C. *J. Am. Coll. Cardiol.* **64**, 293–301. (doi:10.1016/j.jacc.2014.04.044)
30. Bosman LP *et al.* 2020 Diagnosing arrhythmogenic right ventricular cardiomyopathy by 2010 task force criteria: Clinical performance and simplified practical implementation. *Europace* **22**, 787–796. (doi:10.1093/europace/euaa039)
31. Kirkels FP, Bosman LP, Taha K, Cramer MJ, van der Heijden JF, Hauer RNW, Asselbergs FW, te Riele ASJM, Teske AJ. 2021 Improving Diagnostic Value of Echocardiography in Arrhythmogenic Right Ventricular Cardiomyopathy Using Deformation Imaging. *JACC Cardiovasc. Imaging* (doi:10.1016/j.jcmg.2021.07.002)
32. Taha K, Mast TP, Cramer MJ, van der Heijden JF, Asselbergs FW, Doevendans PA TA. 2019 Evaluation of Disease Progression in Arrhythmogenic Cardiomyopathy: The Change of Echocardiographic Deformation Characteristics Over Time. *JACC Cardiovasc Imaging*
33. Te Riele ASJM *et al.* 2013 Mutation-positive arrhythmogenic right ventricular dysplasia/ cardiomyopathy: The triangle of dysplasia displaced. *J. Cardiovasc. Electrophysiol.* **24**, 1311–1320. (doi:10.1111/jce.12222)
34. Basso C, Thiene G. 2007 Arrhythmogenic right ventricular cardiomyopathy/dysplasia. In *Orphanet Journal of Rare Diseases* (eds F Marcus, A Nava, G Thiene), pp. 29–44. (doi:10.1186/1750-1172-2-45)
35. Basso C, Burke M, Fornes P, Gallagher PJ, De Gouveia RH, Sheppard M, Thiene G, Van Der Wal A. 2008 Guidelines for autopsy investigation of sudden cardiac death. *Virchows Arch.* **452**, 11–18. (doi:10.1007/s00428-007-0505-5)
36. Van Osta N *et al.* 2020 Parameter subset reduction for patient-specific modelling of arrhythmogenic cardiomyopathy-related mutation carriers in the CircAdapt model: Parameter Subset Reduction. *Philos. Trans. R. Soc. A Math. Phys. Eng. Sci.* **378**, 20190347. (doi:10.1098/rsta.2019.0347)
37. Van Osta N, Kirkels F, Lyon A, Koopsen T, Van Loon T, Cramer M-J, Teske AJ, Delhaas T, Lumens J. In press. Electromechanical substrate characterization in arrhythmogenic cardiomyopathy using imaging-based patient-specific computer simulations. (doi:10.1093/europace/euaa407)

Supplementary Material

Supplemental Table S6.1. Values at inclusion and last follow-up are mean (SD). Yearly progression rate with standard errors. P-values for progression are calculated by linear mixed model statistics with exchangeable covariance structure and random intercept.

	At inclusion (n=82) (SD)	Progression rate, 1 year (SE)	At last follow-up (n=82) (SD)	p-value for progression
LVEF, %	58.52 (4.40)	-0.03 (0.06)	58.83 (4.15)	0.603
Age 0-30	59.22 (3.60)	-0.11 (0.09)	58.44 (4.15)	0.201
Age 30-50	57.97 (3.96)	0.02 (0.10)	58.97 (3.84)	0.835
Age 50+	58.48 (5.73)	-0.07 (0.18)	59.09 (4.70)	0.699
LV GLS, %, n=313	-20.08 (1.93)	0.10 (0.02)	-19.58 (2.10)	<0.001
Age 0-30, n=108	-20.11 (1.79)	0.10 (0.04)	-19.56 (2.34)	0.012
Age 30-50, n=132	-20.02 (2.09)	0.08 (0.04)	-19.55 (1.81)	0.023
Age 50+, n=73	-20.14 (1.95)	0.15 (0.06)	-19.66 (2.25)	0.022
RV _{FW} LS, %	-25.33 (6.05)	0.58 (0.06)	-21.50 (5.91)	<0.001
Age 0-30	-25.56 (5.78)	0.43 (0.10)	-22.22 (5.35)	<0.001
Age 30-50	-25.59 (6.00)	0.65 (0.10)	-21.09 (6.52)	<0.001
Age 50+	-24.71 (6.64)	0.70 (0.13)	-21.22 (5.82)	<0.001
Peak systolic strain base	-22.78 (7.51)	0.71 (0.06)	-17.40 (6.52)	<0.001
Age 0-30	-23.21 (7.57)	0.67 (0.11)	-17.81 (6.63)	<0.001
Age 30-50	-23.00 (7.60)	0.70 (0.10)	-17.23 (6.91)	<0.001
Age 50+	-21.97 (7.57)	0.84 (0.13)	-17.16 (6.08)	<0.001
Peak systolic strain mid	-25.76 (6.26)	0.58 (0.07)	-21.84 (6.09)	<0.001
Age 0-30	-25.95 (5.97)	0.41 (0.10)	-22.59 (5.55)	<0.001
Age 30-50	-26.17 (6.17)	0.67 (0.10)	-21.59 (6.59)	<0.001
Age 50+	-24.96 (6.91)	0.72 (0.14)	-21.31 (6.15)	<0.001
Peak systolic strain apex	-27.54 (5.89)	0.43 (0.08)	-25.42 (6.01)	<0.001
Age 0-30	-27.55 (4.89)	0.19 (0.12)	-26.38 (4.57)	0.105
Age 30-50	-27.70 (6.02)	0.56 (0.12)	-24.72 (6.89)	<0.001
Age 50+	-27.30 (6.95)	0.59 (0.18)	-25.27 (6.30)	0.001
Onset base (ms)	96.00 (56.40)	4.1 (0.7)	122.38 (55.25)	<0.001
Age 0-30	94.22 (63.93)	4.4 (1.2)	119.11 (62.51)	<0.001
Age 30-50	96.03 (58.51)	3.4 (1.0)	121.81 (54.11)	0.001
Age 50+	98.04 (45.26)	5.6 (1.3)	127.00 (49.58)	<0.001
Onset mid (ms)	69.17 (46.55)	3.3 (0.7)	87.29 (49.51)	<0.001
Age 0-30	55.78 (42.60)	3.7 (1.0)	83.70 (44.23)	<0.001
Age 30-50	72.94 (53.75)	3.0 (1.1)	88.62 (54.91)	0.007
Age 50+	79.65 (37.52)	3.7 (1.4)	89.65 (49.41)	0.009
Onset apex (ms)	58.28 (35.58)	2.1 (0.6)	72.94 (40.51)	<0.001
Age 0-30	50.78 (35.04)	2.2 (1.0)	66.93 (37.93)	0.027
Age 30-50	56.56 (36.01)	1.9 (0.9)	75.69 (46.60)	0.030
Age 50+	69.48 (34.34)	2.5 (1.2)	76.17 (34.87)	0.038
Post-syst. shortening base	7.87 (15.39)	0.76 (0.17)	11.62 (18.90)	<0.001
Age 0-30	5.67 (17.46)	0.60 (0.25)	11.03 (20.42)	0.016
Age 30-50	9.01 (15.41)	1.10 (0.27)	14.35 (20.60)	<0.001
Age 50+	8.88 (12.96)	0.07 (0.38)	8.52 (14.23)	0.856

Supplemental Table S6.1. (continued)

	At inclusion (n=82) (SD)	Progression rate, 1 year (SE)	At last follow-up (n=82) (SD)	p-value for progression
Post-syst. shortening mid	2.05 (5.29)	0.45 (0.12)	4.38 (12.66)	<0.001
Age 0-30	1.38 (5.20)	0.09 (0.10)	2.24 (4.15)	0.371
Age 30-50	2.10 (4.82)	0.85 (0.23)	7.15 (18.58)	<0.001
Age 50+	2.78 (6.09)	0.13 (0.23)	3.04 (8.06)	0.580
Post-syst. shortening apex	0.50 (1.17)	0.34 (0.07)	2.23 (7.15)	<0.001
Age 0-30	0.39 (0.76)	0.02 (0.03)	0.57 (1.48)	0.617
Age 30-50	0.68 (1.38)	0.63 (0.14)	4.30 (10.35)	<0.001
Age 50+	0.36 (1.27)	0.22 (0.12)	1.31 (4.92)	0.054

LVEF, left ventricular ejection fraction; LV GLS, left ventricular global longitudinal strain; RV_{FWLS}, right ventricular free wall longitudinal strain.

Supplemental Table S6.2. Values at inclusion and last follow-up are mean (SD). Yearly progression rate with standard errors. P-values for progression are calculated by linear mixed model statistics with exchangeable covariance structure and random intercept.

	At inclusion (n=82) (SD)	Progression rate, 1 year (SE)	At last follow-up (n=82) p-value for progression	p-value for progression
Contractility base, MPa/s	455.116 (132.925)	-5.473 (1.687)	422.837 (136.938)	0.001
Age 0-30	449.171 (119.957)	-7.409 (2.652)	412.581 (135.470)	0.005
Age 30-50	481.458 (146.787)	-5.825 (1.933)	434.399 (154.782)	0.022
Age 50+	425.445 (125.355)	-7.58 (4.154)	418.789 (115.124)	0.855
Contractility mid, MPa/s	480.433 (117.575)	-1538 (1446)	474.570 (113.836)	0.288
Age 0-30	471.521 (106.577)	-1448 (2245)	474.260 (106.125)	0.436
Age 30-50	509.287 (115.090)	-3517 (2238)	486.931 (130.727)	0.116
Age 50+	450.751 (128.761)	4304 (3339)	457.735 (99.002)	0.197
Contractility apex, MPa/s	467.850 (118.692)	-2.362 (1.515)	459.076 (118.832)	0.119
Age 0-30	472.776 (113.608)	-3.794 (2.307)	457.487 (106.345)	0.100
Age 30-50	481.884 (122.978)	-3.536 (2.398)	470.409 (140.351)	0.140
Age 50+	442.541 (119.662)	3.730 (3.407)	445.174 (102.358)	0.274
Compliance base, 1/kPa	1.24e-05 (1.12e-05)	1.04e-06 (5.16e-07)	2.20e-05 (5.37e-05)	0.044
Age 0-30	1.09e-05 (9.18e-06)	2.43e-07 (2.75e-07)	1.41e-05 (1.38e-05)	0.377
Age 30-50	1.38e-05 (1.38e-05)	1.45e-06 (5.29e-07)	1.58e-05 (1.76e-05)	0.006
Age 50+	1.23e-05 (9.25e-06)	2.49e-06 (2.33e-06)	3.98e-05 (9.75e-05)	0.285
Compliance mid, 1/kPa	1.87e-05 (1.73e-05)	1.17e-06 (6.28e-07)	3.26e-05 (6.66e-05)	0.062
Age 0-30	1.38e-05 (1.05e-05)	4.75e-07 (4.06e-07)	2.14e-05 (2.23e-05)	0.242
Age 30-50	2.02e-05 (1.62e-05)	5.88e-07 (6.22e-07)	2.43e-05 (3.02e-05)	0.345
Age 50+	2.25e-05 (2.36e-05)	5.86e-06 (2.77e-06)	5.73e-05 (1.16e-04)	0.035
Compliance apex, 1/kPa	2.61e-05 (2.42e-05)	3.12e-06 (7.26e-07)	5.58e-05 (6.18e-05)	<0.001
Age 0-30	1.89e-05 (1.91e-05)	2.41e-06 (7.55e-07)	4.62e-05 (4.05e-05)	0.001
Age 30-50	3.07e-05 (2.65e-05)	3.18e-06 (7.26e-07)	5.64e-05 (7.14e-05)	0.008
Age 50+	2.82e-05 (2.50e-05)	4.43e-06 (2.07e-06)	6.62e-05 (6.84e-05)	0.032
Activation delay base, ms	83.61 (63.77)	1.2 (0.9)	85.82 (69.53)	0.156
Age 0-30	72.81 (53.30)	1.6 (1.4)	94.74 (85.20)	0.250
Age 30-50	94.77 (68.58)	0.5 (1.2)	87.76 (60.99)	0.659
Age 50+	80.75 (68.22)	2.1 (2.2)	72.67 (60.79)	0.355

Supplemental Table S6.2. (continued)

	At inclusion (n=82) (SD)	Progression rate, 1 year (SE)	At last follow-up (n=82) p-value for progression	p-value for progression
Activation delay mid, ms	75.42 (47.40)	1.3 (0.7)	78.34 (55.22)	0.049
Age 0-30	72.06 (39.56)	0.7 (0.9)	80.09 (44.46)	0.458
Age 30-50	78.90 (45.13)	1.8 (1.1)	85.81 (64.55)	0.105
Age 50+	74.53 (59.32)	0.6 (1.5)	65.89 (52.67)	0.718
Activation delay apex, ms	70.70 (44.28)	0.7 (0.6)	68.26 (45.21)	0.251
Age 0-30	70.79 (35.54)	-0.1 (0.9)	70.74 (40.15)	0.899
Age 30-50	70.80 (42.20)	1.1 (0.9)	72.76 (46.59)	0.212
Age 50+	70.45 (56.72)	0.4 (1.5)	59.08 (49.35)	0.780
Work density base, kPa	4437.11 (1518.13)	-18.6 (18.7)	4349.26 (1790.30)	0.321
Age 0-30	4155.70 (1290.09)	-55.9 (25.9)	3975.06 (1363.42)	0.031
Age 30-50	4709.47 (1734.44)	5.2 (31.2)	4619.96 (2195.16)	0.867
Age 50+	4388.53 (1439.48)	-7.4 (42.0)	4411.89 (1591.03)	0.860
Work density mid, kPa	4760.22 (1477.71)	-6.5 (13.8)	4807.39 (1729.39)	0.637
Age 0-30	4459.76 (1197.44)	-9.4 (19.8)	4549.55 (1388.68)	0.635
Age 30-50	5106.32 (1663.42)	-15.4 (22.7)	5083.16 (2190.07)	0.498
Age 50+	4631.40 (1464.22)	25.6 (31.0)	4726.39 (1332.26)	0.410
Work density apex, kPa	4859.82 (1747.30)	-0.2 (19.6)	5122.76 (1994.36)	0.992
Age 0-30	4642.50 (1353.06)	2.7 (25.6)	4892.43 (1780.15)	0.916
Age 30-50	5113.13 (2038.61)	-26.3 (33.8)	5317.75 (2392.85)	0.436
Age 50+	4762.51 (1749.26)	75.4 (42.1)	5121.85 (1646.44)	0.073

Supplemental Table S6.3. Normalized heterogeneity between three RV free wall segments at inclusion and last follow-up are mean (SD). Yearly progression rate with standard errors. P-values for progression are calculated by linear mixed model statistics with exchangeable covariance structure and random intercept.

	At inclusion (n=82)	Progression rate, 1 year (SE)	At last follow-up (n=82)	p-value for progression
Normalized Contractility, %	10.99 (5.94)	0.46 (0.11)	13.26 (9.95)	<0.001
Age 0-30	10.67 (7.02)	0.51 (0.14)	13.68 (11.12)	<0.001
Age 30-50	10.63 (5.25)	0.47 (0.18)	13.98 (10.97)	0.008
Age 50+	11.86 (5.61)	0.38 (0.31)	11.78 (6.75)	0.220
Normalized Compliance, %	44.84 (16.69)	1.07 (0.27)	55.53 (18.18)	<0.001
Age 0-30	43.10 (13.23)	1.53 (0.39)	56.33 (18.12)	<0.001
Age 30-50	46.94 (19.27)	0.55 (0.42)	52.96 (16.63)	0.187
Age 50+	43.96 (16.86)	1.69 (0.73)	58.19 (20.53)	0.020
Normalized Work Density, %	12.44 (8.57)	1.07 (0.23)	17.47 (17.80)	<0.001
Age 0-30	11.22 (5.89)	0.80	16.75 (14.91)	0.001
Age 30-50	13.52 (11.42)	1.27	19.59 (23.15)	<0.001
Age 50+	12.35 (6.50)	1.71	15.36 (11.69)	0.032
Activation delay, ms	16.40 (16.56)	0.80 (0.25)	19.92 (19.51)	<0.001
Age 0-30	14.99 (11.24)	0.81 (0.40)	21.20 (29.58)	0.044
Age 30-50	18.11 (24.09)	0.71 (0.38)	20.16 (14.65)	0.057
Age 50+	15.67 (6.00)	1.10 (0.57)	18.09 (7.65)	0.052

7



General Discussion



General Discussion

The aim of this Thesis was to get more insight in the myocardial disease substrates observed in early-stage Arrhythmogenic Cardiomyopathy (AC) patients. To do so, we developed a modelling framework for patient-specific estimation of model parameters representing regional myocardial tissue properties. This modelling framework used the CircAdapt model of the human heart and circulation [1,2] as engine and clinically measured regional deformation patterns as input.

In **Chapter 2**, we developed a simple protocol in which right ventricular (RV) model parameters were estimated with a gradient-based parameter estimation protocol, minimizing the error between measured and simulated strain indices. Main findings were 1) that the CircAdapt model can reproduce deformation patterns, 2) that more information on LV deformation should be included to enable a more reliable description of the RV afterload, and 3) a more robust parameter optimization algorithm should be used in order to cope with the non-linear parameter space.

Using this knowledge, we performed an extensive sensitivity and identifiability analysis in **Chapter 3** to identify the most important parameters to simulate both LV and regional RV deformation patterns using our model. Over hundred model parameters were identified. Based on the sensitivity analysis performed with the Morris screening method [3] and identifiability analysis based on the diaphony obtained from Monte Carlo simulations [4], the parameter set was reduced to a smaller subset containing 23 parameters. Most important parameters related to active and passive stress development and, hence, contractility and passive stiffness of the myocardium. Making additional assumptions, we combined three parameters into one which reduced the parameter subset to the final 21 parameters used in the following chapters. In **Chapter 4**, we used this parameter subset to estimate patient-specific model parameters in a large cohort of 68 individuals with a desmosomal mutation related to AC. These estimations showed that abnormal deformation patterns in AC patients were related to increased heterogeneity in tissue contractility and compliance.

To get more insight in the development of the myocardial tissue substrate underlying abnormal deformation patterns in early-stage AC patients, we studied a cohort in **Chapters 5 and 6** at baseline and during follow-up. As measurement uncertainty inevitably affects the model estimation, uncertainty might affect the results in a longitudinal study design more than in the previous chapters describing cross-sectional data. To include measurement uncertainty in the framework, we implemented a Bayesian inference method in **Chapter 5** to estimate the posterior distributions rather than a single point estimate. Using this method, we were able to estimate the reliability of the estimation.

In **Chapter 6**, this method was applied to longitudinal follow-up data obtained in a large cohort of 82 subjects without structural abnormalities defined by the Task Force Criteria (TFC) and the age-related prevalence of AC progression was investigated. It was shown that AC-related evolution of deformation abnormalities and related heterogeneity of RV tissue properties occurs independent from age.

In this final chapter, we discuss the current state of the creation of the Digital Twin of early-stage AC patients. First, we discuss the novel insight in AC tissue characterization using the Digital Twin, which mainly focusses on the research presented in **Chapters 4** and **6**. Then, we discuss how the main findings of these chapters depend on the choices made in **Chapters 2, 3, and 5**. Also, we hypothesize which technological advancements might improve the quality of our modelling framework. Finally, we discuss the impact of the research presented in this Thesis and frame the potential for clinical translation of the Digital Twin technology. In this Thesis, we have addressed the six challenges introduced in **Chapter 1** (Figure 7.1), which were *the Problem Challenge, the Measurement Challenge, the Model Challenge, the Parameter Challenge, the Optimization Challenge, and the Translational Challenge*.

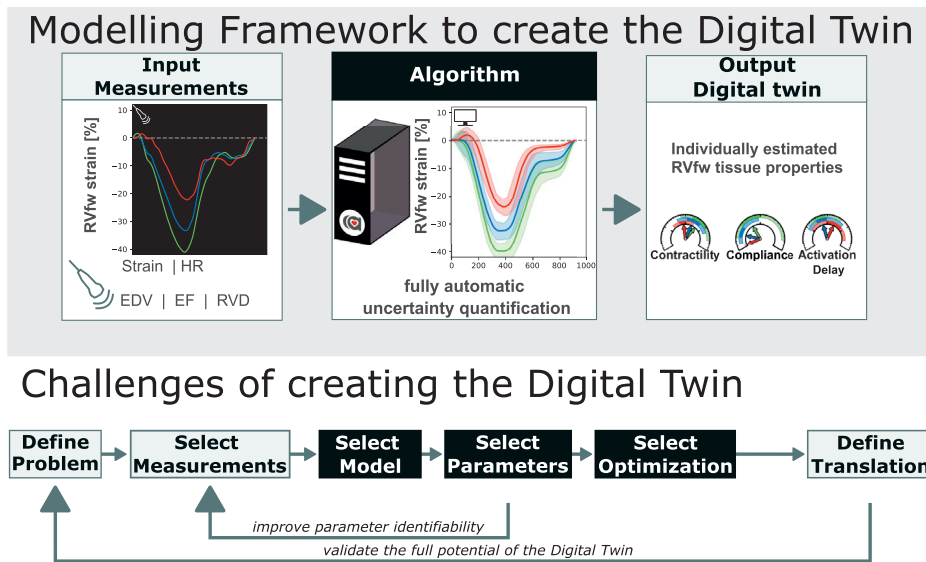


Figure 7.1 Modelling framework (top) and challenges of (bottom) creating a Digital Twin. The identified challenges are related to different aspects of the modelling framework. The lower two arrows indicate the most important dependencies as discussed in this chapter.

Using the Digital Twin – Novel insights in Arrhythmogenic Cardiomyopathy tissue characterization

The role of the Digital Twins has gained impact in clinics. The first Digital twins are being used for diagnosis [5], stratification [6], and intervention planning [7,8]. The Digital Twin can be used to get more insight in the myocardial tissue substrate underlying the abnormal deformation patterns (**Chapter 4**). Better understanding of the substrate is important because the lack of diagnostic tools to diagnose early-disease stages [9]. Patients with AC may receive treatments like lifestyle changes, anti-arrhythmic drugs, ablation, and ICD implantation [10] which all have a high impact on quality of the patient's life. Therefore, reliable risk stratification is important in early-stage or preclinical AC, as these subjects may experience sudden cardiac death as first symptom [11,12]. The 2010 TFC [13] and guidelines [10,14] have been developed to guide the diagnosis and risk stratification of AC. In this Thesis, we have followed the 2010 TFC to distinguish between subclinical subjects, patients with only electrical, and patients with both electrical and structural abnormalities (**Chapters 2, 3, and 4**). After the publication of the 2010 TFC, various evaluations of the current diagnostic criteria and differential diagnosis have been performed [15–18] and updated consensus statements and guidelines have been published [10,14]. The prognostic value of regional deformation abnormalities has been demonstrated [19–22] and this Thesis emphasizes the value of deformation imaging.

In this thesis, we applied the modelling framework to two cohorts which were both described elsewhere [9,23,24]. These studies focussed on the development of deformation characteristics and its predictive value. Therefore, deformation patterns were available for most subjects. Because studies in this Thesis were performed in retrospect, the availability of other clinical data was limited. As a result, voluminal information obtained from cardiac magnetic resonance imaging (CMR) was used in **Chapters 2, 3, and 4** while echocardiographic voluminal information was used in **Chapters 5 and 6**. This may affect the model estimations, as these two sources have a systematic difference in voluminal measurements [25]. The effect of the different measurements on the outcome of the Digital Twin should be investigated and the results of this should be included in the design of a prospective study. As the systematic difference between echocardiographic and CMR data only holds for global estimations, we assume regional heterogeneities are marginally affected by this measurement uncertainty.

In line with previously published hypotheses based on generic simulations [9], most of our patient-specific simulations revealed heterogeneity in contractility and compliance rather than activation delay as main cause of the tissue deformation abnormalities observed in AC subjects. Estimated tissue properties in the basal segment of the RV

were most abnormal, which is in line with typical expression of the disease [9,19,26,27]. The decreased contractility and compliance in the basal segment may be directly related to fibro-fatty replacement of myocardial tissue [28,29]. Our findings emphasize the high clinical value of deformation patterns because they reveal heterogeneity in tissue properties (**Chapter 4**). By expanding and improving our modelling framework, the estimated Digital Twin might be used in the future to aid diagnosis and to improve risk stratification.

Despite the abnormal electrical activation patterns that may be observed in AC patients [30], only abnormal activation delay was observed on an individual level (**Chapter 4**). Late activated basal segments are not expected to significantly affect pump function, as their contractile function was in most cases severely reduced. Although not histologically validated, it is likely that abnormal tissue properties are caused by fibro-fatty tissue replacement. Late activated segments infiltrated with fibro-fatty tissue can be a substrate for arrhythmias [31]. Only little arrhythmic events were reported in the study cohort used in **Chapter 6**. In future studies, applying this method on a larger cohort with a higher number of arrhythmic events could show whether this modelling framework can add value to current arrhythmic risk prediction models.

Creating the Digital Twin – The Modelling Framework

Garbage in, Garbage out

The quality of the Digital Twin is heavily influenced by the quality of the measurements. The deformation patterns obtained from echocardiography are easy to obtain and more accessible than those obtained with CMR. Automatic segmentation of the wall can standardize deformation imaging and thereby improve its accuracy and reproducibility [32]. The downside of echocardiography is its sensitivity to noise and artifacts [33]. The framework developed in this Thesis is developed using patient data of relatively good quality (**Chapter 3** and **5**). Datasets with artifacts were removed from the cohort studies (**Chapter 4** and **6**). Therefore, the effect of artifacts on the estimation of the Digital Twin is unknown. Noise was included as measurement uncertainty in **Chapter 5** and **6**, however, this was limited to uncertainty of the offline analysis. Future work should further investigate which amount and type of noise and artifacts are acceptable. Given the general principle of “Garbage in, garbage out”, it is crucially important to define what level of measurement uncertainty is acceptable when creating Digital Twins.

Despite all sources of uncertainty present in echocardiographic deformation patterns, it has been demonstrated that deformation patterns have predictive value in AC patients [20,34]. Therefore, we aimed to combine these patterns with a physics- and physiology-

based computational model to obtain more information than from the patterns alone. In **Chapter 3**, we selected the model parameters essential to reproduce regional deformation patterns. Further reduction of the parameter subset resulted in an increase in model discrepancy, meaning these parameters form the basis for the myocardial tissue substrate possibly found in the Digital Twin. We have limited the amount of clinical information used for creating the Digital Twin to the data available in these large cohorts due to the retrospective nature of the study. **Chapter 6** demonstrates that the current set of measurements is not sufficient, as wide posterior distributions are estimated. Rather than only addressing the research question “What is the tissue substrate underlying the clinical data?” in the sensitivity analysis (Parameter Challenge), the research question “In which clinical data is the tissue substrate expressed?” should be addressed as well (Measurement Challenge). These two questions form a recursive search to the optimal combination of clinical data and model parameters to create the best Digital Twin of AC patients (Figure 7.1), given the research question being addressed.

In **Chapters 4, 5, and 6**, we found that derived tissue properties are estimated more accurately than properties explicitly represented by model parameters given the available clinical data. More research should be done on which estimated tissue properties have clinical value. The estimated tissue properties should be interpreted as a pseudo-true value related to real tissue properties which may have clinical value. To use the Digital Twin to estimate the absolute values of tissue properties (Translational Challenge), estimated results should be validated with real-world data. This change in clinical translation should be followed by a re-formulation of the problem (Problem Challenge) which affects the choice of measurements, model, and model parameters identified. All challenges should be re-addressed to be able to estimate the absolute values of tissue properties.

Estimation of pump function

The main function of the heart is to pump blood through the body to meet the body’s demands. The amount of pumped blood is quantified by Stroke Volume or Cardiac Output, which in the CircAdapt model is controlled by the pressure-flow control which contains two parameters describing heart rate and time-averaged venous return [1]. In our sensitivity analysis (**Chapter 3**), these two parameters seemed to be most sensitive to deformation indices. Therefore, reliable measurements of cardiac output and stroke volume are important. This important input information was limitedly available in the cohort studies used in this thesis (**Chapters 4 and 6**). Future studies should prospectively include more clinical data on ventricular cavity and wall volumes.

In **Chapter 3**, we showed that the mean aortic pressure is not identifiable given the available data. This parameter was removed from the subset, and set to its default value of 92mmHg. Thereby, global pump function in terms of work is mostly affected by

cardiac output. It is only minimally affected by diastolic pressure, as simulations with high diastolic pressure were assumed to be not physiological and thus rejected so most model parameters are related to the distribution of load over the wall segments. As only voluminal information is included in the estimation of pump function, pump function was not reliably estimated. Because the total pump work is the sum of local myocardial work [35], the absolute values of the derived tissue properties are not reliable and only heterogeneity in tissue properties can be used for clinical translation. To improve the reliability, target tissue properties should be prospectively included in the problem definition such that measurements and model parameter selection can be dedicated to these model outcomes (Figure 7.1).

Increasing model detail and additional measurements can improve the accuracy of the Digital Twin

In **Chapter 5**, we observed not all parameters were identifiable. As the model parameter subset cannot be further reduced because model discrepancy will increase, the model could be changed (Model Challenge) or measurements can be added to the set (Measurement Challenge). Adding measurements to the modelling framework will change the dynamics of the estimation as more information is available to estimate the posterior parameter values. As this is limited to those signals the chosen model is able to reproduce, the choice of model must be re-evaluated. Currently, two modules exist which allows to increase the level of detail in the CircAdapt model without significantly increase the computational cost. First, a 1D wave propagation model has been developed recently as a module for the circulation [36]. This module simulates arteries as a 1D model rather than lumped cavities. It also includes the backward propagation of waves, and has been used to describe cardiovascular fetal to neonatal transition [37]. Using this module, afterload of the heart is modelled more realistically.

Second, myocardial active behaviour could be modelled using a electrophysiological model rather than a phenomenological model. Recently, Lyon et al. developed an electromechanical cardiomyocyte model [38], which combines the O'Hara-Rudy dynamic model describing cellular electrophysiology and Calcium cycling [39] with the MechChem model describing contraction of the sarcomere and tension development [40,41]. This novel cardiomyocyte model could be implemented in the CircAdapt model as a module to replace the currently used phenomenological description for active stress (Equation 2.2). This module might be able to reproduce the cellular abnormalities found in mice models [42] while implemented in a whole-heart haemodynamic circulation. If so, it may further increase accuracy of the Digital Twin and its value for clinical translation.

When these modules are simulated in the CircAdapt model, tissue mechanics and cavity haemodynamics will still be simulated using the one-fibre and TriSeg modules [1,2], respectively. The geometric and structural simplicity of these modules is essential to create a fast and reliable computational model of cardiac mechanics and haemodynamics, but might limit the measurements that are possible to simulate. It could be considered to replace the one-fibre and TriSeg modules by more complex mechanical finite element models (FEM) [43]. Because these models contain a more detailed description of the geometry, they might have a lower discrepancy with real-world data and therefore might improve the estimations. The spatial resolution, however, is more detailed compared to the clinical measurements used in this Thesis, which complicates the identifiability of the model parameters (Parameter Challenge).

Different parameters will be available when these suggestions are taken into account. Therefore, the parameter subset of interest should be reidentified (Parameter Challenge). With these new models, less parameters might be needed to reproduce clinical measurements which improves the identifiability of the model. Currently, only systolic part of strain is included in the likelihood function. We did not include diastolic strain because of the higher uncertainty due to drift compensation [44]. Because diastolic strain reflects filling of the ventricle, it is likely to contain more information on the passive material behaviour. Future work is needed to investigate how to reliably include diastolic strain in the modelling framework.

As an alternative to diastolic strain, valvular flow velocity patterns can be used. As they are known to reflect pressure gradients between the cardiac cavities [45], they potentially contain valuable information which is not enclosed in strain patterns. This information may improve the identifiability of the current parameter subset. However, valvular flow velocities are dependent on both ventricular as well as atrial or arterial behaviour. Therefore, by re-evaluating the parameter subset (Parameter Challenge), atrial and arterial model parameters are likely to be sensitive and therefore should be considered. This may be a valuable extension of the modelling platform, especially because right atrial dilatation has been observed in AC patients [46].

The biggest overall challenge is to find a balance between low model discrepancy, high parameter identifiability, high accuracy, low computational cost, and easy implementation in clinical workflow. It might be tempting to keep adding measurements, adding model parameters, or increase model complexity to improve the quality of the Digital Twin to non-invasively estimate myocardial tissue and cardiac pump properties. Due to limited time available to provide all measurements and the need to quickly translate measurements into interpretable results for clinical decision support, the number of measurements needed for the Digital Twin should be limited. However, correctly designed modelling

frameworks can provide accurate pseudo-true estimations which might have similar or even better predictive values compared to the true properties. The downside of using pseudo-true estimates is that validation requires more complex studies compared to non-invasive computational estimates of real properties.

Computational cost of creating the Digital Twin

Because the CircAdapt model is a lumped parameter model, most model parameters cannot be measured directly. Therefore, we have focussed on creating a Digital Twin using methods for parameter inference. These techniques are computationally more expensive, as many model evaluations need to be done to estimate model parameters. Due to limitations in the likelihood definition, the parameter describing heart rate was directly set from the measurements. Especially using Adaptive Multiple Importance Sampling (**Chapter 5**), in which posterior model parameter distributions were estimated, it would have been better to estimate rather than set the heart rate to also include uncertainty of the heart rate. Future work is needed to investigate the error propagation originating from this mapping.

For the purpose of this Thesis, we have attempted to reduce computational cost by means of optimizing the implementation. The version of the CircAdapt model used in this Thesis was originally developed in MATLAB [47] and this version was used in **Chapter 2**. The computational cost is approximately 2 seconds per heartbeat in the reference state, depending on the machine. To reduce computational cost, we have implemented the model in C++ to be able to do an extensive sensitivity analysis in **Chapter 3**. In this implementation, one heart beat takes approximately 10 milliseconds in the reference state. Especially the sensitivity analysis in **Chapter 3** was intractable before, since one reduction step would have taken over 2 years rather than the 4 days. Therefore, this implementation was essential for the study designs used in this Thesis.

Challenge the Challenges

Given the multidisciplinary character of the technology, patient-specific modelling and the creation of the Digital Twin of a patient's heart has been approached from different angles, each giving rise to specific challenges [8,43,48,49]. We aimed to summarize these challenges into 6 main challenges (Figure 7.1). The inter-dependent nature of these challenges is well illustrated by the optimization protocol (Optimization Challenge) handling the general function $\mathbf{y} = \mathcal{M}(\boldsymbol{\theta})$, which suggests that Measurement Challenge (the measurements \mathbf{y}), Model Challenge (the computational model \mathcal{M}), and Parameter Challenge (the parameter subset $\boldsymbol{\theta}$) could be combined into one main challenge. This would be a more theoretical approach, whilst we determined the set of measurements

(Measurement Challenge) from the clinical perspective independent from the model. Most challenges identified by others can be considered sub-challenges or out of scope for this Thesis, such as the challenge considering the availability of high-quality datasets [50], the integration and accessibility of data with healthcare organizations caused by infrastructural, regulatory, and social reasons [48], or the decision upon boundary and initial conditions [8].

Impact

The estimated prevalence of AC is 1 in 1000 to 5000 [51,52]. Family screening of first-degree relatives of probands is an important for identifying those at risk for sudden cardiac death [11,12]. Currently, only 40% of family members are screened [12] due to a lack of adequate screening infrastructure and due to anxiety and distress associated with the personal experience of a life-threatening arrhythmia or a recent family bereavement from an inheritable cardiac condition [53,54]. For those who are screened and monitored, accurate risk stratification is essential to not burden the patient more than needed.

In this impact section, we hypothesize on the potential added value of the Digital Twin approach presented in this Thesis for early recognition of AC and for arrhythmic risk stratification.

Digital Twin as a tool to get more insight in physiology

Computational models are used to get insight in the working mechanisms of the heart, its diseases and their treatments. As demonstrated in this Thesis, they can be used to reveal functional information that can't be measured without injuring the patient, e.g. pressures, or can't be measured at all, e.g. myofibre stress [43]. Over the years, various types of models have been developed to investigate cardiac pathologies. In the recent decade, the Digital Twin approach is becoming more popular [48,55] and models are now personalized to reveal the (patho)physiology of one single patient rather than the cohort.

Although work in this thesis is limited to the development of a modelling framework to create a Digital Twin of early-stage AC patients, this platform can easily be extended to other pathologies. It has been shown that the CircAdapt model is able to reproduce clinical data for different pathologies, including pulmonary hypertension [56], valvulopathies [57], left bundle branch block [58], and heart failure [59]. These simulation studies aimed at getting more insight in the physiology of the population or predict responses in the population, and thereby shows the model could be personalized to these pathologies (Model Challenge). Creating the Digital Twin of patients in the population might reveal new insights in the variety of disease expression.

Digital Twin as a tool for teaching

To extend the application range of the comprehensive CircAdapt model from research to education, the interactive user-friendly CircAdapt Simulator has been developed as an environment that can be used by medical students with the aim to improve their understanding of cardiovascular haemodynamics and related physiology [60]. This tool is available as a free download from www.circadapt.org. It is implemented in the medical curriculum at Maastricht university to teach haemodynamics and cardiac mechanics in healthy physiology, in valvopathies, and in congenital heart diseases, and it has been adapted by other universities. The CircAdapt Simulator in the current version does not use the full potential of the model, as it is limited to global pressures, volumes, and flows limiting the tool to teach general pump function in (patho)physiology.

The computational framework developed in this Thesis could add opportunities to the CircAdapt Simulator tool. As the Digital Twin reveals more details on the complex physiology and pathophysiology of the individual patient and the differences between patients, cardiac pathologies can be simulated more accurately and realistically. When (regional) myocardial data are added to the visualizations in the CircAdapt Simulator, the tool could be used to teach the pathophysiology in many more pathologies.

Digital Twin as a tool for precision medicine and aid clinical decision

Precision medicine is becoming more popular and big steps have been made to improve disease diagnosis and management [61]. Precision medicine is data-science driven and often includes genomics to create subgroups to better prescribe treatment strategies [62]. Also in AC, genomics is included in the 2010 TFC and geno-positive subjects are likely to develop AC [13]. In the two cohorts studied in **Chapters 4** and **6**, the pathogenic plakophilin-2 mutation is dominant. Although these subjects are at high risk of developing AC, **Chapter 6** shows that early stage disease can be found in all age groups. In the future, the Digital Twin could aid precision medicine by better characterizing and quantifying the myocardial tissue substrate.

As computational models are maturing, the step to add value to the process of clinical decision taking becomes smaller. As shown in this Thesis, Digital Twins can reveal information currently not measurable. This information can be used in randomized clinical trials to quantify its predictive and differential value. Reduction of computational cost is essential to implement a computational framework as presented in this Thesis into clinical workflow. Different protocols have been proposed to do so, including machine learning approaches and model emulator approaches [51]. These approaches can be used to increase the speed of parameter inference or as a direct inverse of the computational model.

Digital Twin as a tool for in silico trials to partially guide and reduce animal experiments

The CircAdapt model has been used to generate hypotheses which can guide further trials [63,64]. These studies predicted the effect of a clinical device on a population level. By using Digital Twins rather than a generic simulations, a more realistic cohort could be created to improve the predictive value of these in silico trials. Outcome of these trials can generate hypotheses and thereby guide the design of real clinical trials and animal studies. The chance of a positive result from these will increase, reducing the amount of trials and animal studies needed.

The work presented in this thesis demonstrates how the Digital Twin can be used to get more insight in the myocardial tissue substrate without the direct use of animal experiments. Without this in silico approach, biopsy could give insight in the tissue substrate but is limited to endocardial tissue. It is highly invasive, has a risk on complications, and is likely to produce false negatives [65,66]. Autopsy generally only gives insight in later stage AC. Alternatively, animal studies can be used to get insight in the tissue substrate. Necropsy on sacrificed animals could reveal insight in the substrate which is not possible to get with non-invasive measurements [67]. The Digital Twin could be used to estimate tissue properties without the need to sacrifice animals, reducing animal burden.

Digital Twin as a tool for virtual diagnostics

Cardiac stress testing is a test used in the diagnosis of various pathologies [68]. Potentially diseased subjects are stressed to increase the loading of the heart to better reveal the substrate. Cardiac stress tests are not included in the diagnosis of AC [10,13], but it has been shown that present deformation abnormalities increase during stress-test [69]. As exercise is associated with disease progression [70,71], performing a cardiac stress test could be considered unethical. As alternative, an in silico cardiac stress test could be performed with the Digital Twin. This could be used to better estimate arrhythmic risk or disease progression as result of exercise.

The Digital Twin could also be used as a tool to guide the diagnosis path. For established pathologies, guidelines aid professionals to diagnose and develop treatment strategies according to the best available evidence [10]. However, for less established pathologies, the best diagnosis and treatment strategies are unknown. Using the model framework developed in **Chapter 5**, not only insight in the myocardial tissue substrates is obtained, also regular clinical measurements can be obtained. Given the available evidence at that time, the Digital Twin can provide information on possible diagnosis and which measurements should be considered to improve differential diagnosis. This may

reduce time spent in the hospital by the patient, which increases quality of life of the patient and reduces healthcare cost.

Conclusion

This Thesis presents a novel patient-specific modelling framework that enables non-invasive estimation of myocardial tissue properties in individual patients with Arrhythmogenic Cardiomyopathy (ACM). The use of non-invasive clinical data combined with physics and physiology gives more insight in the substrate underlying abnormal characteristics observed in clinics. Digital Twin simulations revealed that ACM disease expression, in terms of regional right ventricular deformation abnormalities, is related to increased regional heterogeneity of myocardial contractility and compliance. Longitudinal Digital Twin simulations of subjects with early-stage or preclinical ACM demonstrated that the development and further evolution of tissue property heterogeneity occurs independent of age. The basal segment of the right ventricular free wall was consistently found to have a decreased contractility and compliance compared to the apical segment, which is in line with the current paradigm. The Digital Twin modelling framework presented in this Thesis can easily be applied to cardiac pathologies other than ACM. Once all challenges are overcome, the Digital Twin technology can be used for personalized clinical decision support and thereby pave the way for precision medicine.

References

1. Arts T, Delhaas T, Bovendeerd P, Verbeek X, Prinzen F. 2005 Adaptation to Mechanical Load Determines Shape and Properties of Heart and Circulation: the CircAdapt Model. *Am. J. Physiol. Heart Circ. Physiol.* **288**, 1943–1954. (doi:10.1152/ajpheart.00444.2004.)
2. Lumens J, Delhaas T, Kirn B, Arts T. 2009 Three-wall segment (TriSeg) model describing mechanics and hemodynamics of ventricular interaction. *Ann. Biomed. Eng.* **37**, 2234–2255. (doi:10.1007/s10439-009-9774-2)
3. Morris MD. 1991 Factorial Sampling Plans for Preliminary Computational Experiments. *Technometrics.* **33**.
4. Hornfeck W, Kuhn P. 2015 Diaphony, a measure of uniform distribution, and the Patterson function. *Acta Crystallogr. Sect. A Found. Adv.* **71**, 382–391. (doi:10.1107/S2053273315007123)
5. Cartoski MJ, Nikolov PP, Prakosa A, Boyle PM, Spevak PJ, Trayanova NA. 2019 Computational Identification of Ventricular Arrhythmia Risk in Pediatric Myocarditis. *Pediatr. Cardiol.* **40**, 857–864. (doi:10.1007/s00246-019-02082-7)
6. Arevalo HJ, Vadakkumpadan F, Guallar E, Jebb A, Malamas P, Wu KC, Trayanova NA. 2016 Arrhythmia risk stratification of patients after myocardial infarction using personalized heart models. *Nat. Commun.* **7**, 11437. (doi:10.1038/ncomms11437)
7. Prakosa A *et al.* 2018 Personalized virtual-heart technology for guiding the ablation of infarct-related ventricular tachycardia. *Nat. Biomed. Eng.* **2**, 732–740. (doi:10.1038/s41551-018-0282-2)
8. Gray RA, Pathmanathan P. 2018 Patient-specific cardiovascular computational modeling: Diversity of personalization and challenges. *J. Cardiovasc. Transl. Res.* **11**, 80–88. (doi:10.1007/s12265-018-9792-2)
9. Mast TP *et al.* 2016 Right Ventricular Imaging and Computer Simulation for Electromechanical Substrate Characterization in Arrhythmogenic Right Ventricular Cardiomyopathy. *J. Am. Coll. Cardiol.* **68**, 2185–2197. (doi:10.1016/j.jacc.2016.08.061)
10. Priori SG *et al.* 2015 2015 ESC Guidelines for the management of patients with ventricular arrhythmias and the prevention of sudden cardiac death the Task Force for the Management of Patients with Ventricular Arrhythmias and the Prevention of Sudden Cardiac Death of the Europea. *Eur. Heart J.* **36**, 2793-2867L. (doi:10.1093/eurheartj/ehv316)
11. Priori SG *et al.* 2013 Executive Summary: HRS/EHRA/APHSR Expert Consensus Statement on the Diagnosis and Management of Patients with Inherited Primary Arrhythmia Syndromes. *Hear. Rhythm* **10**, e85–e108. (doi:10.1016/j.hrthm.2013.07.021)
12. Charron P *et al.* 2010 Genetic counselling and testing in cardiomyopathies: A position statement of the European Society of Cardiology Working Group on Myocardial and Pericardial Diseases. *Eur. Heart J.* **31**, 2715–2728. (doi:10.1093/eurheartj/ehq271)
13. Marcus FI *et al.* 2010 Diagnosis of Arrhythmogenic Right Ventricular Cardiomyopathy/Dysplasia. *Eur. Heart J.* **31**, 806–814. (doi:10.1093/eurheartj/ehq025)
14. Towbin JA *et al.* 2019 2019 HRS expert consensus statement on evaluation, risk stratification, and management of arrhythmogenic cardiomyopathy. *Hear. Rhythm* **16**, e301–e372. (doi:10.1016/j.hrthm.2019.05.007)
15. Corrado D *et al.* 2019 Arrhythmogenic right ventricular cardiomyopathy: evaluation of the current diagnostic criteria and differential diagnosis Domenico. *Eur. Heart J.* , 1–16. (doi:10.1093/eurheartj/ehz669)
16. Costa S *et al.* 2021 Impact of Genetic Variant Reassessment on the Diagnosis of Arrhythmogenic Right Ventricular Cardiomyopathy Based on the 2010 Task Force Criteria. *Circ. Genomic Precis. Med.* , 49–56. (doi:10.1161/CIRCGEN.120.003047)
17. Bosman LP *et al.* 2020 Diagnosing arrhythmogenic right ventricular cardiomyopathy by 2010 task force criteria: Clinical performance and simplified practical implementation. *Europace* **22**, 787–796. (doi:10.1093/europace/ea0039)
18. Borgquist R *et al.* 2014 The diagnostic performance of imaging methods in ARVC using the 2010 task force criteria. *Eur. Heart J. Cardiovasc. Imaging* **15**, 1219–1225. (doi:10.1093/ehjci/jeu109)
19. Taha K, Mast TP, Cramer MJ, van der Heijden JF, Asselbergs FW, Doevendans PA TA. 2019 Evaluation of Disease Progression in Arrhythmogenic Cardiomyopathy: The Change of Echocardiographic Deformation Characteristics Over Time. *JACC Cardiovasc Imaging*
20. Sarvari SI, Haugaa KH, Anfinsen OG, Leren TP, Smiseth OA, Kongsgaard E, Amlie JP, Edvardsen T. 2011 Right ventricular mechanical dispersion is related to malignant arrhythmias: A study of patients with arrhythmogenic right ventricular cardiomyopathy and subclinical right ventricular dysfunction. *Eur. Heart J.* **32**, 1089–1096. (doi:10.1093/eurheartj/ehr069)

21. Malik N *et al.* 2020 Right ventricular strain predicts structural disease progression in patients with arrhythmogenic right ventricular cardiomyopathy. *J. Am. Heart Assoc.* **9**, 1–9. (doi:10.1161/JAHA.119.015016)
22. Mast TP *et al.* 2019 The Prognostic Value of Right Ventricular Deformation Imaging in Early Arrhythmogenic Right Ventricular Cardiomyopathy. *JACC Cardiovasc. Imaging*, 14 March. **12**, 446–455. (doi:10.1016/j.jcmg.2018.01.012)
23. Chivulescu M, Lie ØH, Popescu BA, Skulstad H, Edvardsen T, Jurcut RO, Haugaa KH. 2019 High penetrance and similar disease progression in probands and in family members with arrhythmogenic cardiomyopathy. *Eur. Heart J.* , 1–10. (doi:10.1093/eurheartj/ehz570)
24. Rootwelt-Norberg C *et al.* 2021 Sex differences in disease progression and arrhythmic risk in patients with arrhythmogenic cardiomyopathy. *Europace* (doi:10.1093/europace/euab077)
25. Hoffmann R, Barletta G, Von Bardeleben S, Vanoverschelde JL, Kasprzak J, Greis C, Becher H. 2014 Analysis of left ventricular volumes and function: A multicenter comparison of cardiac magnetic resonance imaging, cine ventriculography, and unenhanced and contrast-enhanced two-dimensional and three-dimensional echocardiography. *J. Am. Soc. Echocardiogr.* **27**, 292–301. (doi:10.1016/j.echo.2013.12.005)
26. Kirkels FP, Lie ØH, Cramer MJ, Chivulescu M, Rootwelt-Norberg C, Asselbergs FW, Teske AJ, Haugaa KH. 2021 Right Ventricular Functional Abnormalities in Arrhythmogenic Cardiomyopathy. *JACC Cardiovasc. Imaging* (doi:10.1016/j.jcmg.2020.12.028)
27. Te Riele ASJM *et al.* 2013 Mutation-positive arrhythmogenic right ventricular dysplasia/ cardiomyopathy: The triangle of dysplasia displaced. *J. Cardiovasc. Electrophysiol.* **24**, 1311–1320. (doi:10.1111/jce.12222)
28. Thiene G, Nava A, Corrado D, Rossi L, Pennelli N. 1988 Right Ventricular Cardiomyopathy and Sudden Death in Young People. *N. Engl. J. Med.* **318**, 129–133. (doi:10.1056/NEJM198801213180301)
29. Basso C, Corrado D, Marcus FI, Nava A, Thiene G. 2009 Arrhythmogenic right ventricular cardiomyopathy. *Lancet* **373**, 1289–1300. (doi:10.1016/S0140-6736(09)60256-7)
30. Haqqani HM, Tschabrunn CM, Betensky BP, Lavi N, Tzou WS, Zado ES, Marchlinski FE. 2012 Layered activation of epicardial scar in arrhythmogenic right ventricular dysplasia possible substrate for confined epicardial circuits. *Circ. Arrhythmia Electrophysiol.* **5**, 796–803. (doi:10.1161/CIRCEP.111.967935)
31. De Coster T, Claus P, Kazbanov I V., Haemers P, Willems R, Sipido KR, Panfilov A V. 2018 Arrhythmogenicity of fibro-fatty infiltrations. *Sci. Rep.* **8**, 1–9. (doi:10.1038/s41598-018-20450-w)
32. Nolan MT, Thavendiranathan P. 2019 Automated Quantification in Echocardiography. *JACC Cardiovasc. Imaging* **12**, 1073–1092. (doi:10.1016/j.jcmg.2018.11.038)
33. Le HT, Hangiandreou N, Timmerman R, Rice MJ, Smith WB, Deitte L, Janelle GM. 2016 Imaging Artifacts in Echocardiography. *Anesth. Analg.* **122**, 633–646. (doi:10.1213/ANE.0000000000001085)
34. Mast TP *et al.* 2016 Prolonged Electromechanical Interval Unmasks Arrhythmogenic Right Ventricular Dysplasia/Cardiomyopathy in the Subclinical Stage. *J. Cardiovasc. Electrophysiol.* **27**, 303–314. (doi:10.1111/jce.12882)
35. Lumens J, Delhaas T. 2012 Cardiovascular modeling in pulmonary arterial hypertension: Focus on mechanisms and treatment of right heart failure using the CircAdapt model. *Am. J. Cardiol.* **110**, S39–S48. (doi:10.1016/j.amjcard.2012.06.015)
36. Heusinkveld MHG, Huberts W, Lumens J, Arts T, Delhaas T, Reesink KD. 2019 Large vessels as a tree of transmission lines incorporated in the CircAdapt whole-heart model: A computational tool to examine heart-vessel interaction. *PLoS Comput. Biol.* **15**, 1–21. (doi:10.1371/journal.pcbi.1007173)
37. Munneke AG, Lumens J, Delhaas T. 2021 Cardiovascular fetal-to-neonatal transition: an in silico model. *Pediatr. Res.* , 1–13. (doi:10.1038/s41390-021-01401-0)
38. Lyon A, Dupuis LJ, Arts T, Crijns HJGM, Prinzen FW, Delhaas T, Heijman J, Lumens J. 2020 Differentiating the effects of β -adrenergic stimulation and stretch on calcium and force dynamics using a novel electromechanical cardiomyocyte model. *Am. J. Physiol. - Hear. Circ. Physiol.* **319**, H519–H530. (doi:10.1152/ajpheart.00275.2020)
39. O'Hara T, Virág L, Varró A, Rudy Y. 2011 Simulation of the undiseased human cardiac ventricular action potential: Model formulation and experimental validation. *PLoS Comput. Biol.* **7**. (doi:10.1371/journal.pcbi.1002061)
40. Dupuis LJ, Lumens J, Arts T, Delhaas T. 2016 Mechano-chemical Interactions in Cardiac Sarcomere Contraction: A Computational Modeling Study. *PLoS Comput. Biol.* **12**, 1–20. (doi:10.1371/journal.pcbi.1005126)
41. Dupuis LJ, Lumens J, Arts T, Delhaas T. 2018 High tension in sarcomeres hinders myocardial relaxation: A computational study. *PLoS One* **13**, 1–13. (doi:10.1371/journal.pone.0204642)

42. Cerrone M *et al.* 2017 Plakophilin-2 is required for transcription of genes that control calcium cycling and cardiac rhythm. *Nat. Commun.* **8**, 106. (doi:10.1038/s41467-017-00127-0)
43. Niederer SA, Lumens J, Trayanova NA. 2019 Computational models in cardiology. *Nat. Rev. Cardiol.* **16**, 100–111. (doi:10.1038/s41569-018-0104-y)
44. Voigt JU *et al.* 2015 Definitions for a common standard for 2D speckle tracking echocardiography: consensus document of the EACVI/ASE/Industry Task Force to standardize deformation imaging. *Eur. Heart J. Cardiovasc. Imaging* **16**, 1–11. (doi:10.1093/ehjci/jeu184)
45. Nagueh SF. 2018 Non-invasive assessment of left ventricular filling pressure. *Eur. J. Heart Fail.* **20**, 38–48. (doi:10.1002/ehf.971)
46. Zghaib T *et al.* 2018 Atrial Dysfunction in Arrhythmogenic Right Ventricular Cardiomyopathy. *Circ. Cardiovasc. Imaging* **11**, e007344. (doi:10.1161/CIRCIMAGING.117.007344)
47. Walmsley J, Arts T, Derval N, Bordachar P, Cochet H, Ploux S, Prinzen FW, Delhaas T, Lumens J. 2015 Fast Simulation of Mechanical Heterogeneity in the Electrically Asynchronous Heart Using the MultiPatch Module. *PLoS Comput. Biol.* **11**, 1–23. (doi:10.1371/journal.pcbi.1004284)
48. Corral-Acero J *et al.* 2020 The 'Digital Twin' to enable the vision of precision cardiology. *Eur. Heart J.* **41**, 4556–4564B. (doi:10.1093/eurheartj/ehaa159)
49. Neal ML, Kerckhoffs R. 2009 Current progress in patient-specific modeling. *Brief. Bioinform.* **11**, 111–126. (doi:10.1093/bib/bbp049)
50. Niederer SA *et al.* 2020 Creation and application of virtual patient cohorts of heart models Subject Areas : Author for correspondence :
51. Basso C, Corrado D, Thiene G. 1999 Cardiovascular causes of sudden death in young individuals including athletes. *Cardiol. Rev.* **7**, 127–135. (doi:10.1097/00045415-199905000-00009)
52. Tabib A, Loire R, Chalabreysse L, Meyronnet D, Miras A, Malicier D, Thivolet F, Chevalier P, Bouvagnet P. 2003 Circumstances of Death and Gross and Microscopic Observations in a Series of 200 Cases of Sudden Death Associated with Arrhythmogenic Right Ventricular Cardiomyopathy and/or Dysplasia. *Circulation* **108**, 3000–3005. (doi:10.1161/01.CIR.0000108396.65446.21)
53. Ormondroyd E, Oates S, Parker M, Blair E, Watkins H. 2014 Pre-symptomatic genetic testing for inherited cardiac conditions: A qualitative exploration of psychosocial and ethical implications. *Eur. J. Hum. Genet.* **22**, 88–93. (doi:10.1038/ejhg.2013.81)
54. Ingles J, Burns C, Barratt A, Semsarian C. 2015 Application of Genetic Testing in Hypertrophic Cardiomyopathy for Preclinical Disease Detection. *Circ. Cardiovasc. Genet.* **8**, 852–859. (doi:10.1161/CIRCGENETICS.115.001093)
55. Niederer SA *et al.* 2020 Creation and application of virtual patient cohorts of heart models: Virtual Cohorts of Heart Models. *Philos. Trans. R. Soc. A Math. Phys. Eng. Sci.* **378**. (doi:10.1098/rsta.2019.0558)
56. Palau-Caballero G, Walmsley J, Van Empel V, Lumens J, Delhaas T. 2017 Why septal motion is a marker of right ventricular failure in pulmonary arterial hypertension: Mechanistic analysis using a computer model. *Am. J. Physiol. - Hear. Circ. Physiol.* **312**, H691–H700. (doi:10.1152/ajpheart.00596.2016)
57. Palau-Caballero G, Walmsley J, Gorcsan J, Lumens J, Delhaas T. 2016 Abnormal Ventricular and Aortic Wall Properties Can Cause Inconsistencies in Grading Aortic Regurgitation Severity: A Computer Simulation Study. *J. Am. Soc. Echocardiogr.* **29**, 1122–1130.e4. (doi:10.1016/j.echo.2016.07.015)
58. Willems E *et al.* 2019 The left and right ventricles respond differently to variation of pacing delays in cardiac resynchronization therapy: A combined experimental-computational approach. *Front. Physiol.* **10**, 1–13. (doi:10.3389/fphys.2019.00017)
59. van Loon T, Knackstedt C, Cornelussen R, Reesink KD, Brunner La Rocca H-P, Delhaas T, van Empel V, Lumens J. 2020 Increased myocardial stiffness more than impaired relaxation function limits cardiac performance during exercise in heart failure with preserved ejection fraction: a virtual patient study. *Eur. Heart J. - Digit. Heal.* **1**, 40–50. (doi:10.1093/ehjdh/ztaa009)
60. Lumens J. 2014 Creating your own virtual patient with CircAdapt Simulator. *Eur. Heart J.* **35**, 335–337.
61. Ashley EA. 2016 Towards precision medicine. *Nat. Rev. Genet.* **17**, 507–522. (doi:10.1038/nrg.2016.86)
62. Ginsburg GS, Phillips KA. 2018 Precision medicine: From science to value. *Health Aff.* **37**, 694–701. (doi:10.1377/hlthaff.2017.1624)
63. Huntjens PR *et al.* 2018 Electrical Substrates Driving Response to Cardiac Resynchronization Therapy: A Combined Clinical-Computational Evaluation. *Circ. Arrhythmia Electrophysiol.* **11**, 1–12. (doi:10.1161/CIRCEP.117.005647)

64. Lumens J *et al.* 2015 Differentiating Electromechanical from Non-Electrical Substrates of Mechanical Discoordination to Identify Responders to Cardiac Resynchronization Therapy. *Circ. Cardiovasc. Imaging* **8**, 1–12. (doi:10.1161/CIRCIMAGING.115.003744)
65. Basso C, Thiene G. 2007 Arrhythmogenic right ventricular cardiomyopathy/dysplasia. In *Orphanet Journal of Rare Diseases* (eds F Marcus, A Nava, G Thiene), pp. 29–44. (doi:10.1186/1750-1172-2-45)
66. Basso C, Burke M, Fornes P, Gallagher PJ, De Gouveia RH, Sheppard M, Thiene G, Van Der Wal A. 2008 Guidelines for autopsy investigation of sudden cardiac death. *Virchows Arch.* **452**, 11–18. (doi:10.1007/s00428-007-0505-5)
67. Delmar M, McKenna WJ. 2010 The cardiac desmosome and arrhythmogenic cardiomyopathies: From gene to disease. *Circ. Res.* **107**, 700–714. (doi:10.1161/CIRCRESAHA.110.223412)
68. Gibbons RJ *et al.* 1997 ACC/AHA Guidelines for Exercise Testing: A report of the American College of Cardiology/American Heart Association task force on practice guidelines (Committee on Exercise Testing). (doi:10.1016/S0735-1097(97)00150-2)
69. Vitarelli A, Cortes Morichetti M, Capotosto L, De Cicco V, Ricci S, Caranci F, Vitarelli M. 2013 Utility of strain echocardiography at rest and after stress testing in arrhythmogenic right ventricular dysplasia. *Am. J. Cardiol.* **111**, 1344–1350. (doi:10.1016/j.amjcard.2013.01.279)
70. James CA, Bhonsale A, Tichnell C, Murray B, Russell SD, Tandri H, Tedford RJ, Judge DP, Calkins H. 2013 Exercise Increases Age-Related Penetrance and Arrhythmic Risk in Arrhythmogenic Right Ventricular Dysplasia/Cardiomyopathy–Associated Desmosomal Mutation Carriers. *J. Am. Coll. Cardiol.* **62**, 1290–1297. (doi:10.1016/j.jacc.2013.06.033)
71. Prior D, La Gerche A. 2020 Exercise and Arrhythmogenic Right Ventricular Cardiomyopathy. *Hear. Lung Circ.* **29**, 547–555. (doi:10.1016/j.hlc.2019.12.007)

A



Appendices

Summary

Acknowledgment (Dankwoord)

Curriculum Vitae

List of Publications

Summary

Arrhythmogenic cardiomyopathy is an inherited pathology of the heart. In 60% of probands, a (likely-)pathogenic mutation can be found. Even before disease expression, mutation carriers are already at risk of sudden cardiac death. To prevent sudden cardiac death in apparently healthy individuals, early detection of pro-arrhythmic tissue substrates is important. This thesis aims to get more insight in the myocardial disease substrate in patients with early-stage arrhythmogenic cardiomyopathy using a *Digital Twin approach*. In the *Digital Twin approach*, a biophysical model is personalized to clinical measurements. Unlimited features describing myocardial behavior can be extracted from this *Digital Twin*. Therefore, it may reveal myocardial (mal)function underlying the measurements.

In this thesis, the CircAdapt model of cardiovascular system is used as biophysical model. This model allows fast calculation of regional myocardial mechanics and global hemodynamics. To explore the ability of personalizing this model, a simple protocol was made which focused on optimizing the right ventricular model parameters (**Chapter 2**). This protocol confirmed that the CircAdapt model was able to reproduce clinically measured deformation. A more robust parameter optimization algorithm was needed to cope with the non-linear parameter space and to further personalize the model.

Keeping the high complexity of the problem in mind, an extensive sensitivity and identifiability analysis was performed (**Chapter 3**). The most important model parameters needed to model left and right ventricular deformation were identified using the Morris Screening method and using Monte Carlo simulations. By reducing the number of model parameters, reproducibility of the estimation was improved. The final subset includes regional tissue contractility, passive stiffness, activation delay, and wall size. Subsequently, a parameter optimization protocol based on Particle Swarm Optimization was designed. We demonstrated that the CircAdapt model was still able to accurately simulate deformation in subjects with genetic mutations related to arrhythmogenic cardiomyopathy.

The parameter optimization protocol was applied to a cohort of 68 patients with arrhythmogenic cardiomyopathy and 20 control subjects who were evaluated at the UMC Utrecht in the Netherlands between 2006 and 2015 (**Chapter 4**). Simulations revealed that in subjects with clinically advanced disease compared to mutation carriers without clinically established disease, regional RVfw heterogeneity of both contractile function ($17\pm 13\%$ vs. $8\pm 4\%$, $p=0.01$) and compliance ($18\pm 11\%$ vs. $10\pm 7\%$, $p<0.01$) was increased and. No significant difference in activation delay was found.

The estimations obtained in Chapter 3 and 4 contain noise. Among others, measurement uncertainty propagates through the optimization adding noise. This is

negligible on a population level, but will affect the individual result. Therefore, in **Chapter 5**, a Bayesian optimization approach was applied to include measurement uncertainty. Hereby, a posterior distribution was estimated rather than a single point. This allows to predict whether disease substrate deteriorates over time, or not. To do so, the Adaptive Multiple Importance Sampling algorithm was used, which iteratively updates the proposal distribution of the model parameters. This algorithm was shown to be accurate as virtual estimations were precise and real-world estimations were highly reproducible. This algorithm was applied to a case study of two subjects and revealed the evolution of early-stage AC disease over time using longitudinal follow-up datasets.

In **Chapter 6**, the Bayesian optimization approach as shown in Chapter 5 was applied to a cohort of 82 early stage patients with arrhythmogenic cardiomyopathy from a consecutive cohort evaluated at Oslo University Hospital, Rikshospitalet, Norway. A total of 313 baseline and follow-up echocardiographic assessments were included with a mean follow-up of 6.7 ± 3.3 years. Patients were divided into three groups based on age at baseline: early presenters (<30 years), mid-life presenters (30-50 years) and late presenters (>50 years). In all three age-groups, both global and segmental deformation characteristics deteriorated. The development of local tissue substrates in the RV free wall was expressed in increased heterogeneity in estimated RV tissue properties. This chapter showed that deformation imaging and patient-specific computer simulations can be used to follow-up disease substrate progression in patients with early arrhythmogenic cardiomyopathy.

With this thesis, we aimed to get more insight in the myocardial disease substrates observed in early-stage arrhythmogenic cardiomyopathy. By doing so, we developed a modelling framework for patient-specific estimation for model parameters representing regional myocardial tissue properties. With this framework, the tissue properties were estimated. This revealed the patient-specific tissue substrate underlying abnormal tissue deformation. **Chapter 7** discusses the results and main findings of the different chapters in a broader perspective. It addresses the limitations of this optimization framework, but also the possibilities within the context of arrhythmogenic cardiomyopathy and cardiovascular diseases in general as this framework can be easily adapted for other purposes. With this optimization framework, we are one step closer to use patient-specific computational simulations in precision medicine, *Making it Personal*.

Acknowledgment (Dankwoord)

Daar is het dan, vier jaar werk gebundeld in een boekje. Het wordt zelfs gelezen, althans, het dankwoord. En terecht, want dit boekje was er nooit geweest zonder de hulp van anderen. Ik ga geheid iemand vergeten, maar ga toch een poging doen iedereen te bedanken die bijgedragen heeft aan dit onderzoek en mijn ontwikkeling de afgelopen vier jaar. Zonder de kansen die ik gekregen heb, de aanwijzingen, de tips en tricks, de voorbeelden, de afleidingen, de humor en spanning, de gedeelde bloed zweet en tranen, was het nooit gelukt.

Beste **Joost**, ik kan me ons eerste gesprek goed herinneren. Grappig om te zien hoe mijn idee van ‘dit is makkelijk, paar vergelijkingen oplossen’ in ‘het is toch best complex’ is veranderd. Je hebt me weten te enthousiasmeren over CircAdapt en laten zien dat er nog zo veel meer mee kan. Dank voor alle discussies die we hebben gehad, de gezelligheid en intermezzo’s als het goed ging en de positieve inspiratie en kritische blik als ik het even niet zag. Jouw presentaties en visualisaties zijn altijd een inspiratie geweest. Dank dat ik de mogelijkheid heb gehad om aan dit project te werken. Dank voor al je hulp, de leuke momenten en voor het zijn van mijn promotor.

Beste **Tammo**, na mijn masterthesis op station Eindhoven afgegeven te hebben, mocht ik in jouw groep aan de slag gaan. Jouw kritische blik en oog voor detail heeft mijn werk sterk verbeterd, van het opmaken van figuren tot het tekstueel uitwerken. Jouw fysiologische vraagstukken weten altijd een interessante discussie op te wekken. Ook jouw drang voor optimalisatie is goed wiskundig onderbouwd (traveling salesman problem). Dank voor al je hulp, de leuke momenten en voor het zijn van mijn promotor.

Prof. dr. F.W. Prinzen, dr. ir. P.H.M. Bovendeerd, Prof. dr. ir. R.L.M. Peeters, dr. A.S.J.M. te Riele en Prof. dr. P.G.A. Volders, dank voor jullie tijd om mijn proefschrift kritisch door te nemen en plaats te nemen in de beoordelingscommissie.

The work presented in this thesis is nothing without the collaboration between Utrecht Medical Centre, Oslo University Hospital – Rikshospitalet, and Maastricht University. Thank you **dr. A.J. Teske, dr. M.J.M. Cramer, and Prof. dr. K.H. Haugaa** for your input and comments.

In deze samenwerking natuurlijk een bijzonder dankjewel naar **Feddo**. Wat een tijd zeg. De paar mailtjes in het begin zijn uitgelopen tot regelmatig meeten in Maastricht/Utrecht naar bijna dagelijks zoomen om onze deadlines samen te halen. Dank voor al je input, klinische inzicht, biertjes en gezelligheid. Veel succes zelf in de kliniek en tussendoor verder promoveren.

Tim en Tijmen, zonder jullie had mijn werk er heel anders uitgezien. Dank voor alle diepgaande discussies om de fysiologie achter het model beter te begrijpen en alle

algoritmes te verbeteren en perfectioneren. Om te voorkomen dat we te fit zouden worden na het vele exercisen en de vele hartslagen op de kamer, zijn er de nodige stroopwafels en pepernoten doorheen gegaan. Helaas mocht ons tripje naar Tirol niet doorgaan, toch hebben ‘Die Mayrhofner’ ons op eigen bodem veel inspiratie mogen geven.

Ook alle andere leden van de focus groep bedankt voor de nuttige discussies! **Aurore**, thank you for your help and feedback writing my first papers. **Ahmed, Andrija, Anneloes, Claudia, Melania, Roel**, and ex-members **Lauren, Peter**, and **Erik**, thank you all for our weekly discussions, coffee breaks, and games. Thanks to all people on the other side of the wall and in the hallway: **Afrah, Alessandro, Bart, Koen vdL, Myrthe, Koen R, Mehrdad, Mijde, Shaiv, Wouter**. Velen van jullie hebben bijgedragen aan de BME pauze-spellen, zoals voetbal (hooghouden en hoogtrappen), petanque (kogelstoten op een berg) en pingpong (of zoeken naar een plek om te pingpongen). **Ben, Bennis, Frank, Maarten, Niek, Pamir, Raoul** en **Sjeng**, de voetbal en 2-wieler generatie van BME. Jullie zijn mij allemaal voorgegaan waar ik veel van heb kunnen leren. **Theo**, bedankt voor al je wijze woorden en inzichten in (het modeleren van) de fysiologie. **Claire**, bedankt voor het koffie apparaat, de dagjes uit en het in toom houden van de afdeling. BME is ook niks zonder de studenten die rondhagen. Dank voor alle gezelligheid op het lab.

Ook de mensen van de CRT / TRANCE meeting wil ik bedanken: **Frans, Kevin, Nienke, Meike, Moedi, HongXing, Floor, Jolijn, Justin, Philip, Richard, Rick, Twan, Uyen** en iedereen die ik vergeet, bedankt voor het luisteren naar mijn (te diepgaande) presentaties en de feedback die daarop gekomen is. Hier heb ik altijd veel aan gehad.

De afgelopen jaren heeft het treintje naar Maastricht mee mogen genieten van mij en meerderen van jullie. Wanneer de meeste reizigers wilden slapen kwamen de beste discussies op gang, of het nu 7 uur in de ochtend of 11 uur in de avond was. Tim, Anneloes, Roel, Feddo (tot Eindhoven dan) en anderen die zich wel eens aangesloten hebben, bedankt voor deze gezellige momenten.

Dit is ook de plek om vrienden te bedanken voor alle afleiding. **Iris, Koert, Marjolein, Nimke, Pascal, Sandra, Sanne, Saskia, Tom**, een mooi voorbeeld hoe een pauze app niet op pauze blijft staan. De spelletjesavonden veranderden in ‘we moeten nog een spelletje spelen’-avonden naar spelletjesmiddag op de grond. Hopelijk mogen we nog vele spelletjesmomenten samen hebben. **Nina** en **Bibi**, jullie enthousiasme over (onze) Tirol muziek was geweldig. **Robin**, van dansen naar boulderen heb ik veel bij je mogen klagen over alle en nog wat. En ‘avondje stad’ was minstens zo gezellig met **Ilona** erbij.

Ook familie wil ik bedanken. **Mike** en **Manon**, helaas is Roosendaal wat ver van Eindhoven af, maar dat maakt het niet minder gezellig. Dank voor het helpen sjouwen van de kasten en het bureau. **Papa** en **Mama**, dank voor al jullie hulp, steun en vertrouwen in mij! Jullie hebben mij de kans gegeven mijzelf te vormen. Ook mijn schoonfamilie kan ik

natuurlijk niet vergeten. **Rudi en Ginette**, bedankt voor de afleiding en de andere redenen dan werk om in Maastricht en omstreken te zijn.

Lieve **Melanie**, zonder jou was dit boekje nooit tot stand gekomen. Jouw liefde, rust en steun heeft de downs minder down gemaakt en de ups alleen maar beter. Ik ben zo trots jou mijn vrouw te mogen noemen. Drie jaar lang heb ik gedacht je hier als laatste te mogen bedanken, maar toch ben ik trots nog iemand te noemen. Lieve **Livia**, zonder dat je er was heb je veel betekent. Het schrijven van de laatste hoofdstukken ging gepaard met fantaseren over jou en wat voor kamer je mooi zou vinden. Je was die extra druk om alles op tijd af te ronden. En nu tijdens het schrijven van dit stuk laat je horen dat je er bent. Melanie en Livia, ik hoop nog veel inspiratie en motivatie van jullie te mogen krijgen. Ik hou van jullie!

Curriculum Vitae

Nick van Osta was born on July 6, 1994 in Roosendaal, Noord-Brabant, the Netherlands. After attending atheneum (pre-university education) at Gertrudiscollege, he started his academic education in September 2012 at Eindhoven University of Technology (TU/e) where he obtained his Bachelor's degree Biomedical Engineering in 2015.

In 2015, he enrolled the Master Biomedical Engineering. In 2016, Nick performed an internship at the Karlsruhe Institute fur Technology (KIT) under the supervising of Prof. Dr. rer. nat. Olaf Dössel as part of his Master's program. During this internship, he investigated the effect of residual stresses in a Finite Element model of the left ventricle. His graduation project under the supervision of dr. ir. Peter Bovendeerd focused on cardiac growth. He investigated the effect of a local stimulus-effect relation in a Finite Element model of the left ventricle.

After obtaining his Master's degree in 2017, Nick started as a PhD candidate at the Department of Biomedical Engineering (Maastricht University) under the supervision of prof. dr. ir. Joost Lumens and prof. dr. Tammo Delhaas. During his PhD, he worked on important aspects of patient-specific modelling. He developed a modelling framework which can estimate tissue properties based on clinical deformation measurements in patients with arrhythmogenic cardiomyopathy using the CircAdapt model – a model of the cardiovascular system. This PhD resulted into the Digital Twin approach presented in this dissertation.

Nick will continue his career at the Department of Biomedical Engineering (Maastricht University) to further explore the applicability of the Digital Twin approach.

List of Publications

Peer reviewed journals

Nick van Osta, Aureore Lyon, Feddo P. Kirkels, Tijmen Koopsen, Tim van Loon, Maarten J. Cramer, Arco J. Teske, Tammo Delhaas, Wouter Huberts, Joost Lumens “Parameter subset reduction for patient-specific modelling of arrhythmogenic cardiomyopathy-related mutation carriers in the CircAdapt model” *Philosophical Transactions of the Royal Society A* (2020)

Nick van Osta, Feddo P. Kirkels, Aureore Lyon, Tijmen Koopsen, Tim van Loon, Maarten J. Cramer, Arco J. Teske, Tammo Delhaas, Joost Lumens “Electromechanical substrate characterization in arrhythmogenic cardiomyopathy using imaging-based patient-specific computer simulations” *EP Europace*, 23(Supplement_1), i153-i160 (2021)

Nick van Osta, Feddo P. Kirkels, Tim van Loon, Tijmen Koopsen, Aureore Lyon, Roel Meiburg, Wouter Huberts, Maarten J. Cramer, Tammo Delhaas, Kristina H. Haugaa, Arco J. Teske, Joost Lumens. “Uncertainty quantification of regional cardiac tissue properties in Arrhythmogenic Cardiomyopathy using adaptive multiple importance sampling” *Frontiers in Physiology* 12:738926 (2021)

In preparation

Feddo P Kirkels, **Nick van Osta**, Christine Rootwelt-Norberg, Monica Chivulescu, Øyvind Lie, Folkert W. Asselbergs, Maarten J. Cramer, Tammo Delhaas, Arco J. Teske, Kristina H. Haugaa, Joost Lumens. “Monitoring age-related Penetrance of Structural Right Ventricular Disease in Arrhythmogenic Cardiomyopathy”.

Conference proceedings

Nick van Osta, Feddo P. Kirkels, Aureore Lyon, Tammo Delhaas, Maarten J. Cramer, Arco J. Teske, Joost Lumens “Personalization of Biomechanical Models for Early Detection of Disease in Arrhythmogenic Cardiomyopathy” *2018 Computing in Cardiology Conference* (2018)

(Poster) Presentations

Dutch Heart Foundation PhD course, papendal, October 2018, Personalization of Biomechanical Models for Early Detection of Disease in Arrhythmogenic Cardiomyopathy

EHRA 2019, Lisbon March 2019, **Runner up** at the best oral e-cardiology abstract award competition; “Characterization of Right Ventricular Electromechanical Tissue Substrates in Arrhythmogenic Cardiomyopathy: A Patient-Specific Modelling Approach”

Cardiac Physiome, Maastricht December 2019, Oral presentation, “Parameter Subset Reduction for Patient-Specific Modelling of Arrhythmogenic Cardiomyopathy Related Mutation Carriers in the CircAdapt Model”

Meeting on Myocardial Function Imaging 2020, Leuven February 2020, Oral presentation “RV Disease Characterization using Strain-Based Patient-Specific Modeling in Arrhythmogenic Cardiomyopathy”

ESC 2020, Amsterdam August 2020, Poster Presentation: “Arrhythmogenic cardiomyopathy is characterized by apex-to-base heterogeneity of right ventricular myocardial contractility and stiffness: an imaging-based patient-specific modeling study.”

EACVI – Best of Imaging 2020, Online Event, December 2020, Oral Presentation, “Arrhythmogenic cardiomyopathy is characterized by apex-to-base heterogeneity of right ventricular myocardial contractility and stiffness: a patient-specific modeling study.”

EuroEcho 2021, Berlin December 2021, Poster Presentation, “Arrhythmogenic cardiomyopathy is characterized by apex-to-base heterogeneity of right ventricular myocardial contractility and stiffness: An imaging-based patient-specific modeling study”

Not included in this thesis

Nick van Osta, Loes van der Donk, Emanuele Rondanina, Peter Bovendeerd. “Modeling cardiac growth: an alternative approach.” International conference on functional imaging and modeling of the heart. Springer, Cham, 2019.

